Institut für Physik
Arbeitsgruppe Nichtlineare Dynamik

Recurrent outbreaks in Ecology:

Chaotic dynamics in complex networks

Dissertation
zur Erlangung des akademischen Grades
doctor rerum naturalium (Dr. rer. nat.)
im Fach Physik / Nichtlineare Dynamik

eingereicht an der
Mathematisch-Naturwissenschaftlichen Fakultät
der Universität Potsdam

von

Sébastien Clodong

Potsdam, August 2004

Contents

1 Introduction **5**

2 Outbreak Phenomena in Natural Systems **7**
2.1 Classification and examples 7
2.2 Modeling outbreaks 11
2.2.1 Classical approach: outbreak as an excitable system 12
2.2.2 New approach: a bottom-up outbreak model 15

3 Phytoplankton Blooms **17**
3.1 Introduction 17
3.2 The chemostat model 18
3.3 Stability analysis of the unforced model 20
3.4 Characterizing phytoplankton blooms 22
3.5 Chaotic dynamics 24
3.5.1 Introduction of external forcing 24
3.5.2 Bifurcation analysis 26
3.6 Conclusion 30
Appendix A: Transition to the Monod model 31

4 Epidemics Outbreaks **33**
4.1 Background 33
4.2 The SIR-model 35
4.3 Symbolic dynamics 37
4.3.1 Transition probabilities 38
4.3.2 Block entropies 39
4.4 Reconstruction of attractors from data 40
4.5 Reducing the SIR-model to an asymmetric tent map 43
4.6 Introducing the coupling between cities 45
4.6.1 Simple case of 2 cities 46

4.6.2 Size distribution and network of cities . . . 51
4.7 Dynamics in the network . . . 53
4.8 Conclusion . . . 55
Appendix A: Extension to coupled Rössler oscillators . . . 56

5 Complex Dynamics in Networks with distributed Sizes 59
5.1 Motivation . . . 59
5.2 Coupling N maps in a weighted network . . . 60
5.3 Analysis of the network topology . . . 61
5.3.1 The case $\mu \to \infty$: hierarchical topology . . . 62
5.3.2 Intermediate values of μ: weighted links . . . 67
5.4 Networks of asymmetrical tent maps . . . 69
5.5 Generalization to the logistic maps . . . 71
5.6 Dynamics in the network and bifurcation analysis . . . 72
5.6.1 Influence of the effective temperature $T_{eff} \sim 1/\mu$ . . . 77
5.6.2 Influence of the coupling strength ϵ . . . 78
5.6.3 Influence of the threshold κ . . . 79
5.6.4 The role of the sizes in the system . . . 79
5.7 An effective theory . . . 80
5.7.1 Analytical formulation of the evolution of the system . . . 81
5.7.2 Testing the theory . . . 82
5.8 Results . . . 83
Appendix A: Tree masting . . . 85

6 Outlook 87

Chapter 1

Introduction

This thesis is devoted to the study of outbreak phenomena in natural chaotic systems. The classical models refer to the concept of excitable system and allow only top-down control of the outbreaks. Therefore we developed a new modeling approach based on bottom-up models.

The novelty of our approach is shown into two case studies: the dynamics of phytoplankton blooms under variable nutrients supply and the spread of epidemics in networks of cities. These two systems are characterized by a short-term and a long-term dynamics. It can occur a single outbreak but one can also observe recurrence of outbreaks, respectively. Short-term behavior is introduced through models having very similar mathematical formulation and long-term behavior through periodic forcing of the environments. Both systems can be described by the same class of bottom-up models even if they are very different.

In the second Chapter we give an overview of the concepts of single and recurrent outbreaks. Some of the most striking examples from Ecology are shown. We also present the two classes of top-down and bottom-up models. A mathematical formulation of the model is given and their respective dynamics is explained in phase space.

Natural aquatic systems like lakes offer very good examples for the annual recurrence of outbreaks in Ecology. In Chapter 3 we therefore examine the effect of seasonal forcing on simple models of algal growth. The idea whether chaos is responsible for the irregular heights of outbreaks is central in the domain of ecological modeling. This question is investigated in the context of phytoplankton blooms. We study the possibility of chaotic dynamics in the externally driven Droop model. This model describes a phytoplankton population in a chemostat under a periodic supply of nutrients. Previously it has been proven under very general assumptions that such systems are not able to exhibit chaotic dynamics. Here we show that the simple introduction of algal mortality may lead to chaotic oscillations of algal density in the forced chemostat. Conditions for the existence of chaos

are obtained in terms of stability analysis of the unperturbed system. In the unforced model the introduction of mortality leads to complex eigenvalues of the stable steady state. Chaotic dynamics results upon interaction of the resulting damped oscillations with the external driving force. These findings are not restricted to the Droop model but hold also for other chemostat models with mortality. Our results suggest periodically driven chemostats as a simple model system for the experimental verification of chaos in ecology.

We introduce in the fourth Chapter the notion of spatially extended system. The dynamics of epidemics in networks of cities is a problem which offers many ecological and theoretical aspects. We use here the concept of symbolic dynamics to analyze in a more convenient way the dynamics of the system. We also succeed to reconstruct the attractor of the system from the data of infectious childhood diseases. It could be shown that a single epidemiological model can be reduced to a one-dimensional map. The coupling between the cities is introduced through their sizes and gives then rise to a weighted network which structure is generated from the distribution of the city sizes. We examined the dynamics in this network and find that different regimes are possible. One of these regimes is the bi-annually cycle of outbreaks which is also observed in data.

In Chapter 5 we analyze of complex dynamics in networks of weighted maps. Since the weights can be distributed over several orders of magnitude, we introduced the coupling between the maps through a saturation function. This coupling function possess a parameter which can be interpreted as an effective temperature for the network. Changing this parameter permits us to vary continously the topology from global coupling to hierarchical networks. It is possible in some cases to compute the main statistical properties of the networks. We find that the system shows the same dynamical regimes than those observed in the network of cities. We perform bifurcation analysis of the global dynamics and succeed to construct an effective theory explaining very well the behavior of the system.

Finally we summarize our results and give an outlook on possible research in the last part of this thesis.

Chapter 2

Outbreak Phenomena in Natural Systems

> *And the locusts went up over all the land of Egypt and rested in all the coasts of Egypt: very grievous were they. For they covered the face of the whole earth, so that the land was darkened; and they did eat every herb of the land, and all the fruit of the trees which the hail had left: and there remained not any green thing in the trees, or in the herbs of the field, through all the land of Egypt.* (Exodus X)

2.1 Classification and examples

One of the most striking features of ecological systems is their ability to undergo sudden outbreaks in the population numbers of one or a small number of species. Such population outbreaks often appear without any warning or obvious cause and naturally often go together with tremendous implications for the environment and the rest of the ecosystem. Intuitively a *single outbreak* can be characterized by the following properties (see also Figure 2.1):

- There is a drastic change in the population numbers, which sometimes can be up to several order of magnitude.
- The change in abundance is very fast compared to the typical time-scale for the evolution of the system.
- After some characteristic time the population numbers are reduced back again into the rest state and the system relaxes.

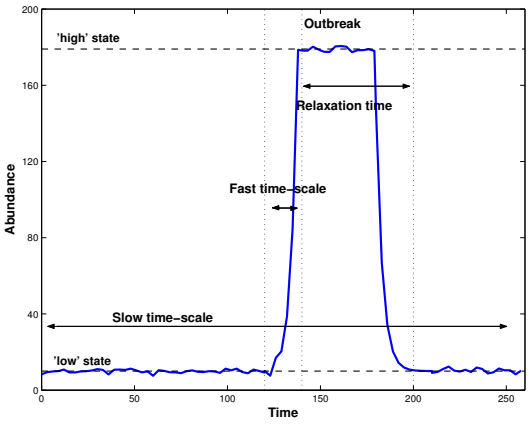

Figure 2.1: Schematic representation of a single outbreak. Shown are the existence of an excited ('high') and a relaxed ('low') state such as slow and fast time-scales.

- An additional property of outbreak can be their recurrence (see Figure 2.2). This comes from the fact that natural systems are often exposed to periodical variations of the environment.

Even though this definition mathematically may be not very precise it helps to classify phenomena which are observed in Nature or in numerical models. For example, it allows to classify the possible states of the system into a 'low' (or 'rest') state and a 'high' (or 'excited') state.

Typically, outbreaks in natural systems are no single events. Instead very often after some time the single outbreak is followed by repetitions of successive outbreaks. In this case one speaks about *recurrent outbreaks* (see Figure 2.2). Furthermore, in many natural outbreak time series are characterized by the fact that the timing of outbreaks is very regular, whereas the amplitude or height of outbreaks can be irregular. This property was termed UPCA (Uniform Phase and Chaotic Amplitudes) [4, 32].

Such outbreak phenomena as characterized by the previous definition are ubiquitous in living systems. In the following we present some typical examples:

- One classical example is the outbreak of insect pests like the spruce budworm [24], the lepidoptera *Thrips imaginis* [9] or the budmoth in the Alps [3, 28]. Such insect outbreaks and their hazardous effects are very common and are known for long times. Already the Bible mentions the outbreak of locusts as one the ten plagues (see quotation at the beginning of this chapter). The periodic behavior of these outbreaks is shown on Figure 2.3. It is obvious that these insect pests can have great impact on agriculture with large consequences for economy. Thus, it is a challenge

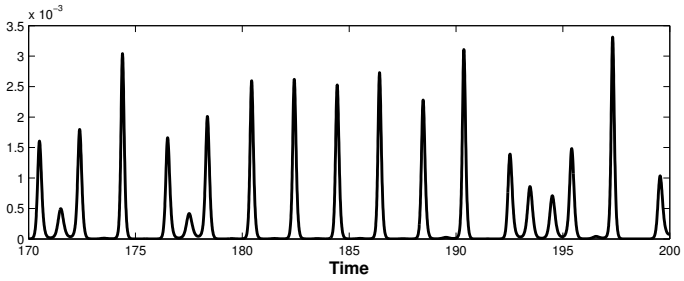

Figure 2.2: Representation of recurrent outbreaks.

for scientists to understand their dynamics to find solutions for management and control [6].

- As shown in [4], cycles of outbreaks can also be found among larger animals. A common example with such rapid multiplication in population numbers are large amplitude predator-prey cycles in mammals, like the Canadian lynx *Lynx canadensis* and the snowshoe hare *Lepus americanus* (see Figure 2.4b).

- Outbreaks also play a central role in the dynamics of phytoplankton in lakes or sea water [10, 55, 48, 49] under the form of algae blooms. Since the phytoplankton belongs to the primary producers, it is necessary to understand its dynamics for the comprehension of the whole aquatic system. Algae are also important for men as an indicator for water quality. Algae blooms of large magnitude may be related to eutrophication [11]. Figure 2.4c shows periodical algae blooms in the Lake Kinneret in Israel. Algae also play a crucial role in the global CO_2 cycle [65, 66, 67, 63, 69]. Large-scale experiments related to this question are performed through iron fertilization in the Arctic Ocean [68].

- Another important topic with drastic outbreak dynamics is the dynamics of micro-parasitism. In this context the rapid outbreaks in the numbers of infected individuals are known as epidemics. More than one billion of the Earth's habitant are affected of parasitic diseases. The number of newly emerging pathogens (HIV, BSE, SARS...) and re-emerging infectious diseases (tuberculous, cholera...) has alarmingly increased over the last decades. A well documented case for recurrent epidemic outbreaks are childhood diseases like measles, chicken pox or rubella (see Figure 2.4a).

- Understanding the dynamics of forests is essential for the conservation of a large number of species [111, 125, 112]. Dynamics with all the characteristics of outbreaks are exhibited in the fruit production of trees (masting). Data about the tree masting

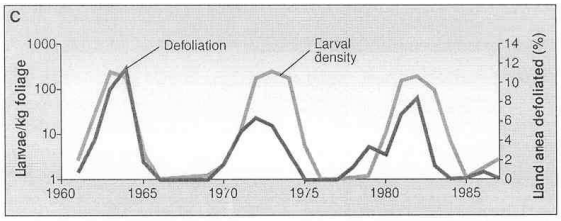

(a)

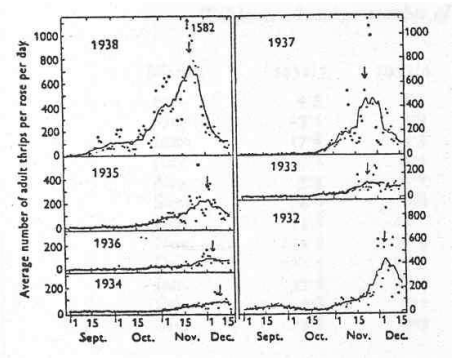

(b)

Figure 2.3: Examples of periodic insect outbreaks. a) The larvae of the budmoth (*Zeiraphera diniana*) causes severe periodic defoliation in larch forests [28] (note the logarithmic scale). b) *Thrips imaginis* shows annual outbreaks [9].

of North American oaks can be found in [23]. They observed spatial synchrony in the mast seeding of these trees (see Figure 2.5a).

- The phenomenology of outbreaks is reminiscent to phenomena in other disciplines. For example in neuroscience, recordings from single neurons show characteristic spike trains with recurrent localized sharp changes in voltage [19, 27, 15] (see Figure 2.5b). The phenomenology of such neural spike trains, usually going together with the idea of excitable system, has very similar properties as that exhibited by outbreaks in ecological systems.

Outbreaks in ecology cannot be seen as isolated events. They propagate through the ecosystem (often in the form of traveling waves) and influence the dynamics of other parts of the systems. Typical properties of natural systems related to outbreaks are seasonality [29, 46, 53], predator-prey cycles [4, 35, 40], extinction risk [94], stochasticity [20, 13, 95] or chaos [12, 8].

The striking similarity of outbreak characteristics, which is exhibited in totally different and unrelated (ecological) systems naturally leads to the question whether there are universal mechanisms underlying outbreak dynamics in different systems in ecology [2, 34]. In this sense a comparative study of complex outbreak phenomena in Nature gives information about possible underlying mechanisms and properties of the system.

One particular problem for the construction of outbreak models is the ability to generate the often very irregular outbreak amplitudes by simultaneous regular outbreak timings. As will be shown below, one explanation for the regular recurrence of outbreaks stems from the interaction of the natural systems with periodical variations of their environment. Periodicity in the environment is a very common feature of natural systems [9, 29, 90, 72].

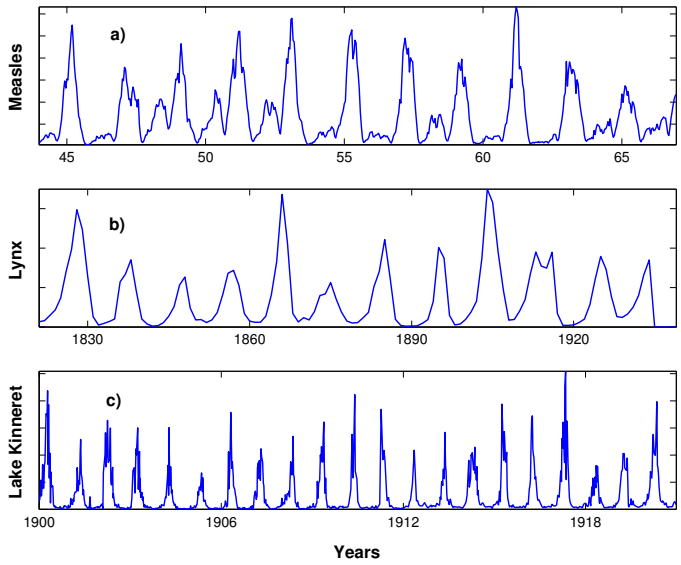

Figure 2.4: Examples of outbreak cycles in real systems. Time series of a) the mean number of children infected by measles in England/Whales in the pre-vaccination time, b) the abundance of Canadian lynx and c) the concentration of the algae *Peridinium* in the Lake Kinneret (Israel).

Periodic forcing in simple ecological model typically leads to large parameter ranges with chaotic dynamics, and thus is closely related to the concept of chaos [37, 31, 17, 18, 22, 7]. On the other hand chaotic models easily are able to reproduce the observed large fluctuations in outbreak heights. Therefore systems exhibiting chaotic behavior are good candidates for realistic outbreak models. Also the idea of complexity is related to the biodiversity of ecosystems [16, 57]. Complexity and chaos enhance the stability of ecosystems [30, 76].

2.2 Modeling outbreaks

We consider in this section two distinct models for outbreak phenomena. The mechanisms which governs the outbreak dynamics in both case are completely different. The first model represents a classical excitable system where the dynamics is controlled by a top-down mechanism. The population abundance in a higher trophic level determines the whole dynamics in the system. The excitable system shows typical cycles of slow/fast dynamics.

In the second model we consider a system of the Monod- or the Michaelis-Menten-type.

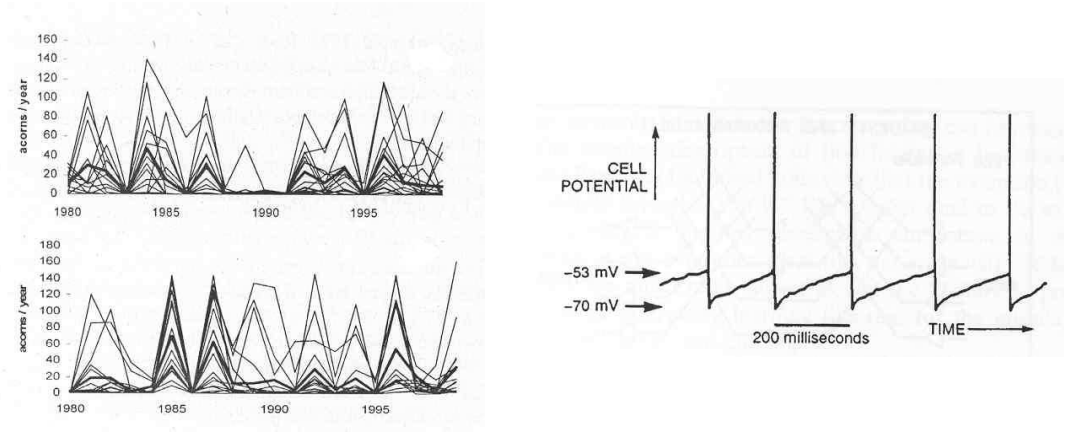

(a) (b)

Figure 2.5: Time series a) of the mast production of *Q. agrifolia* and *Q. douglasii* from the Hastings Reservation in California [23] and b) of the internal potential of a single neuron [19].

This model shows typical outbreak dynamics in the form of damped oscillations, which are represented in the phase space by a spiral. This approach permits to build models which allow bottom-up control, where the lower trophic level controls the dynamics of the higher one.

2.2.1 Classical approach: outbreak as an excitable system

One classical model to model recurrent outbreaks in ecological system was developed in the context of tree defoliation by the spruce budworm in Eastern Canada [24]. The first variable of the model describes the density of budworms in the forest

$$\frac{dB}{dt} = rB\left(1 - \frac{B}{K}\right) - \frac{\beta B^2}{\alpha^2 + B^2} \tag{2.1}$$

where r is the intrinsic growth rate at low densities and K is the carrying capacity for the budworm. The carrying capacity is first assumed to be a constant but will be in the following a function of the resources which are available for the budworm, that mean the amount of leafs on the trees. The second term in Eq. (2.1) is a predation rate. The predators (in this case birds) are assumed to have a Holling type-III functional response, with a maximum predation rate of β and a half-saturation budworm density of α. This functional form implies that predators only eat budworms if their density is high enough ($B > \alpha$). At low density of the budworms, predators don't invest energy in searching. We perform the stability analysis of Eq. (2.1) and find that, depending on the parameters, the budworm population can show two distinct regimes. Either the system shows one fixed

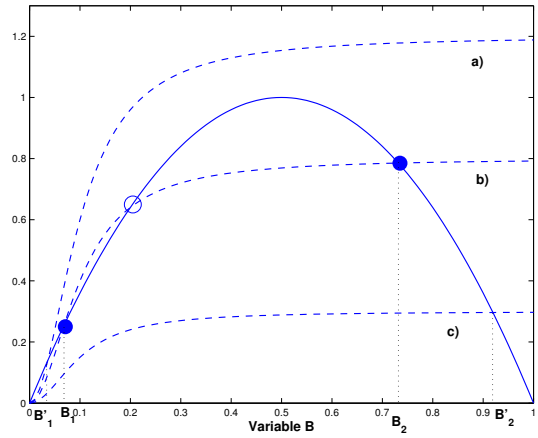

Figure 2.6: Stability analysis of the system (2.1).

point (regime I) or three fixed points (regime II). In the first regime we can distinguish two situations where the numerical value of the fixed point is either small or large (see in Figure 2.6 the points B_1' and B_2', respectively). The second regime corresponds to a situation where bi-stability occurs. In this case the system (2.1) possess two stable fixed points (B_1 and B_2 in Figure 2.6) and one unstable. We observe in regime II that the system can jump (discontinuous transition) between the two stable fixed points when varying smoothly one parameter. This phenomenon is called cusp-catastrophe and is an essential feature of this outbreak: small variations in the environment can have important consequences on the dynamics in the system. This corresponds exactly to an outbreak as we defined it previously.

We now consider the complete model which also includes the variables for the forest

$$\begin{aligned} \frac{dS}{dt} &= r_S S\left(1 - \frac{S}{K_S}\frac{K_E}{E}\right) \\ \frac{dE}{dt} &= r_E E\left(1 - \frac{E}{K_E}\right) - P\frac{B}{S} \end{aligned} \tag{2.2}$$

where S represents the average size of the trees and E the energy reserve, which is a generalized measure for the forest's health. The constants r_S, r_E, K_S, K_E and P are parameters of the forest and the carrying capacity in the equation (2.1) is now a function of the energy which is available for the budworm

$$K \longrightarrow K' = \frac{KE^2}{T_E^2 + E^2} \tag{2.3}$$

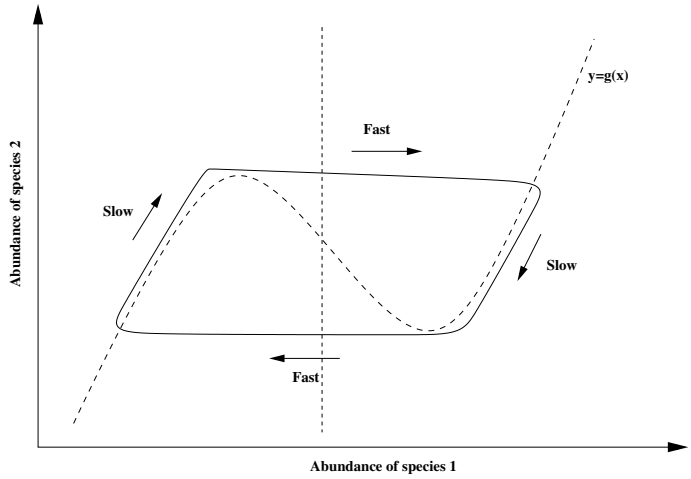

Figure 2.7: Dynamical behavior of the budworm/forest model.

where T_E represents the foliage unit per branch.

The complete tree/budworm system exhibits a very interesting periodic behavior which is shown in Figure 2.7. The dynamics can be described as composed of fast and slow periods. The energy E of the trees accumulates slowly in time up to a certain threshold. When this threshold is reached, enough food (energy) has been accumulated such that an outbreak of the budworms is triggered. These two processes correspond to a growing of the budworm population and take place in the phase plane *above* the N-shaped null-cline shown in Figure 2.7. When all the energy has been consumed, the system will be *under* the N-shaped null-cline after the outbreak. That means that the budworm population will first slowly decrease (relaxation) and after that jump to the original level before the occurrence of the outbreak. These cycle of slow and fast dynamics is typical for excitable systems. An equation that exhibits dynamics similar to the dynamics of the budworm equation, but with simpler algebra is given by

$$\frac{dx}{dt} = a + rx - x^3 \tag{2.4}$$

This cubic form is a generic model of such excitable systems and can also be found in other domains like neuro-sciences (Fitz-Hugh-Nagumo model for a single neuron).

This classical model (2.1) was very successful to model outbreaks of spruce budworm but is only able to describe top-down controlled outbreaks.

2.2.2 New approach: a bottom-up outbreak model

We introduce here an alternative approach to the classical modeling *Ansatz* of systems which show outbreak behavior. We are interesting here in the possibilities of bottom-up control of outbreaks. Therefore we consider the following simple paradigmatic Monod model [51]

$$\begin{aligned} \frac{dN}{dt} &= N_0 - lN - \mu \frac{NP}{k+N} \\ \frac{dP}{dt} &= \mu \frac{NP}{k+N} - mP \end{aligned} \tag{2.5}$$

which describes the dynamics of phytoplankton P consuming nutrients N. The parameter N_0 represents the inflow of nutrients, l the loss-rate of nutrients, μ the growing rate of algae, k the half-saturation constant and m the death rate of phytoplankton. This is a very general model for various aquatic systems like lakes or cultures in chemostats.

Depending on the parameter set, the system (2.5) can be in three different regimes:

- Regime I: All the phytoplankton dies out $P = 0$ and the concentration of nutrients reaches its highest maximum value $N = N_0/l$.
- Regime II: The phytoplankton concentration makes a peak and reaches after that the steady state. This phenomenon corresponds to an algal bloom.
- Regime III: Also here we observe the phenomenon of overshooting of the concentration of algae. The difference to the previous regime is that the concentration P undergoes damped oscillations before reaching equilibrium.

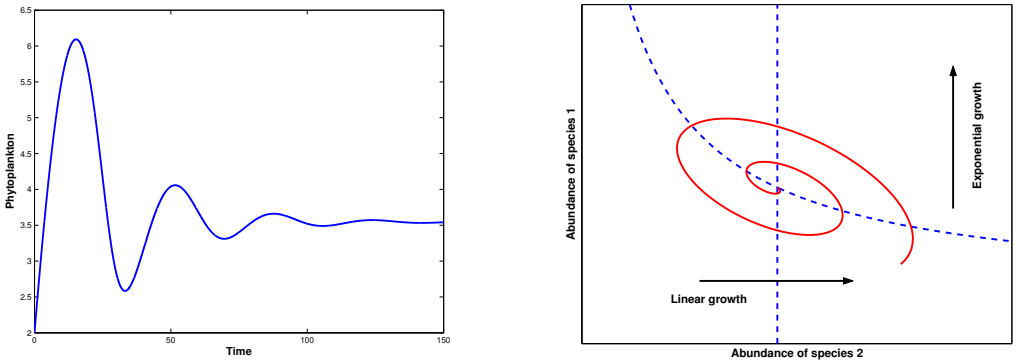

(a) (b)

Figure 2.8: Numerical simulation of the system (2.5) with parameters $N_0 = 1$, $l = 0.05$, $m = 0.75$, $k = 1$ and $\mu = 1$. a) Outbreak represented by damped oscillations. b) Trajectory of the system in phase space.

Actually, the form of the conceptual model which generates the spiral dynamics does not need to have the form of the model (2.5). The system only needs a fixed point with the Jacobian exhibiting complex conjugates eigenvalues with negative real part.

Figure 2.8 shows a typical numerical result for the dynamics of the system in the third regime. This dynamical behavior has all the properties of an outbreak: it occurs an overshooting which relaxes after a certain time to a lower concentration of algae. The model (2.1) for excitable systems permits only top-down control of the outbreak. In contrast our new approach offers the possibility of having a bottom-up control of the system. We will also show in the next section that the model 2.5 is appropriated to model the recurrence of outbreaks. This is done through the introduction of periodical forcing of the environment.

Chapter 3

Phytoplankton Blooms

3.1 Introduction

Ever since Robert May's discovery of irregular behavior in the simple logistic equation [50] ecologists have been fascinated by the possibility that similar chaotic dynamics may be exhibited by natural systems, and thus could be responsible for the common observed fluctuations in population numbers [18, 4, 8]. Beside the logistic equation many or most ecological models allow for chaotic solutions due to a number of generic mechanisms such as nonlinear internal regulations, time delayed feedback or periodic external forcing [17, 7, 4, 5]. Despite this ubiquity of chaotic regimes in the standard ecological models there are not many examples where the theoretical concepts could successfully be translated into real case studies and hard data (see for example [8]). These difficulties arise to some extend from the common shortage of ecological time series. But other problems are inherent to the systems themselves, which can never be isolated from their environment and therefore necessarily are subject to major disturbances and noise.

Recently, the method of continuous chemostats, as an experimental system for the growth of microorganisms such as phytoplankton, has been proven to be a powerful experimental setup that allows to successfully combine theoretical concepts with ecological reality [40, 59]. Most studies of chemostat dynamics have focused on ideal constant nutrient environments. In the last years, however, there has been renewed interest in nutrient limited growth of phytoplankton in environments with variable nutrient levels. For example, it has been found that time-variable conditions may promote the coexistence of competing phytoplankton species [45, 57, 71, 76]. Non-equilibrium conditions are ubiquitous in ecology. Almost without any exception biological communities are affected by perturbations that frequently show more or less periodic patterns. Consequently, the effects of periodic forcing on ecological models [22, 29, 84, 35] and on phytoplankton models [71, 72, 58] have been intensively studied. All these studies confirm that periodic forcing

typically can drive the biological system into a chaotic regime if the strength of forcing is sufficiently large. Astonishingly however, externally driven chemostats of a single species seem to be an exception from this general rule. In such systems common wisdom forbids the appearance of chaotic solutions due to external forcing [53, 56].

The classical model for describing the nutrient limited growth of phytoplankton in a chemostat dates back to Monod [51]. This simple model is able to capture basic characteristics of the algal dynamics but has been criticized because it relates the growth or phytoplankton directly to the nutrient uptake. These model assumptions are refined in the Droop model which essentially decouples algal growth from nutrient uptake [38, 39] and can now be regarded as the paradigmatic model to describe the growth of phytoplankton in a chemostat [47].

It is long known that chaotic dynamics are not possible in the periodically driven Monod-model. More complex behavior was expected to arise in the Droop model because the passage of nutrients from the outside to the inside of the cell introduces inevitable time delays. It was argued that such delays may play an important role in non-equilibrium situations [53, 47]. The consequences of periodic influence on the Droop model have been first studied by Pascual [53] where it was found that chaotic dynamics did not occur. Later on these studies were extended to various generalizations of the Droop model, however always with the same negative result. In all the investigated model variations the existence of chaos could rigorously be excluded [56]. These results led to the belief that externally forced chemostats of a single species are unable to exhibit chaotic dynamics, in this way ruling out such systems as a candidate for the experimental verification of chaos.

In this chapter we explore this case in more detail and show that simple chemostats can give rise to more complexity than was previously thought. As we show, the simple introduction of an additional algal loss or mortality allows for the existence of chaotic solutions. Algal mortality usually plays only a minor role in the laboratory system because the residence time of the cells in the chemostat is much smaller than their average life span. Therfore algal mortality is usually neglected in chemostat models. Nevertheless, it is possible to realize an effective algae mortality also in the experimental situation, for example in the form of an auxiliary flow-loop in which phytoplankton is filtered out of the water column (G. Fußmann, personal communication). As we show in the following this innocent modification of the system has fundamental dynamical consequences and for example allows for the appearance of chaos.

3.2 The chemostat model

The Droop model [38, 39] has been well studied in the last decade (see [47] for a detailed analysis). The model describes a well stirred reactor which contains phytoplankton cells with concentration $P(t)$ in a growth medium of limiting nutrients with concentration $N(t)$.

Each phytoplankton cell is assumed to possess an internal pool of stored nutrients (the so-called cell quota) $Q(t)$. The chemostat is supplied with nutrients at input concentration $N_i(t)$ from an external nutritive medium. Note, that we allow the external nutrient supply to be a function of time. The outflow contains both medium and phytoplankton cells. Inflow and outflow are characterized by the the dilution rate D. Under these assumptions the Droop model takes the following form

$$\begin{aligned} \dot{N} &= D(N_i(t) - N) - \rho(N)P \\ \dot{P} &= \mu(Q)P - (M + D)P \\ \dot{Q} &= \rho(N) - \mu(Q)Q, \end{aligned} \tag{3.1}$$

with

$$\mu(Q) = \mu_m \left(1 - \frac{K_Q}{Q}\right) \qquad \text{and} \qquad \rho(N) = \rho_m \frac{N}{K_\rho + N}. \tag{3.2}$$

It is assumed that the phytoplankton growth rate $\mu(Q)$ depends solely on the cell quota. μ_m is the maximal growth rate and K_Q is the minimal amount of nutrients per phytoplankton cell, *i.e.* $Q(t) > K_Q$. $\rho(N)$ represents the nutrient assimilation rate of the phytoplankton cells and is modeled as a Monod function with maximum uptake rate ρ_m and half saturation constant K_ρ. Furthermore we modify the model by the introduction of an additional phytoplankton mortality M.

For further analysis we rewrite the model (3.1) in non-dimensional variables

$$\begin{aligned} \dot{n} &= \delta(n_i(\tau) - n) - \frac{np}{1+n} \\ \dot{p} &= (1 - \frac{1}{q})p - (m + \delta)p \\ \dot{q} &= \frac{\alpha n}{1+n} + 1 - q \end{aligned} \tag{3.3}$$

Here the variable transformations

$$n = \frac{N}{K_\rho}, \quad p = \left(\frac{\rho_m}{\mu_m K_\rho}\right) P, \quad q = \frac{Q}{K_q}, \quad \tau = \mu_m t \tag{3.4}$$

have been performed and the new parameters are

$$m = \frac{M}{\mu_m}, \quad \delta = \frac{D}{\mu_m}, \quad n_i = \frac{N_i}{K_\rho}, \quad \alpha = \frac{\rho_m}{\mu_m K_q}. \tag{3.5}$$

In dimensionless units the model contains only four independent control parameters: the effective phytoplankton mortality m, the dilution rate δ and the input nutrient concentration n_i, all of which can be controlled in the experiment, and the parameter α, which

is related to the physiology of the phytoplankton species. Note, that the dimensionless variables are restricted to the range $n, p \geq 0$, $q \geq 1$. Besides the Droop model (3.3) we also study the more simplistic Monod model (3.19), which arises in the limit $\alpha \ll 1$, i.e. when the algal growth rate is small in comparison to the uptake rate (see Appendix A).

3.3 Stability analysis of the unforced model

Following [47] we first analyze the stability of system (3.3) without any external forcing when the supply of input nutrients is constant $n_i(t) = n_i$. The system then contains two fixed points. The first fixed point describes a steady state without phytoplankton and is given by

$$(n^*, p^*, q^*)_1 = \left(n_i,\ 0,\ 1 + \frac{\alpha n_i}{1 + n_i} \right). \tag{3.6}$$

In contrast, the second fixed point

$$(n^*, p^*, q^*)_2 = \left(\frac{d}{\alpha(1-d) - d},\ \delta(n_i - n_2^*)\frac{\alpha(1-d)}{d},\ \frac{1}{1-d} \right) \tag{3.7}$$

represents a non-vanishing algal concentration. Here, $d = m + \delta$ stands for the total phytoplankton loss rate, which acts as a main bifurcation parameter. Both fixed points collide at the critical value

$$d_c = \frac{\alpha n_i}{1 + (1+\alpha) n_i}. \tag{3.8}$$

In the case of large loss rate, $m + \delta > d_c$, the trivial equilibrium (3.6) is stable and the algae are washed out of the chemostat. In this regime (3.6) has the stability type of a stable star, i.e. all three eigenvalues of the Jacobian are negative (-,-,-). On the other hand, if the total loss rate is smaller than the threshold, $m + \delta < d_c$, the equilibrium (3.6) is unstable whereas (3.7) becomes positive and stable. Thus, at $d = d_c$ both fixed points exchange their stability in a transcritical bifurcation. Stable coexistence of nutrients and phytoplankton is only possible for $d < d_c$. Depending on the parameter set, (3.7) may then either have the stability type of a stable star (-,-,-) or of a stable spiral (-,+i,-i). Figures 3.1a and 3.1b give a visualization of these different regimes in the parameter planes (m,δ) and (m,α). Very similar stability properties arise in the Monod model (3.19). In particular, depending on the parameter set there are also two different steady state solutions of either algal washout or stable phytoplankton-nutrient coexistence. In the Monod model formula (3.8) must be replaced by $d_c' = n_i/(1 + n_i)$.

Notice from the stability diagram Figure 3.1 that spiral solutions are only allowed with explicit algal mortality, *i.e.* if $m > 0$. Therefore, one noticeable effect of phytoplankton mortality is the ability to modify the topology of the nontrivial fixed point from a stable

star to a stable spiral, in this way allowing the phytoplankton to undergo damped oscillations before reaching equilibrium. As will be shown below this difference has important consequences under external forcing.

Figures 3.2 and 3.3 depicts a typical simulation result with $m > 0$ in the region with a stable spiral. Clearly phytoplankton does not reach equilibrium monotonically but goes through an intermediate maximum value. This overshooting of phytoplankton is a direct consequence of the spiral geometry in the (n, p)-phase plane (see Figure 3.2b). As shown in Figure 3.2c the cell quota q closely follows the nutrient concentration (see also Appendix 1), and in three dimensional phase space the trajectory forms a flat spiral. This geometry is also reflected in the eigenvalue spectrum of the stable equilibrium (3.7). The eigenvalue corresponding to the eigenvector $\mathbf{v}_1^{\perp}$ normal to the plane of the spiral is a negative number, $\lambda_1 < 0$. In contrast, the other two eigenvectors $\mathbf{v}_2^{\parallel}$ and $\mathbf{v}_3^{\parallel}$ are located in the plane of the spiral and the corresponding eigenvalues form a pair of complex conjugate numbers with negative real part, $\lambda_{2,3} = -\rho \pm i\omega$. Our numerical investigations show that the absolute value of λ_1 is about one order of magnitude larger than that of the other two eigenvalues, $\lambda_1 \ll -\rho$ (see Figure 3.2 legend). Therefore, any perturbation of the system out of the plane of the spiral is very quickly re-attracted.

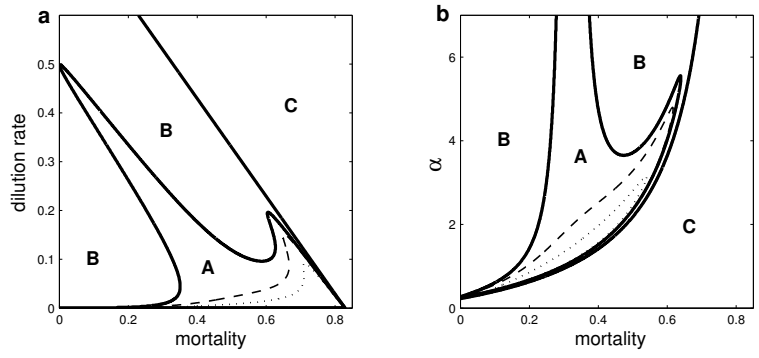

Figure 3.1: a) Stability diagram of the unforced Droop model (3.3) showing the regimes in parameter space with a stable spiral (A), a stable node (B) and algal washout (C). a) Results in (m,δ) parameter plane for $\alpha = 5$, $n_i = 40$ and b) results in (m,α) plane for $\delta = 0.11$, $n_i = 40$. Further indicated is the estimate of plankton-overshooting κ in the spiral regime calculated by Eq.(3.11). Plotted are the lines where the overshooting measure takes the constant values $\kappa = \kappa_1$ (dotted line) and $\kappa = \kappa_2$ (dashed line). Parameters: a) $\kappa_1 = 10^{-2}$ and $\kappa_2 = 10^{-4}$, b) $\kappa_1 = 10^{-3}$ and $\kappa_2 = 10^{-6}$.

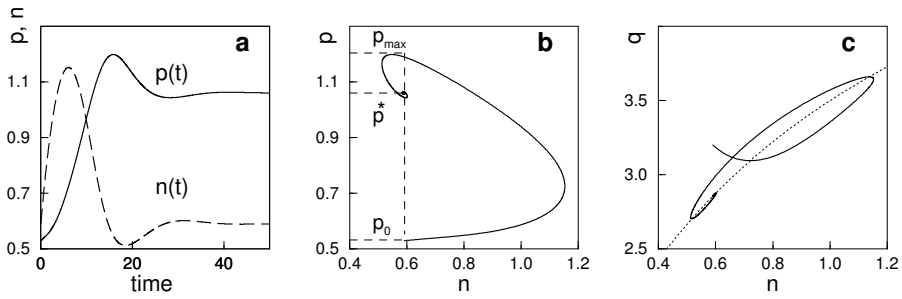

Figure 3.2: Typical behavior of the unforced model (3.3) in the spiral regime. Plotted are a) the time series of phytoplankton $p(\tau)$ and nutrients $n(\tau)$, b) and c) the resulting trajectories in the (n,p)- and (n,q)-planes, respectively. In c) also the functional dependence $q(n)$ (3.18) is drawn (dotted line). Further indicated in b) is a schematic representation of p^*, p_{max} and p_0. Parameter values $m = 0.64$, $\delta = 0.01$, $n_i = 40$, $\alpha = 5$, and initial values $n_0 = n^* = 0.59$, $p_0 = p^*/2 = 0.53$, $q_0 = 3.2$. The eigenvalues of the stable spiral are $\lambda_1 = -1.12$, $\lambda_{2,3} = -0.153 \pm 0.25\,\mathrm{i}$.

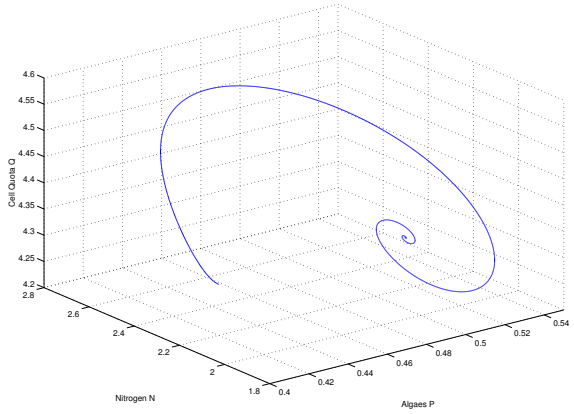

Figure 3.3: Typical behavior of the unforced model (3.3) in the spiral regime in the phase space (n,p,q). Parameter values $m = 0.73$, $\delta = 0.02$, $n_i = 40$, $\alpha = 5$, and initial values $n_0 = 2.2$, $p_0 = 0.41$, $q_0 = 4.3$.

3.4 Characterizing phytoplankton blooms

Note that the overshooting of phytoplankton in the Droop model with mortality as depicted in Figure 3.2 has all the characteristics of a single population outbreak (see Figure 2.1). Also the modeling as a spiral in phase space is a direct generalization of the conceptional outbreak model (2.5) in 2.2.2.

We now introduce a quantity which allows to measure the strength of phytoplankton overshooting. Obviously the imaginary part ω of the eigenvalues alone is not sufficient because it contains only information about the rotation speed of the spiral but not about the damping. In fact, we observe that the ratio ρ/ω of real and imaginary parts gives a good characterization. This becomes clear by inspection of Figure 3.2b. Starting from initial conditions (n^*, p_0) which in phase space are located with a vertical distance $p^* - p_0$ exactly below the fixed point, we estimate the height of the following intermediate phytoplankton maximum, p_{max}. The ratio $\kappa = (p_{max} - p^*)/(p^* - p_0)$ is then a measure for the damping of the oscillation amplitude over half a cycle. In the neighborhood of the fixed point we can use the linearization of the model around the fixed point to calculate κ. Assuming a two-dimensional spiral simple algebra leads to the formula

$$\kappa = \frac{p_{max} - p^*}{p^* - p_0} = e^{\frac{\pi\rho}{\omega}}, \tag{3.9}$$

where $\rho = Re(\lambda_i) < 0$ is the damping rate and $\omega = |Im(\lambda_i)|$ the typical rotation frequency around the fixed point. Note, that κ in (3.9) is independent of the the initial point p_0. Formula (3.9) holds for the two-variable Monod model and the corresponding computations for the Droop model are showed in the following.

One has to solve the eigenvalue and eigenvector problem for the Jacobian matrix

$$J(n,p,q) = \begin{pmatrix} -\delta - \frac{p}{(1+n)^2} & -\frac{n}{1+n} & 0 \\ 0 & (1-\frac{1}{q}) - (m+\delta) & \frac{p}{q^2} \\ \frac{\alpha}{(1+n)^2} & 0 & -1 \end{pmatrix} \tag{3.10}$$

in the Droop model (3.3) and assuming a flat spiral in phase space, *i.e.* $n_0 \simeq n(\pi/\omega) \simeq n^*$ and $q_0 \simeq q(\pi/\omega) \simeq q^*$, leads to the formula

$$\begin{aligned} \frac{p_{max} - p^*}{p^* - p_0} &= \frac{1}{\varepsilon}\left[\left(\frac{\lambda_2 - \lambda_3}{\lambda_1}\right) e^{\pi Re(\lambda_1)/\omega}\right. \\ &\quad \left. - \left(\frac{\lambda_3 - \lambda_1}{\lambda_2}\right) e^{\pi Re(\lambda_2)/\omega} - \left(\frac{\lambda_1 - \lambda_2}{\lambda_3}\right) e^{\pi Re(\lambda_3)/\omega}\right], \end{aligned} \tag{3.11}$$

where ω is the absolute value of the two non-zero $Im(\lambda_i)$ and

$$\varepsilon = (\lambda_2 - \lambda_3)/\lambda_1 + (\lambda_3 - \lambda_1)/\lambda_2 + (\lambda_1 - \lambda_2)/\lambda_3. \tag{3.12}$$

The corresponding results for the full Droop model are described by equation (3.11).

In Figure 3.1 and 3.4 numerically obtained values for the plankton overshooting κ in the unforced Droop model (3.3) are plotted in dependence on various control parameters. In general, maximal overshooting takes place for large algal mortality and comparatively small dilution rates.

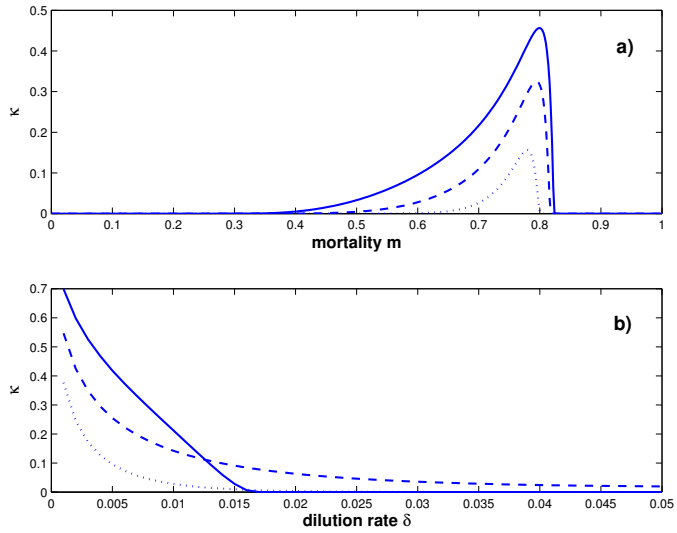

Figure 3.4: Overshooting as a function of mortality m and dilution rate δ, showing the measure of plankton overshooting κ calculated by equation (3.11). a) κ as a function of m for $\delta = 0.005$ (solid line) and $\delta = 0.01$ (dashed line), $\delta = 0.025$ (dotted line). b) κ as a function of δ for $m = 0.81$ (solid line), $m = 0.72$ (dashed line) and $m = 0.60$ (dotted line).

We want to stress that the overshooting measure κ is not restricted to chemostat models but holds as well for other systems with spiral dynamics, and therefore is applicable under quite general circumstances. In many practical situations the quantities of main interest are not only the equilibria of the system, but also the maximal abundance that can be attained by the system on its transition towards equilibrium. In such cases our simple formula (3.9) provides a comfortable method for the estimation of the amount of overshooting. This measure can also be of use in other systems with outbreak dynamics, in only requires that the fixed point of the system must be a stable spiral.

3.5 Chaotic dynamics

3.5.1 Introduction of external forcing

As far we could show that the unforced Droop model with the addition of algal mortality is able to reproduce a single phytoplankton bloom or outbreak. Now we show that with seasonal forcing the model shows recurrent outbreaks.

We now introduce external forcing into the model (3.3) by taking the input nutrient concentration $n_i(\tau)$ to be a periodic function of time. For simplicity, we choose a square

wave forcing where the external medium contains nutrients of concentration n_i^{max} during half of the forcing period T and is nutrient free in the rest of the time

$$n_i(\tau) = \begin{cases} n_i^{max} & \text{for} \quad kT \leq \tau < (k+\frac{1}{2})T \quad (k = 0, 1, 2, ..) \\ 0 & \text{otherwise.} \end{cases} \tag{3.13}$$

In our numerical simulations the periodic driving in general leads to forced oscillations of the algal abundance. However, in the presence of algal mortality also large parameter regimes with chaotic solutions are observed. A typical phytoplankton time series in the chaotic regime is shown in Figure 3.5a. Algal abundance undergoes recurrent outbreaks of irregular amplitude and timing. Figure 3.5b depicts the chaotic attractor. For better visualization the square root transformed variables are plotted. Successive maxima of the phytoplankton levels, p_{max}^n, follow a nearly one-dimensional return map (see Figure 3.5c). In the parameter range of Figure 3.5 the return map is piecewise continuous and build up from three branches, which correspond to the solutions with one, two, or three periods of forcing between two successive phytoplankton maxima. Notice, that the existence of a simple unique return map allows for a simple prediction of the height of future phytoplankton maxima.

Figure 3.5b reveals the mechanism of the chaotic dynamics. A typical 'cycle' starts with initially small numbers of phytoplankton and nutrients, *i.e.* in the lower left part of the (n, p)-phase plane. As soon as $n_i(\tau)$ is in the 'high' state, nutrients are linearly accumulated through external inflow. Since the input nutrient concentration is relatively large, $n_i^{max} \gg 1$ (see discussion below), the nutrient assimilation rate is soon saturated and the quota settles to the asymptotic value $q(t) \approx \alpha + 1$. At this stage the cells are sufficiently filled with nutrients and the reserves are used for cell divisions. Consequently, phytoplankton numbers slowly start to build up exponentially, $p = \exp \gamma t$, with a growth constant $\gamma = \frac{\alpha}{1+\alpha} - (m + \delta)$. This phase of exponential growth is clearly visible in the time series of Figure 3.5a and can also be verified by plotting phytoplankton numbers on a logarithmic scale. Multiplication of algal numbers continues until a certain threshold level is reached. This may take several cycles of nutrient forcing, since the amount of nutrients which are accumulated in one period is limited. As a result the state of the system moves upward in phase space in a characteristic zig-zag trajectory (see Figure 3.5b). With increasing phytoplankton numbers the nutrient consumption rises as well. In this critical stage, as soon as external nutrient supply, $n_i(\tau)$, switches to zero the nutrient reserves are used up very fast. Having consumed all its resources, the algal population declines rapidly and the trajectory in phase space spirals down into the left lower corner. The decline continues until the next nutrient pulse arrives. At this instant, nutrient levels start to rise again and the next cycle begins. The time which is needed by the phytoplankton population to reach threshold depends sensibly on the initial phytoplankton levels and therefore also on the last maximal levels p_{max}. This memory effect is responsible for the chaotic dynamics and gives rise to the simple return map of p_{max} (see Figure 3.5c).

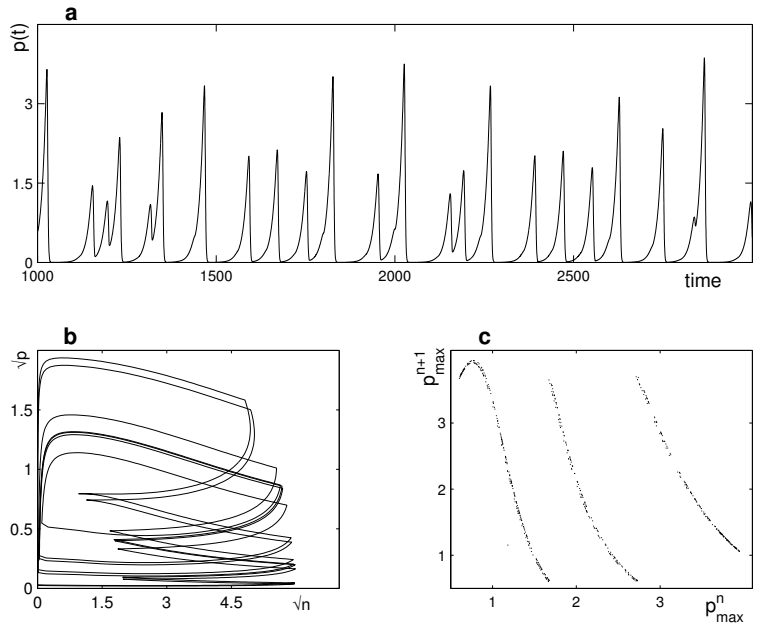

Figure 3.5: Typical simulation result of the forced system in the chaotic regime. a) Time series of phytoplankton $p(\tau)$, b) chaotic attractor in the (n,p) phase plane (square root transformed variables), and c) return map of successive phytoplankton maxima p_{max}. Parameter values are $T = 40$, $\delta = 0.11$, $m = 0.64$, $\alpha = 5$ and $n_i^{max} = 40$.

3.5.2 Bifurcation analysis

A first approach of this analysis is to study the influence of the forcing period on the chaotic regime. Figure 3.6 shows the bifurcation diagram obtained by varying the forcing period T. For small forcing periods the phytoplankton shows limit cycle oscillations. When T rises above a critical value a transition to the chaotic regime is initiated. In general, by increasing the forcing period the amplitude of oscillations is reduced and the average number of forcing cycles between two successive phytoplankton maxima increases. Finally, for very large forcing periods the chaotic regime is destroyed again. In figure 3.6 also the largest Lyapunov exponent, Λ, is plotted. The positive values of Λ for a large parameter range confirm that the irregular behavior of the algal numbers is indeed chaos. The parameter range with chaotic behavior is intersected by periodic windows. Note the exact correspondence of the regimes with positive Lyapunov exponent and irregular behavior in the bifurcation diagram. Concerning the computation of Lyapunov exponents with the Wolf-algorithm [138], we also explored the occurrence of hyperchaos in the hy-

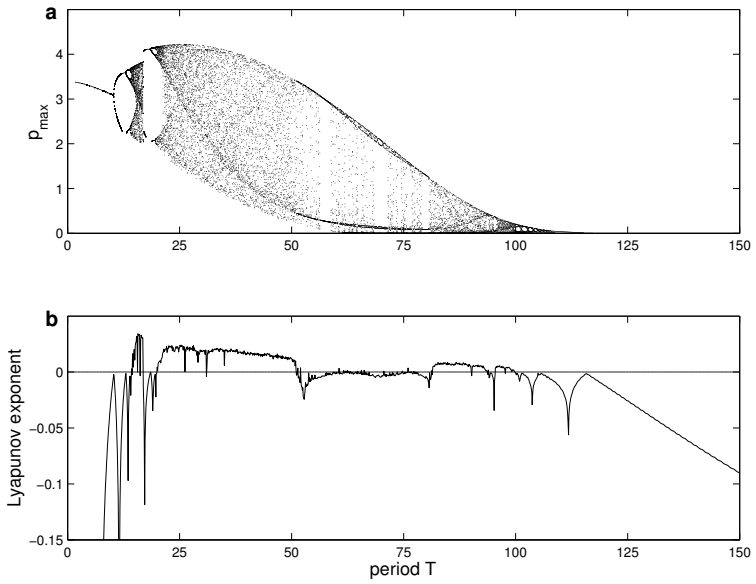

Figure 3.6: Bifurcation diagram. Plotted are a) the maxima of phytoplankton, p_{max} and b) the largest Lyapunov exponent computed with the Wolf algorithm (Wolf *et al.* 1985), in dependence on the forcing period T. Parameters otherwise as in figure 3.5.

perchaotic Rößler system in order to investigate the technical aspects of the algorithm. Our publication [135] about the dynamics in a new class of modified Rößler oscillators was the result of this work.

In order to investigate the size of the chaotic regions, in figure 3.7 we represent the largest Lyapunov exponent as a function of the two main forcing parameters, namely period of forcing T and forcing strength n_i^{max}. In general, chaotic behavior is found for a large range of forcing periods when n_i^{max} is sufficiently large.

In comparison, in figure 3.8 the largest Lyapunov exponent is plotted in the (m, δ)-parameter plane. Again we find a broad regime with chaotic solutions. Very similar chaotic behavior can be found in the forced Monod model (3.19) (see figure 3.8b for a comparison of the parameter regimes with chaotic behavior in the forced Droop and Monod models). Interestingly the chaotic domain corresponds very well to the parameter values which lead to a large overshooting of the unforced model, *i.e.* a large value of κ (compare to figure 3.1). This observation confirms that it is the possibility of spiral solutions of the unforced model which allows for chaotic dynamics under external driving. Due to the mortality, the system undergoes damped oscillations which interact with the external driving and generate complex dynamics.

One important questions concerns the realism of the parameter values with chaotic behavior for real experiments. As mentioned already the most crucial requirement for chaotic dynamics is the introduction of an additional algal mortality $m > 0$. Besides we have only been able to observe chaotic dynamics when the concentration of input nutrients is rather large, $n_i^{max} \gg 1$. This condition ensures that nutrient assimilation is saturated during the phase of exponential algal growth as explained above. Our numerical simulations show that n_i^{max} can be varied in a range of about 20% before chaos is lost. Even then, with a slight change of another parameter the chaotic behavior is retained, for example by reducing or enhancing the duration of a nutrient pulse for large or small values of n_i^{max}, respectively. Note, that the specific 'square-wave' forcing, which has been used, can easily be realized in the experiment. We have also investigated different forcing types, which in general lead to very similar results. However it seems to be crucial that the lower level of input nutrients is set very closely near zero. The chaotic regime is also robust towards modifications of the other parameters α and δ. In general, relatively small values of dilution rate δ are required for chaos. Further, we have observed chaotic dynamics in the full physiological range of $\alpha = 0.1 \cdots 50$. In the limiting case when α is very small, the Droop model goes over into the Monod model with rescaled parameters (see Appendix 1 and figure 3.8).

To summarize, the parameter range with chaotic domains is very broad and no pa-

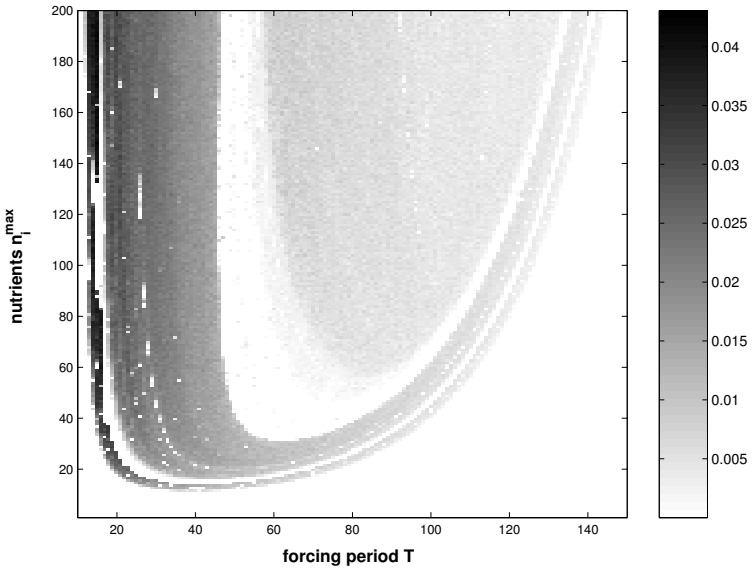

Figure 3.7: Largest Lyapunov exponent indicated as grey level in the (T,n_i^{max}) parameter plane for the Droop model (3.3). Parameters otherwise as in fig. (3.5).

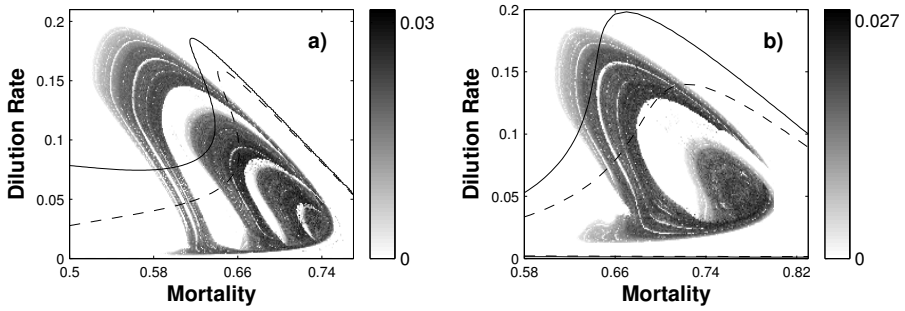

Figure 3.8: Largest Lyapunov exponent indicated as grey level in the (m,δ) parameter plane, for a) the Droop model (3.3) with $T = 40$, and b) the Monod model (3.19) with $T = 25$. Parameters otherwise as in fig. (3.5). Further indicated are lines with constant value of overshooting κ of the unforced model: a) solid line ($\kappa = 10^-6$), dashed line ($\kappa = 10^-3$) and b) solid line ($\kappa = 0.18$), dashed line ($\kappa = 0.25$)

rameter fine tuning is necessary to observe chaos. In our numerical simulations we have used parameter values which can easily be realized in chemostat experiments. For example, typical values of control parameters in dimensional units (Droop 1968; Grover 1991a, 1991b) such as $N_i^{max} = 400\,\mu\mathrm{mol}\,l^{-1}$, $D = 0.3\,d^{-1}$, $\mu_m = 2\,d^{-1}$, $\rho_m = 0.03\,\mu\mathrm{mol}\,d^{-1}$/cell, $K_\rho = 30\,\mu\mathrm{mol}\,l^{-1}$, $K_Q = 0.003\,\mu$mol/cell, $M = 1.2\,d^{-1}$ correspond to non-dimensional parameters of $\delta = 0.15$, $m = 0.6$, $n_i^{max} = 40, \alpha = 5$.

Another possible experimental obstacle are phytoplankton extinction events. Especially if many external forcing cycles are needed during a typical chaotic cycle, in our numerical simulations phytoplankton numbers undergo changes of several orders of magnitude. In a chemostat with limited size this leads to the danger that phytoplankton goes extinct. However, in typical parameter ranges algal changes are in the range of 4 or 5 orders of magnitude which is easily sustained in a chemostat which may contain algal densities of up to $10^7\,l^{-1}$ - $10^8\,l^{-1}$.

In order to test the robustness of the chaotical behavior, we submit our model to different transformations. We first present two variations of the Droop model (3.1) which have more realistic uptake and growth functions. The results for the chaotic dynamics in the Droop model also hold for these modified models. The first model considers only the modified growth function

$$\mu(Q) = \mu_m \left(\frac{Q - Q_{min}}{K_\mu + (Q - Q_{min})} \right). \tag{3.14}$$

The second model takes into account the physiological adaptation of the algae to the variations of nutrients concentration. The uptake and growth functions become in this

case

$$\rho(N,Q) = \left[\rho_{max}^{hi} - (\rho_{max}^{hi} - \rho_{max}^{lo})\left(\frac{Q - Q_{min}}{Q_{max} - Q_{min}}\right)\right]\left(\frac{N}{K_\rho + N}\right) \tag{3.15}$$

$$\mu(Q) = \left(\frac{\rho_{max}^{lo}}{Q_{max} - Q_{min}}\right)\left(1 - \frac{Q_{min}}{Q}\right) \tag{3.16}$$

where Q_{min} and Q_{max} are the minimal and maximal cell quota, respectively, and ρ_{max}^{lo} and ρ_{max}^{hi} the minimal and maximal uptake rate.

Choosing other types of forcing (modification of the duration and height of nutrients pulses, sine forcing...) also do not perturb the system very much. It stays in its chaotical regime. The only point one has to be careful with is the value of the low level of nutrients, which has to be nearly zero. After having introduced all these modifications, we are now left with the study of the influence of noise. Noise has been put in the system by replacing the growth rate and/or the uptake rate by a Gaussian distribution. This is very sensible when one thinks that all algae are not strictly identical and that each organism is growing at its own speed. It is found that noise tends to enlarge the parameter domain of chaos. As a conclusion, one can affirm that the model is quite robust toward changes which make it more realistic.

3.6 Conclusion

In this chapter we studied the dynamics of the periodically forced Droop model with an additional algal mortality. Recent chemostats studies have mostly focused on experiments with more than one species, either as competition studies or in predator-prey, i.e. nutrient-phytoplankton-zooplankton, cultures [76, 40, 59]. However, due to the complexity of such systems these experiments are often difficult to perform and the measured time series not easy to interpret. In contrast, single species chemostats are usually thought to give rise to only very poor dynamics. For example, it has been proven that for $m = 0$ the Droop model cannot exhibit chaotic dynamics [53, 56]. Here, we have shown that even simple nutrient-phytoplankton cultures are able to exhibit complex behavior. With the introduction of mortality the eigenvalues of the Jacobian matrix of the unforced system can become complex numbers, which allows the system to undergo damped oscillations before reaching equilibrium. Chaotic dynamics results upon the interaction of these damped oscillations with the time periodic environment.

As mentioned in the introduction, in the context of a continuous chemostat algal mortality may be somewhat artificial, and in the laboratory experiment must be realized by addition of an auxiliary circuit which filtrates part of the algae. In real aquatic ecosystems, however, the loss of algae from the epilimnion is of great relevance and arises mainly due to grazing by zooplankton and sinking into the deeper water layers. For example, it is well

known that sinking algae act as a carbon pump and have a major impact on the global CO_2-cycle and climate regulation. Also external nutrient forcing becomes a realistic feature due to seasonal nutrient inflow and up-welling. In this sense the chaotic outbreaks of phytoplankton numbers in the forced chemostat model may have some significance for real aquatic ecosystems where they would represent recurrent algal blooms. Similar results have been found in other simple models of bottom-up controlled phytoplankton systems [36, 71, 44]. Furthermore, taking all theses effects into account externally forced chemostats with additional mortality represent a simple yet realistic and controllable idealization of an aquatic system. In this respect our results are important for the design of new experiments.

Our results give insight into the dynamics of nutrient imitated growth in a time-varying environment and contribute to the significance of chaos in ecology. We suggest a simple model system which in principle allows to experimentally test for chaos and thus, should be of relevance for the understanding and role of deterministic chaos in ecological systems.

Appendix A: Transition to the Monod model

In some limiting biological case adiabatic elimination techniques can be applied to reduce the Droop model (3.3) to the more simplistic Monod model. We start with the analytical solution for $q(\tau)$:

$$q(\tau) = 1 + \frac{\alpha n(\tau)}{1+n(\tau)} + \left[q(\tau_0) - 1 - \frac{\alpha n(\tau_0)}{1+n(\tau_0)}\right] e^{-(\tau-\tau_0)}$$
$$-\alpha e^{-\tau} \int_{\tau_0}^{\tau} e^{\tau} \frac{\dot{n}(\tau)}{(1+n(\tau))^2} d\tau. \tag{3.17}$$

If the parameter α is very small, $\alpha \ll 1$, it can be shown that the last two terms vanish after a time $\tau \gg 1$. The assumption $\alpha = \rho_m(\mu_m K_\rho)^{-1} \ll 1$ corresponds to the limiting case where the maximal uptake rate μ_m is much larger than the maximal growth rate ρ_m. This means that after a time scale $t \gg \mu_m^{-1}$, which corresponds to the typical time needed for cell division the quota are related to the nutrients with the functional dependence

$$q(\tau) \approx 1 + \frac{\alpha n(\tau)}{1+n(\tau)}. \tag{3.18}$$

Inserting equation (3.18) into the second one of (3.3) and making the approximation $\alpha \ll 1$ leads to Monod's equations

$$\dot{s} = \frac{ds}{d\tau'} = \delta'(n_i - s) - \frac{sx}{1+s}$$
$$\dot{x} = \frac{dx}{d\tau'} = \frac{sx}{1+s} - (m' + \delta')x \tag{3.19}$$

with the following rescaled variables

$$s = n,\ x = \frac{p}{\alpha},\ \delta' = \frac{\delta}{\alpha},\ m' = \frac{m}{\alpha},\ \tau' = \alpha\tau. \tag{3.20}$$

Chapter 4

Epidemics Outbreaks

4.1 Background

Different approaches in the study of the dynamics of infectious diseases have been performed in the last ten years. Depending on the type of disease which is studied or the type of information one wants to obtain, stochastic [81, 88, 92, 97] or deterministic [90, 94, 100, 84, 98] models can be used. The relation between stochastic and deterministic models was made in [95]. The spatial aspect [87, 93] is introduced into the models by the concept of networks. Social networks can be used to understand the dynamics of diseases like AIDS for example [82, 91]. Larger space-scales can be taken into account by considering networks of populations [96, 99, 101, 102] (consider for example that the populations belong to distinct cities). Also theoretical questions can be studied with the help of the dynamics of epidemics. The idea of extinction risk [103, 94] or interaction between diseases [84, 86] are examples of these questions.

Our approach is inspired by a classical set of epidemiological data. These are time series of measles in 60 cities of the United Kingdom (see Figure 4.1). They were recorded from 1944 to 1967 with a sampling rate of 2 weeks. This data has been studied in [85]. They find that the epidemics outbreaks between cities where strongly synchronized and their amplitudes completely uncorrelated. They also observed a 2-year periodic cycle in the dynamics of the outbreaks. We choose to look at the problem on a large space-scale. We therefore consider networks of cities having different sizes. The well-known annually forced SIR-model is used to describe the dynamics of epidemics in a single city. In order to study a network of SIR-models, we introduce the coupling between two cities through their respective population size. The topology of the network is then generated from the distribution of these sizes. The interplay between the local dynamics of the individual systems and the global dynamics of the network is analyzed using symbolic dynamics [132, 136]. This method permits to consider only essential properties of the dynamics of

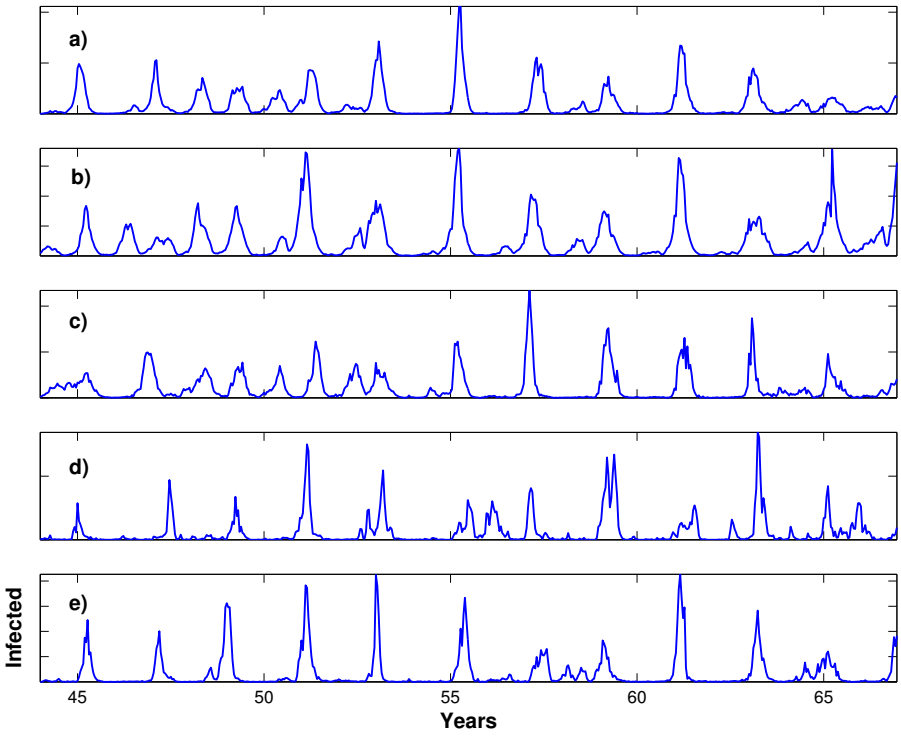

Figure 4.1: Time series of the number of children infected by measles in England/Wales. The data were recorder in the pre-vaccination tine with a sampling rate of 2 weeks. a) Birmingham, b) London, c) Newcastle, d) Cambridge and e) Southampton.

the systems. This simplification is a convenient way to look for synchronization of the maps in the network. The symbolic dynamics is directly derived without any parameterization from the topology of the attractor of the SIR-model. We will also show that the SIR-model will reduce to a simple 1-dimensional asymmetric tent map. The next chapter will be devoted to the study of complex dynamics in networks of chaotic maps with distributed sizes.

Considering the coupling of the SIR-models, we derive a very generic type of coupling function based on the sizes of the individual systems. The sizes of the systems are generated from some distribution function and may change several orders of magnitude. Depending on the distribution function, different types of topologies will be generated. We study the interplay between the topology of the network and the global dynamics. We show that our coupling tends to stabilize a global 2-year cycle, as observed in data. Our findings include a whole class of natural systems, from tree masting [111, 112] to the coupling of

lasers.

4.2 The SIR-model

This epidemiological model takes into account three classes of individuals: susceptible people S who are healthy persons, infected people I who are infectious and recovered people R. The seasonal forcing is introduced into the model by assuming that the contact rate between the individuals (children in the original problem) depends on the rhythm of school- and holiday-time.

The forced SIR-model reads

$$\begin{aligned} \dot{S} &= \mu N - \mu S + \frac{\beta(t)}{N} S(I + wI_0) \\ \dot{I} &= \lambda \frac{\beta(t)}{N} S(I + wI_0) + (\mu + \gamma) I \\ \dot{R} &= \mu R + \gamma I \end{aligned} \tag{4.1}$$

where

$$\beta(t) = \beta_0 (1 + \delta \sin 2\pi t) \tag{4.2}$$

is the periodically forced contact rate, β_0 the unforced contact rate, δ the variability of the contact rate, N the size of the population, μ the birth rate of the population, γ is the recovery rate (inverse of the recovery time t_R), I_0 the mean-field of infected people belonging to other populations and w_0 the coupling strength to this mean-field. λ is a proportionality constant which is derived from the complete $SEIR$-model [80, 83, 94]. This model takes into account the supplementary class E of exposed people who caught the disease but are not infectious. The $SEIR$-model takes into account the incubation time of the disease. If the incubation time is very short compared to the time-scale of the epidemics, the $SEIR$-model reduces to the SIR-model [100, 83]. Note the structural similarity of the SIR-model with the generic outbreak model (2.5) in the part 2.2.2.

In the case where we start our study directly with the SIR-model, this constant can be set to $\lambda = 1$ and the total population size $S + I + R = N$ is then a constant of motion. The parameter of the disease are very well known for measles: $\mu = 0.02$ and $\gamma = 45$. The other parameters are set to $N = 1$, $w_0 = 0.0002$, $I_0 = 0.00045$, $\beta_0 = 1200$ and $\delta = 0.2$. Because the variable R will not play a role in the study we perform, we will simply drop it in the following.

Figure 4.2 shows a typical time series of the model (4.1) in the chaotic regime. The system shows periodic outbreaks of epidemics. There is a great variability in the amplitude of the outbreaks and they occur annually or bi-annually at the same time in the year. Due to the forcing of the model, the phase of the dynamics is perfectly defined. The model posses an interesting dynamics and its attractor is represented in the phase space

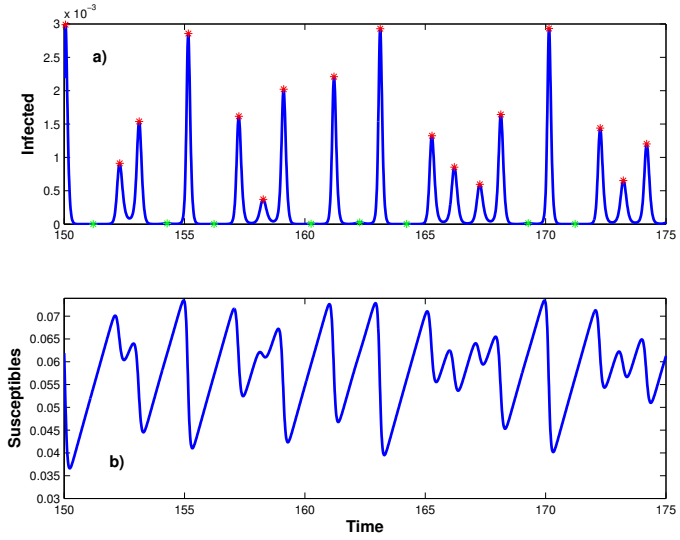

Figure 4.2: Typical behavior of the forced model SIR-model (4.1). Time series of a) the infected I and b) the susceptibles S. The red stars correspond to major outbreaks of epidemics and the green stars to minor ones. The parameters are $\mu = 0.02$, $\gamma = 45$, $\lambda = 0.625$, $N = 1$, $w_0 = 0.0002$, $I_0 = 0.00045$, $\beta_0 = 1200$ and $\delta = 0.2$.

(S, I) in Figure 4.3. We call this attractor 'tooth attractor' because of its shape. The dynamics is composed of a succession of 1- and 2-year cycles. A cycle starts when the number of infected people is very low, that means when a previous epidemics just finished. The susceptibles then linearly accumulate up to a certain threshold where the number of infected people suddenly grow exponentially. This is the mechanism of yearly occurring outbreaks (1-year cycle). But it can also happen that the amount of susceptibles is not high enough to trigger the epidemics. The susceptibles still continue to accumulate and the epidemics will then only happen in the following year. This corresponds to a 2-year cycle which is composed of a very small outbreak (skip) followed by a large one. The difference in the amplitude of these outbreaks can be several order of magnitudes (see Figure 4.3). Let us notice that cycles having a period of 3 or more years cannot occur due to the small immigration term $w_0 I_0$ in the model (4.1). This term controls the minimal level of susceptibles in the system.

In the following section we explore different approaches to investigate the complex dynamics which is exhibited in the forced model (4.1). We first introduce the notion of symbolic dynamics and present some of the possibilities this method offers for the analysis of the dynamical properties of the system. We then show that the SIR-model can be a reduced to a one-dimensional map reproducing very-well the dynamics of the individual

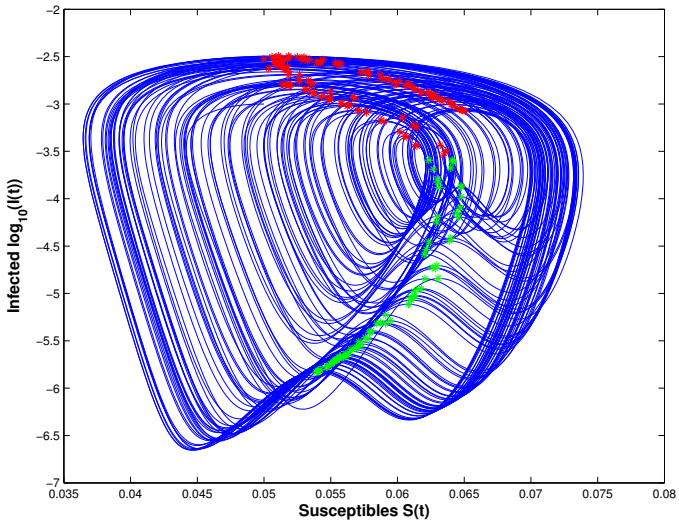

Figure 4.3: 'Tooth attractor' of the model (4.1) in the phase space $(S, log_{10} I)$. The red stars correspond to major outbreaks of epidemics and the green stars to minor ones. The parameters are as in Figure 4.2.

outbreaks (minor and major). Finally we explain how the network of SIR-models is generated from the different sizes of the cities.

4.3 Symbolic dynamics

Our final aim is to understand and to model the interaction of N cities, where each city i has a size n_i and is represented by an SIR-model. Having this goal at mind, it seems rather complex to consider the exact dynamics of the time series of the cities. One may then think to reduce the dynamics to its essential elements. We will only consider as an information in one year if it occurs or not an outbreak. We call '1' a major outbreak and '0' a minor one. This then permits to code the dynamics as a sequence of symbols occurring yearly $S_1 S_2 S_3 \dots S_n$, where S_n can be 0 or 1. This represents the symbolic dynamics, where an example can be '101101010...'. Let us also notice that the symbolic dynamics can be directly generated out of the topology of the tooth attractor (see Figure 4.3). A maxima of the infected corresponds to only two situations in the susceptibles. Either the susceptibles still grow and one gets a minor outbreak '0' or they decrease and it occurs an major outbreak '1'. The symbolic sequence is useful to study the prediction possibilities of a single system or the more global properties like synchronization in the network.

4.3.1 Transition probabilities

The symbolic dynamics is a powerful tool to get information out of the complex dynamics of a system [134, 136]. First we perform the computation from the symbolic sequences of the probability of occurrence $p(W_l)$ of each possible word W_l of length l, where $W_l = S_{n-l+1} \dots S_{n-1} S_n$. Out of the $p(W_l)$'s it is then possible to compute the conditional probabilities to a certain state S_n knowing the k earlier states $S_{n-k} \dots S_{n-2} S_{n-1}$. The formula giving the transition probabilities is the following

$$p(A|B) = \frac{p(A,B)}{p(B)} \Longrightarrow p(S_n|S_{n-k} \dots S_{n-2} S_{n-1}) = \frac{p(S_{n-k} \dots S_{n-2} S_{n-1} S_n)}{p(S_{n-k} \dots S_{n-2} S_{n-1})} \qquad (4.3)$$

where A is the expected state and B the known state (history of outbreaks). Figure 4.4 shows the time series from Figure 4.2 transformed into a symbolic sequence. For the realistic parameters given in the previous section, the probabilities computed from the symbolic sequence are

p(0)	0.39	p(00)	0	p(000)	0
p(1)	0.61	p(01)	0.39	p(001)	0
		p(10)	0.39	p(010)	0.24
		p(11)	0.22	p(011)	0.15
				p(100)	0
				p(101)	0.38
				p(110)	0.15
				p(111)	0.08

The transition probabilities can then be computed using the formula (4.3)

p(0|0)	0	p(0|00)	0
p(0|1)	0.37	p(0|01)	0.62
p(1|0)	1	p(0|10)	0
p(1|1)	0.63	p(0|11)	0.64
		p(1|00)	0
		p(1|01)	0.38
		p(1|10)	1
		p(1|11)	0.36

Because of problems of typographical representation the gave here only transitions probabilities up the second order, that means where two symbols in the past are known. These results will be plot in a more convenient way in the next section. The conditional probabilities give very important information about the outbreak dynamics of the system (4.1). They permit to predict the probability of occurrence of an outbreak knowing the history of the system. It is for example possible to quantify the tendency of a system to show limit-cycle behavior.

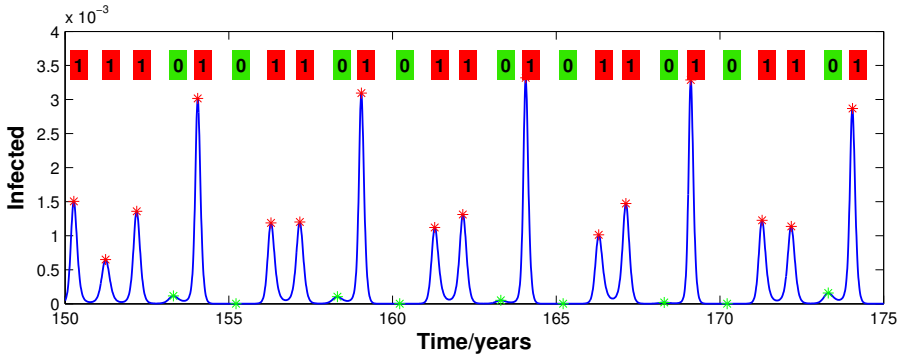

Figure 4.4: Time series of the number of infected people and symbolic sequence $S_0 S_1 \dots S_n$, where $S_n = 0, 1$. The parameters are as in Figure 4.2.

4.3.2 Block entropies

The block entropies are computed in order to evaluate the predictability of a system. The block entropy H_l is mean amount of information about the symbolic dynamics which is contained in a word of length l. The classical formula from information theory [132] gives for the block entropy

$$H_l = -\left\langle \log p(W_i^{(l)}) \right\rangle = -\sum_{i=0}^{2^l-1} p(W_i^{(l)}) \log p(W_i^{(l)}) \tag{4.4}$$

where the index i goes over all possible words of length l. The conditional entropy h_n is defined as the average information which is needed to predict the next symbol, given the preceding n symbols

$$h_n = H_n - H_{n-1} \tag{4.5}$$

Figure 4.5 shows a graphical representation of the conditional entropy for $n = 0 \dots 9$. We notice that the quantity h_n decreases monotonly with n and saturates to a value which is different from zero. This value represents the predictability limit of the sequence and occurs in our case for ca. $n = 5$. This means that one will not get more information about the future of the symbol knowing more then 5 symbols. This is a typical feature of chaotic dynamics, where the future state of the system cannot be perfectly known. For system showing regular dynamics (negative Lyapunov exponents), the conditional entropies h_n reaches zero for a finite n.

The symbolic dynamics is very useful to analyze coupled systems. It is for example possible to detect directionality or intensity of coupling using the concept of mutual transition probability. We explain this by considering two coupled systems. The mutual

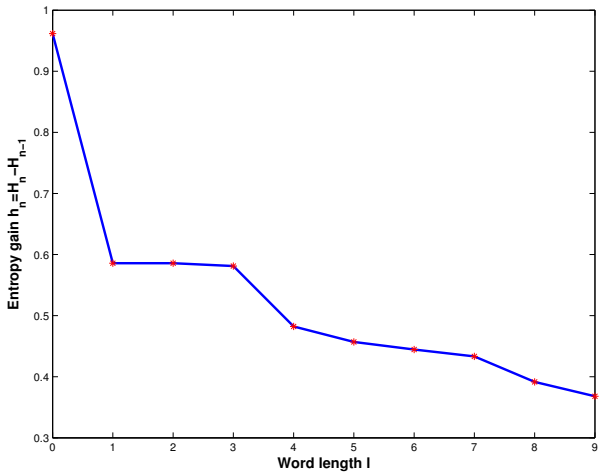

Figure 4.5: Plot of the conditional entropy (4.5). The symbolic sequence is extracted from the SIR-model with parameters are as in Figure 4.2.

transition probability gives the probability of being in some state in the system 1 knowing the actual or the past state of system 2. Here are examples of probabilities of this type:

$$p(S^1_{n+1} = 0, S^2_{n+1} = 1 | S^1_n = 1, S^2_n = 0)$$
$$p(S^1_{n+1} = 0 | S^1_n = 1, S^2_n = 0)$$
$$p(S^1_{n+1} = 0, S^2_{n+1} = 1 | S^1_n = 1)$$

We will use again the symbolic dynamics in the sections about the coupled SIR-models.

4.4 Reconstruction of attractors from data

We show in this section that it is possible to reconstruct the 'tooth attractor' (4.3) from the data of measles (see Figure 4.1 and `http://www.zoo.cam.ac.uk/zoostaff/grenfell/`). The time series of the infected people is known and the susceptibles can be then deduce from it. In fact, the symbolic dynamics can be generated out of the reconstructed data. This gives information about the synchronization of epidemics outbreaks between the cities in England/Wales. Let us notice here that the method of embedding [137] which is classically used to reconstruct chaotic attractors does not work here because of the alternation of 1- and 2-year dynamics. Therefore the phase of the system can not be univokely defined from the time series and the embedding algorithm is not applicable.

In order to reconstruct the susceptibles from the time series of the infected, let us

assume that the dynamics obeys the SI-model

$$\begin{aligned} \dot{S} &= \mu - \beta(t)SI \\ \dot{I} &= \beta(t)SI - \gamma I \end{aligned} \tag{4.6}$$

where we omitted the term μS which is very small compared to μ. The variable R describing the recovered people does not enter into the reconstruction. We then discretize this model following [129, 130]

$$\begin{aligned} S_{n+1} &= S_n + \mu - \beta_n S_n I_n \\ I_{n+1} &= I_n - \gamma I_n + \beta_n S_n I_n \end{aligned} \tag{4.7}$$

and assume that the temporal resolution of the data is good enough. This is in fact the case because our data have been recorded every two weeks, which is a small interval compared to the typical yearly time-scale of the dynamics. This means that there is no change of the number of infected due to growth and death rate of the population on the time-scale of two weeks

$$I_n = \gamma I_n. \tag{4.8}$$

The evolution equation for susceptibles becomes then

$$S_{n+1} = S_n + \mu_n - I_{n+1} \tag{4.9}$$

and recurrently the reconstructed number reads

$$S_{n+1} = -\sum_{j=1}^{n} (I_j - < I >) \tag{4.10}$$

where it was assumed that the dynamics is stationary

$$\mu_n \approx < I_n > . \tag{4.11}$$

The susceptibles are thus reconstructed by integrating (summing) the number of infected people and removing a trend. This trend comes from the fact that the data is noisy and that the integration gives in this case a random walk. It is possible to remove the trend because the time-scale of the trend is larger than the time-scale of the outbreaks (see Figure 4.6b). An example of the results of this procedure is shown for the city of Birmingham in Figure 4.6. The extracted attractor is plot in Figure 4.7 and is very similar to the tooth attractor. The data was smoothed using the technique of moving average.

After reconstruction of the susceptibles it is possible to generate the symbolic dynamics for the real infected data. Figure 4.8 shows a graphical representation of the sequences of symbols. We can see that there is an obvious bi-annually dynamics of the epidemics outbreaks. Most of the cities are synchronized when outbreaks occurs. The computation of the transition probabilities (averaged over the 60 cities) gives

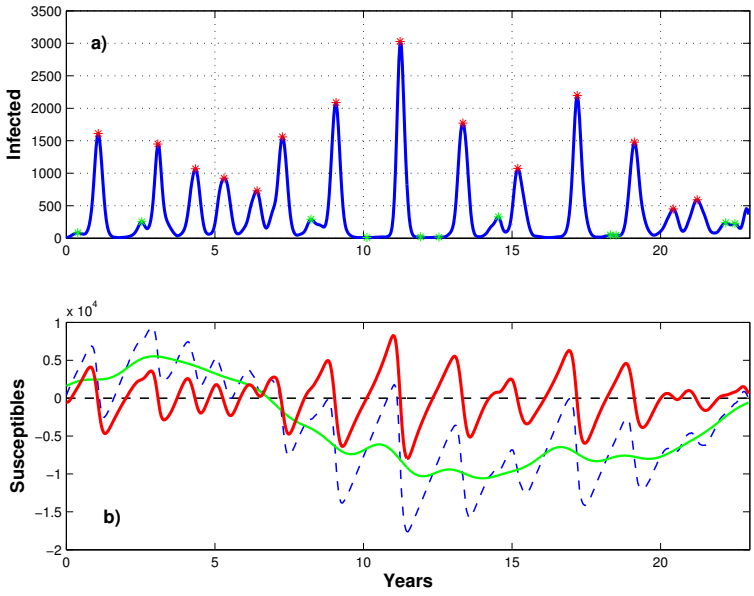

Figure 4.6: a) Time series of data of infected people in Birmingham. The red stars are outbreaks and the green ones are skips. b) Reconstruction of the susceptibles. The blue dashed line is the direct result, the solid red line is the untrended result and the green line is the trend.

p(0|0)	0.02	p(0|00)	0
p(0|1)	0.49	p(0|01)	0.69
p(1|0)	0.98	p(0|10)	0.02
p(1|1)	0.51	p(0|11)	0.67
		p(1|00)	0
		p(1|01)	0.31
		p(1|10)	0.98
		p(1|11)	0.33

We see from the first order probabilities that the prediction of the next is not good when an outbreak occurs in the previous year. There is a fifty percent chance of having or not an outbreak. The second order shows that the probability of having a 2-year cycle of outbreaks is very high. Note, the remarkable well agreement of these transition probabilities to that calculated from the forced SIR-model. We will use again the symbolic dynamics in the section devoted to the analysis of networks of SIR-models.

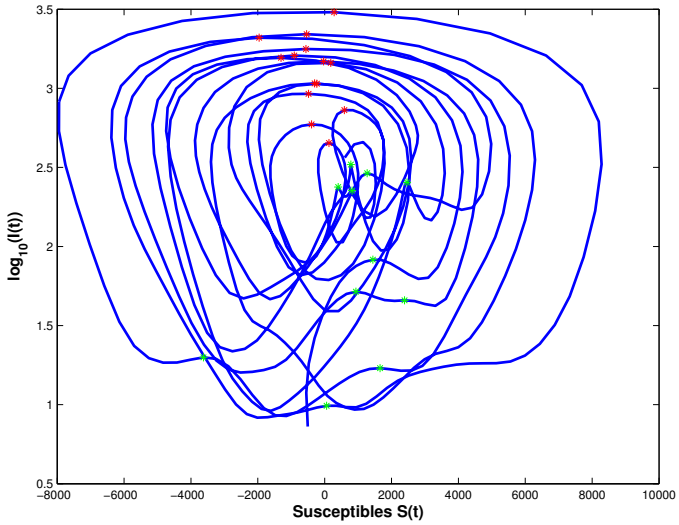

Figure 4.7: Reconstruction of the attractor of the system for the data from the city of Birmingham. The red stars are outbreaks and the green ones are skips.

4.5 Reducing the SIR-model to an asymmetric tent map

We show in this section that the SIR-model (4.1) can be reduced to a one-dimensional map by taking a particular Poincaré section. The map can be generated in different ways. The classical approach is to plot the return map of relevant quantities in the system, for example the maxima or the minima of the variables. We find out that only the return map of the minima of the susceptibles gives a piece-wise continuous map. This map fullfils the conditions for a dynamical system. We plot the return map in fig. (4.9.a) and fig. (4.9.b) shows the time interval between two successive minima. One can see from this figures that the map does not only iterate one step (year) in the future, but can also project two steps in the future. This is a problem which can be solve by considering that it exists a map which always iterates one step.

Our map has the form

$$\begin{cases} x_{n+1} = G_1(x_n) & , \text{ if } \quad x_n \geq x_t \\ x_{n+2} = G_2(x_n) & , \text{ if } \quad x_n < x_t \end{cases} \tag{4.12}$$

and we are looking for a map of the type

$$x_{n+1} = f(X_n) = \begin{cases} F_1(x_n) & , \text{ if } \quad x_n \geq x_t \\ F_2(x_n) & , \text{ if } \quad x_n < x_t \end{cases} \tag{4.13}$$

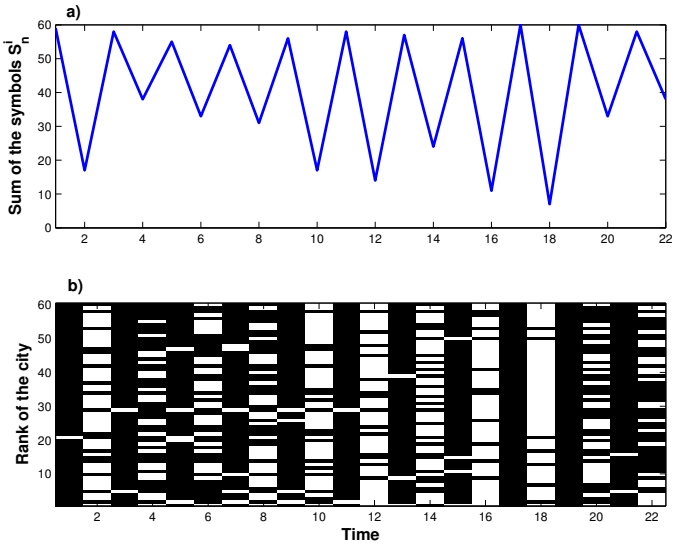

Figure 4.8: Representation of the symbolic dynamics generated from the data of measles in Great Britain. Plot of the a) sum of symbols over all cities and b) symbol sequences for each city. Black means outbreak and white means skip. The cities are sorted by sizes on the y-axis.

where x_t is a threshold which is identical for both maps. Obviously $F_1(x_n) = G_1(x_n)$, so that the right piece of the map is known. The part $F_2(x_n)$ can be deduced from the fact that the composition of F_1 and F_2 has to iterate two steps in the future

$$G_2 = F_1 \circ F_2. \tag{4.14}$$

This leads to

$$F_2 = F_1^{-1} \circ G_2 \Longleftrightarrow F_2(x_n) = F_1^{-1}(G_2(x_n)) \tag{4.15}$$

which can directly be computed out of the time series of the minima of the susceptibles (see Figure 4.10a).

The map which is obtained is an asymmetric tent map

$$f(x) = \begin{cases} 1 - rx & \text{for } x \geq 0 \\ 1 + qx & \text{for } x < 0 \end{cases} \tag{4.16}$$

where x represents the density of susceptibles. The domain $x \geq 0$ corresponds to the outbreak '1' of an epidemics and $x < 0$ to a skip '0'. It is found that the optimal fit leads to the parameters $q = 0.8$ and $r = 2$. The Poincaré section which represents a plane of constant phase is shown in Figure 4.10b.

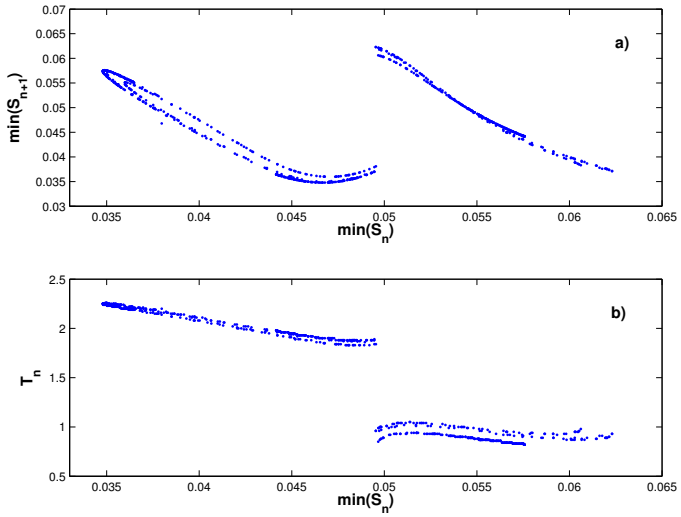

Figure 4.9: a) Return map of the minima of the susceptibles and b) time interval between two minima. The time series were generated with the SIR-model with parameters as in Figure 4.2.

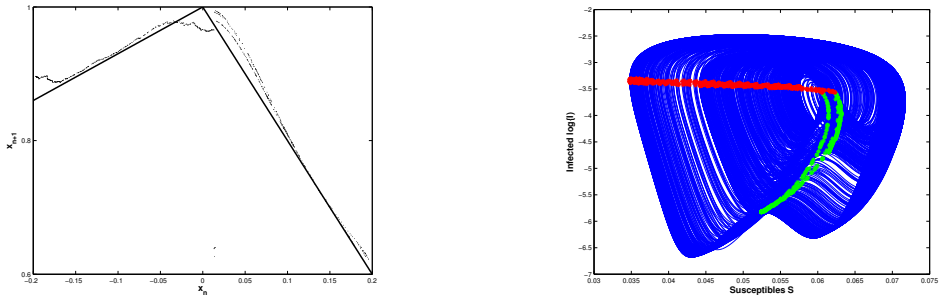

(a) (b)

Figure 4.10: Picture left: Construction of $F_2(x_n)$ and fit of the asymmetric tent map. Picture right: the Poincaré section. The parameters are as in Figure 4.2.

4.6 Introducing the coupling between cities

In this section we introduce the notion of spatiality into the framework of the SIR-model. This problem has been studied in [83, 87, 93] from the meta-population point-of-view, but without any internal structure. That means that the meta-populations are globally coupled and that the coupling strength does not depend for instance on distances or network topology. Therefore we consider a network of cities having different sizes and where the dynamics of each city is represented by a single SIR-model. Introducing the

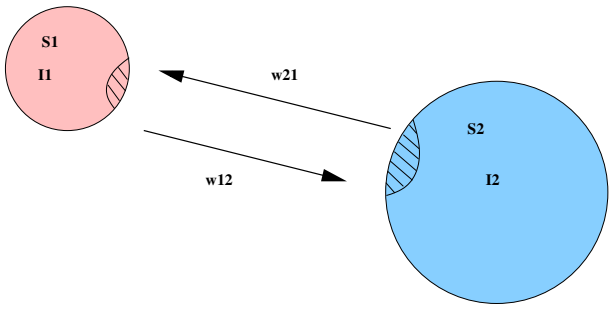

Figure 4.11: Schematic representation of the coupling between two cities. A fraction w_{12} and w_{21} of the population travels from the city 1 to the city 2 and *vice versa*. $S_{1,2}$ and $I_{1,2}$ represent the number of susceptible and infected persons, respectively.

city size into the model is a very realistic feature when one thinks about Zipf's law [25]. This law says that the sizes of the cities obey a power-law distribution. We first derive the coupling function for a system of two cities and after that extend the problem to N coupled SIR-models. The dynamics will be analyzed using the concept of symbolic dynamics which was developed previously.

4.6.1 Simple case of 2 cities

In order to introduce the coupling between two cities, we assume that a small fraction of the population of each city travels to the other city. Furthermore we assume that the time that individuals are in the other city is small compared to the yearly time-scale of the epidemics dynamics. The fraction of the population w_{ij} $(i, j = 1, 2)$ which is moving from city i to city j can be a constant or can also depend on some parameters. These parameters may be the distances d_{ij} between the cities, the travel probabilities $p(j \to i)$ or the attractivity of a city. Figure 4.11 shows a schematic representation of two cities.

We can make two hypothesis to construct the model: a) either the epidemics is only propagated through the traveling of infected people or b) it is also propagated through the motion of infected and susceptible people. But whatever assumption is made, the core of the coupled model will be the SIR-model.

a) Only infected people are traveling

We first consider the case of the city 1 and all the computations will be then identical for the city 2. We replace in the SIR-model the variable describing the infected people I_1 by an effective number of infected individuals

$$I_1 \longrightarrow I_1 + w_{21} I_2 \tag{4.17}$$

which also contains the infected persons I_2 who are located in the city 1. This leads to the new model

$$\begin{aligned}\dot{S}_1 &= \mu N_1 - \mu S_1 - \frac{\beta(t) S_1}{N_1}\left(I_1 + w_{21} I_2\right) \\ \dot{I}_1 &= \frac{\beta(t) S_1}{N_1}\left(I_1 + w_{21} I_2\right) - (\mu+\gamma) I_1\end{aligned} \tag{4.18}$$

which can be re-written in dimensionless units (that means densities)

$$\begin{aligned}\dot{s_1} &= \mu - \mu s_1 - \beta(t) s_1 \left[i_1 + w_{21}\left(\frac{N_2}{N_1}\right) i_2\right] \\ \dot{i_1} &= \beta(t) s_1 \left[i_1 + w_{21}\left(\frac{N_2}{N_1}\right) i_2\right] - (\mu+\gamma) i_1\end{aligned} \tag{4.19}$$

using the transformation

$$s_1 = \frac{S_1}{N_1}, \quad i_1 = \frac{I_1}{N_1} \tag{4.20}$$

where N_1 and N_2 are the sizes of the cities.

We obtain the equations for the city 2 in an identical way

$$\begin{aligned}\dot{s_2} &= \mu - \mu s_2 - \beta(t) s_2 \left[i_2 + w_{12}\left(\frac{N_1}{N_2}\right) i_1\right] \\ \dot{i_2} &= \beta(t) s_2 \left[i_2 + w_{12}\left(\frac{N_1}{N_2}\right) i_1\right] - (\mu+\gamma) i_1\end{aligned} \tag{4.21}$$

We see that the coupling strength between the two cities depends on the traveling fractions w_{ij} and the ratio $r = n_2/n_1$ of the city sizes. The direction of the coupling is given by the ratio r. That means that a large city will influence much more a small one than the other way around.

In order to analyze the dynamics occurring in this system, we will use the concept of symbolic dynamics developed previously. We introduce the similarity index

$$\Gamma = \left\langle |S_n^2 - S_n^1| \right\rangle_n = \frac{1}{T}\sum_{n=1}^{T} |S_n^2 - S_n^1| \tag{4.22}$$

to measure the synchronicity (anti- and in-phase) of the dynamics. The synchronization regime corresponds to $\Gamma = 0$, anti-synchronization to $\Gamma = 1$ and no synchronization to $\Gamma = 0.5$. It can be shown that this measure is proportional to the correlation of the symbolic sequences [134]. We use the similarity instead of the correlation because it will be much more convenient to study the case of N coupled systems.

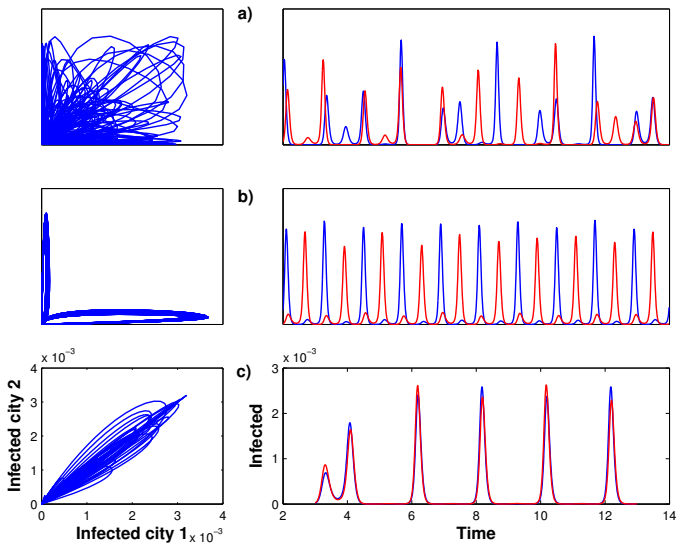

Figure 4.12: Left colum: population of infected people in city 1 *vs.* city 2. Right colum: time series of the infected in city 1 and city 2. The ratio is $r = 0.631$ and the coupling strength is a)$w = 0.0005$, b)$w = 0.0048$ and c)$w = 0.015$. The parameters of the SIR-model are as in Figure 4.2.

For the simulations we assume that the individuals do not have preferential travel destination and that both populations are equally attracted by the other city. Therefore we set $w_{12} = w_{21} = w$, where w is the coupling strength. We show in Figure 4.12 the three typical states which can occur in this system. Each state corresponds to a typical range of the coupling strength. The dynamics in both cities are uncorrelated for small w, intermediate w leads to an anti-synchronized state and the cities are synchronized for large w. It is interesting to notice that all these states take place in a chaotic regime. Figure 4.13 shows the continuous transition between these states in function of the coupling strength w. Also the largest Lyapunov exponent is plotted.

b) Infected and susceptible people are traveling

In the previous paragraph the epidemics was only propagated through the movement of infected. We assume furthermore here that the susceptible can be infected when traveling in another city.

The model for the city 1 then reads

$$\dot{S}_1 = \mu N_1 - \mu S_1 - \frac{\beta(t)}{N_1} S_1 I_1 - \frac{w_{21}\beta(t)}{N_1} S_1 I_2 - \frac{w_{12}\beta(t)}{N_2} S_1 I_2$$

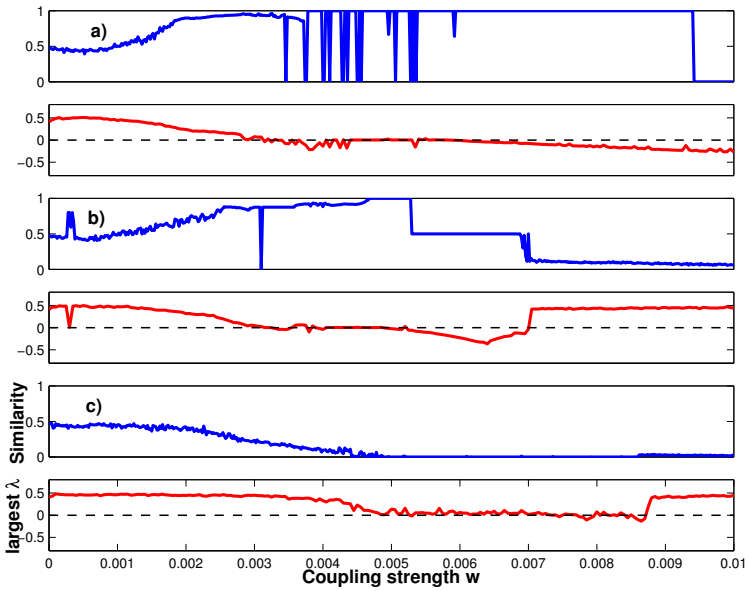

Figure 4.13: Bifurcation diagram of the similarity index and plot of the largest Lyapunov exponent in function of the coupling strength w. The ratio is a) $r = 1$, b) $r = .631$ and c) $r = .321$. The parameters of the SIR-model are as in Figure 4.2.

$$\dot{I}_1 = \frac{\beta(t)}{N_1} S_1 I_1 + \frac{w_{21}\beta(t)}{N_1} S_1 I_2 + \frac{w_{12}\beta(t)}{N_2} S_1 I_2 - (\mu + \gamma) I_1 \tag{4.23}$$

and in dimensionless variables becomes

$$\begin{aligned} \dot{s_1} &= \mu - \mu s_1 - \beta(t) s_1 \left[i_1 + \left(w_{21} \left(\frac{N_2}{N_1} \right) + w_{12} \right) i_2 \right] \\ \dot{i_1} &= \beta(t) s_1 \left[i_1 + \left(w_{21} \left(\frac{N_2}{N_1} \right) + w_{12} \right) i_2 \right] - (\mu + \gamma) i_1 \end{aligned} \tag{4.24}$$

A similar computation for the city 2 leads to

$$\begin{aligned} \dot{s_2} &= \mu - \mu s_2 - \beta(t) s_2 \left[i_2 + \left(w_{12} \left(\frac{N_1}{N_2} \right) + w_{21} \right) i_2 \right] \\ \dot{i_2} &= \beta(t) s_2 \left[i_2 + \left(w_{12} \left(\frac{N_1}{N_2} \right) + w_{21} \right) i_2 \right] - (\mu + \gamma) i_2 \end{aligned} \tag{4.25}$$

These results are perfectly coherent with the equations which have been derived independently in [93]. The authors used a mechanistic model and considered eight distinct

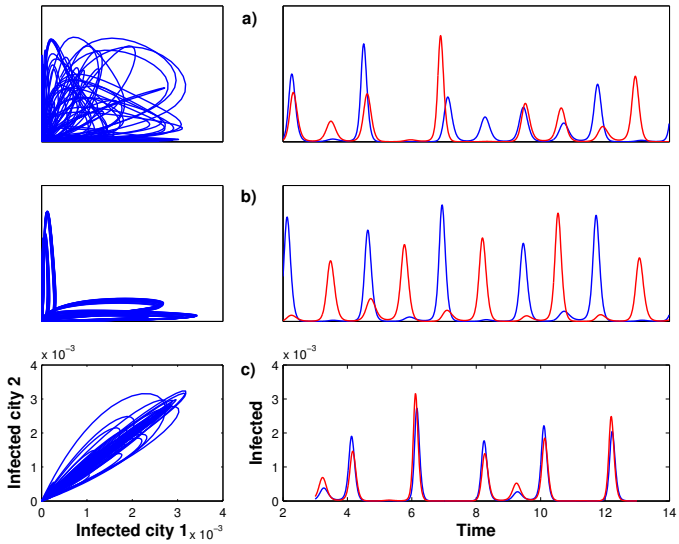

Figure 4.14: Left colum: population of infected people in city 1 *vs.* city 2. Right colum: time series of the infected in city 1 and city 2. The ratio is $r = 0.631$ and the coupling strength is a)$w = 0.0005$, b)$w = 0.0015$ and c)$w = 0.007$. The parameters of the SIR-model are as in Figure 4.2.

populations of susceptible and infected, representing the people who are sojourning in another city. Their model approaches our own one when the sojourning time tends to zero.

We make in Figure 4.14 and 4.15 the same analysis as for the model where only the infected propagate the epidemics. We observe that the more realistic model shows exactly the same behavior. Transitions from a non synchronized state ($\Gamma = 0.5$), through an anti-synchronized state ($\Gamma = 1$) to finally end up in a fully synchronized state ($\Gamma = 0$) occur when the coupling strength w is increased. Even the coupling ranges of the different regimes are very similar to the simpler model.

Let us consider the case of intermediate coupling strength in order to understand the effect of the size ratio $r = n_2/n_1$. When the cities have comparable sizes, the systems behave like spins and tends to be in an anti-synchronized regime. When one city is much larger or smaller than the other one ($r \gtrsim 3$ or $r \lesssim 1/3$, respectively), there is no real anti-synchronized state and the system goes directly into a synchronized regime.

Since the conclusions are extremely similar for both models, we decide to use in the following only the model (4.19) where only the infected people spread the epidemics. This choice is also motivated by the fact that putting some noise on the systems smoothes the bifurcation diagrams (4.13) and (4.15) and eliminates all the small differences. This

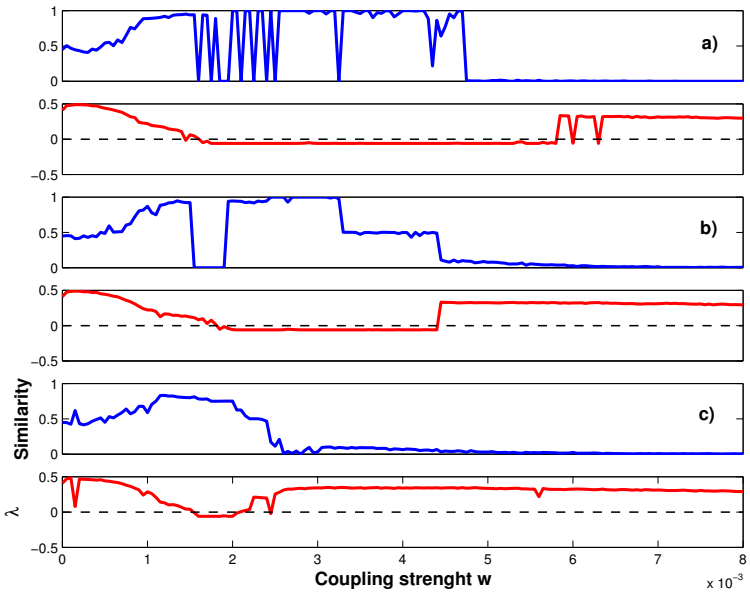

Figure 4.15: Bifurcation diagram of the similarity index and plot of the largest Lyapunov exponent in function of the coupling strength w. The ratio is a) $r = 1$, b) $r = .631$ and c) $r = .321$. The parameters of the SIR-model are as in Figure 4.2.

approach has also been adopted in [83].

4.6.2 Size distribution and network of cities

We consider in this section a set of N cities represented each by an SIR-models and coupled through their size. Extending the model (4.19) to N systems leads to

$$\begin{aligned} \dot{s_k} &= \mu - \mu s_k - \beta(t) s_k \left[i_k + \sum_{l \neq k} w_{lk} \left(\frac{N_l}{N_k} \right) i_l \right] \\ \dot{i_k} &= \beta(t) s_k \left[i_k + \sum_{l \neq k} w_{lk} \left(\frac{N_l}{N_k} \right) i_l \right] - (\mu + \gamma) i_k \end{aligned} \tag{4.26}$$

where $k, l = 1 \ldots N$.

If we assume that the individuals travel to each city with equal probability and do not show any preferences for a city, the traveling fraction w_{kl} for all cities will be identical,

that means $w_{kl} = w$. The system (4.26) can then be written as

$$\dot{s_k} = \mu - \mu s_k - \beta(t) s_k \left[i_k + w \sum_{l \neq k} \epsilon_{lk} i_l \right]$$

$$\dot{i_k} = \beta(t) s_k \left[i_k + w \sum_{l \neq k} \epsilon_{lk} i_l \right] - (\mu + \gamma) i_k$$

where the coupling matrix ϵ_{lk} has the form

$$\epsilon_{lk} = \frac{N_l}{N_k} \tag{4.27}$$

with the interesting property

$$\epsilon_{kl} = \frac{1}{\epsilon_{lk}}. \tag{4.28}$$

The distribution $\tilde{\rho}(\epsilon_{lk})$ of the elements of the coupling matrix can be computed from the distribution $\rho(N_i)$ of the city sizes using the Frobenius-Peron equation. We plot in Figure 4.17 the distribution $\tilde{\rho}(\epsilon_{lk})$ when $\rho(N_i)$ is a power-law and a uniform distribution.

The computations for a power-law distribution

$$\rho(N_i) = \left(\frac{\alpha - 1}{N_0} \right) \left(\frac{N_i}{N_0} \right)^{-\alpha} \quad \text{with } N_i \geq N_0 \tag{4.29}$$

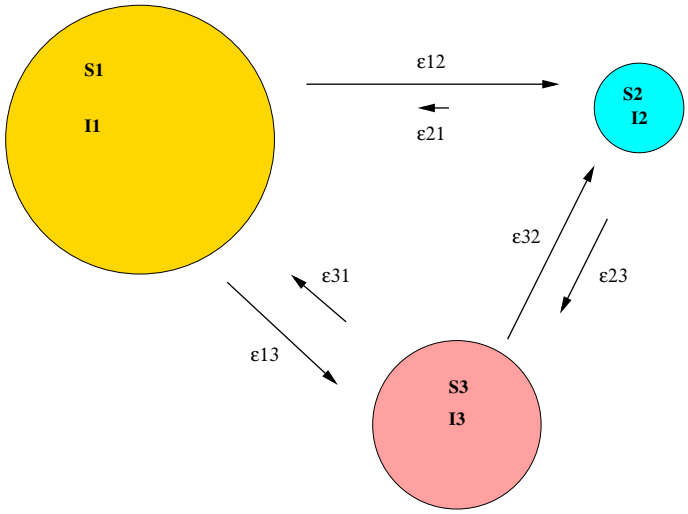

Figure 4.16: Schematic representation of a network of 3 coupled cities. Notice the highly asymmetric coupling strength ϵ_{ij}, where $\epsilon_{ji} = 1/\epsilon_{ij}$.

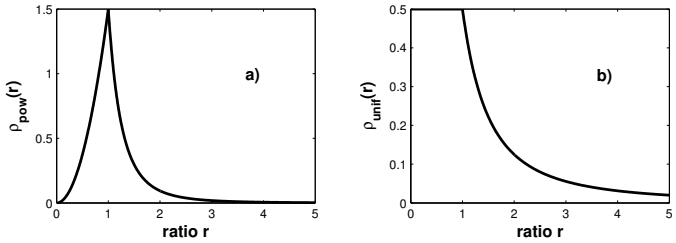

Figure 4.17: Ratio distribution $\tilde{\rho}(r = N_l/N_k)$ for a) the the power-law ($\alpha = 4$) and b) the uniform distribution.

lead to

$$\tilde{\rho}(\epsilon_{lk}) = \begin{cases} \frac{1}{2}(\alpha - 1)r^{-\alpha} & \text{if } r \geq 1 \\ \frac{1}{2}(\alpha - 1)r^{\alpha-2} & \text{if } r < 1 \end{cases} \tag{4.30}$$

and for a uniform distribution

$$\rho(N_i) = \begin{cases} 1 & , \text{ if } N_i \in [0,1] \\ 0 & , \text{ otherwise} \end{cases} \tag{4.31}$$

the result is

$$\tilde{\rho}(\epsilon_{lk}) = \begin{cases} \frac{1}{2} & , \quad r < 1 \\ \frac{1}{2r^2} & , \quad r \geq 1 \end{cases} \tag{4.32}$$

Concerning real cities, the sizes are distributed following Zipf's law [25]. This law yields a power-law distribution, where there exist a lot of small cities and only a few large cities.

4.7 Dynamics in the network

We show in this section numerical simulations of the system (4.27) and describe the different dynamical regimes which can be observed. In a first time we consider an ensemble of 60 cities which have the size distribution of the real cities in the data from England/Whales. We examine the behavior of the system (4.27) by considering the mean-field

$$G_n =< S_n^i >_i = \frac{1}{N} \sum_i S_n^i \tag{4.33}$$

of the symbolic sequences for each city as a measure for the global dynamics.

Let us consider the dynamics in the network in the case of weak, intermediate and strong coupling strength w:

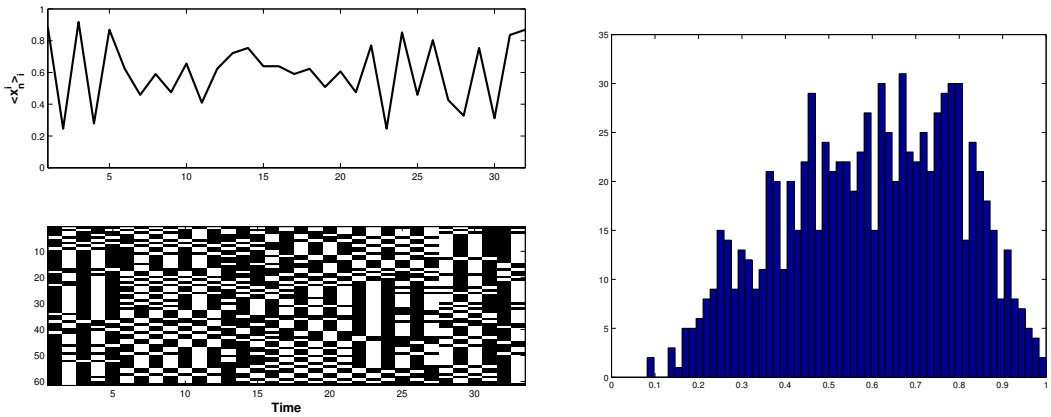

(a) (b)

Figure 4.18: real city sizes. incoherent state.

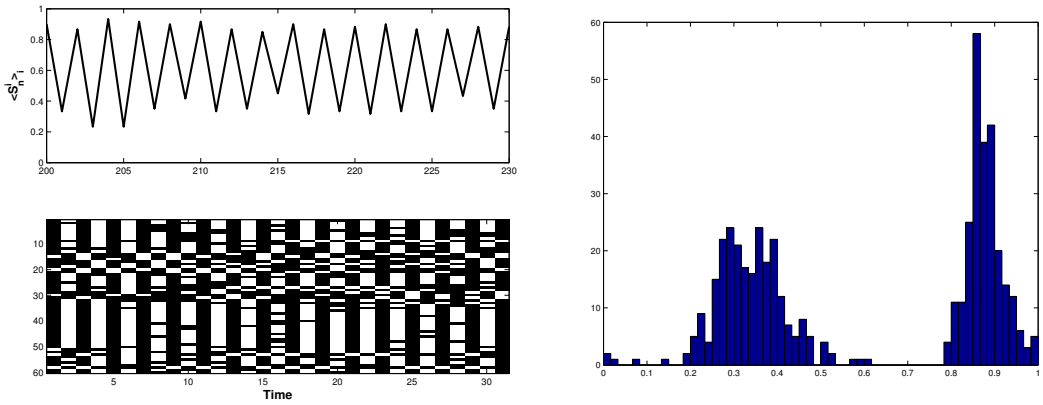

(a) (b)

Figure 4.19: real city sizes. pseudo-limit cycle state.

- In order to show the effect of weak coupling ($w \approx 0.0001$) on the global dynamics we show in Figure 4.18a and 4.18b the time series of the mean-field G_n and its histogram, respectively. No coherent structure is observed and the dynamics can be represented by a Gaussian distribution.

- Figure 4.19 shows the consequences of intermediate coupling ($w \approx 0.001$) on the dynamics of the mean-field G_n. We observe the apparition of a global quasi-limit cycle and the histogram of the mean-field can be represented by a bi-modal Gaussian distribution.

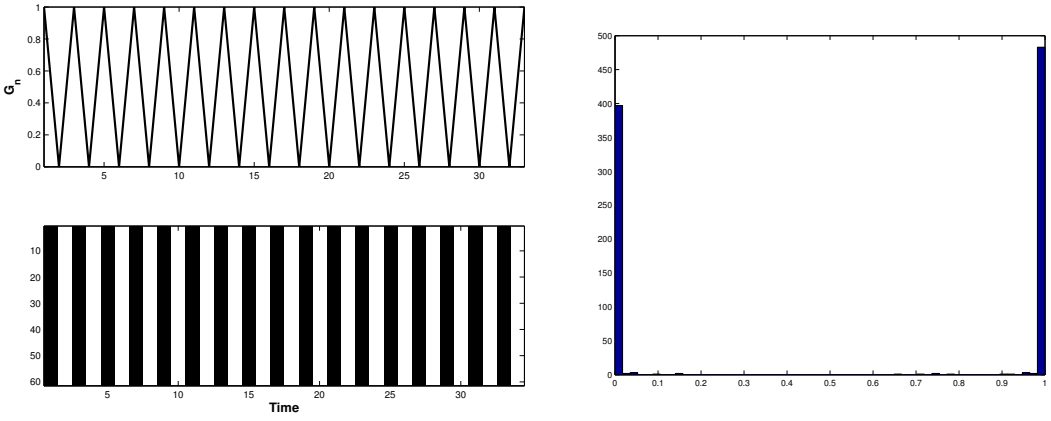

(a) (b)

Figure 4.20: real city sizes. pseudo-limit cycle state.

- As expected for strong coupling ($w \approx 0.01$), the system (4.27) leaves the chaotic regime and goes into a limit cycle. The resulting bi-annual limit cycle is shown in Figure 4.20a and the density distribution of the mean-field becomes a double δ-function (see Figure 4.20b).

We observed that the dynamics in the network can only be in these three different regimes which correspond to three different domains of the coupling strength. We also performed the simulations for other form of distributions $\rho(n)$ of the city sizes. The results are quasi-identical for the power-law distribution. This is obvious because the sizes of the real cities are also power-law distributed. There are small variations in the observations for the uniform distribution. It seems that the range of the coupling strength where the system is an the quasi-limit cycle regime is slightly smaller than in the case of the power-law distribution.

4.8 Conclusion

In this chapter we considered an ensemble of N coupled SIR-model, each representing the dynamics of an infectious disease in a city. The coupling between the systems was introduced through the sizes of the cities and is proportional to $\epsilon_{ij} = n_j/n_i$. The elements of the coupling matrix ϵ_{ij} are generated by the size distribution $\rho(n)$. The coupling matrix fulfill the property $\epsilon_{ji} = 1/\epsilon_{ij}$, which means that the coupling direction is strongly depended on the size ratio. If the sizes n_i and n_j are comparable, each system influences the other one in a similar way. In contrary, if the size n_i is more than two or three time larger than the size n_j, the system i will influence the system j ($i \rightarrow j$) but not the

opposite ($j \nrightarrow i$).

In order to analyze in a more convenient way the dynamics of the system, we introduced we concept of symbolic dynamics. The SIR-model shows a typical dynamics of recurrent outbreaks where each year it occurs or not each an outbreak of a disease. The occurrence of an outbreak is coded with the symbol '1' and the non-occurrence (skip) with '0'. The dynamics of a system is then represented by a sequence of symbols which permits us to examine properties of the system like synchronization.

We made an exhaustive study of the simple case of two coupled SIR-models. We find that only three regimes can take place: either the systems are synchronized, anti-synchronized or not synchronized (independent dynamics). These different regimes correspond to strong, intermediate, weak coupling, respectively. In the case where the ratio n_2/n_1 is larger than 3, the anti-synchronized regime does not appear anymore. We studied the system of two coupled Rößler oscillators and find out that exactly the same regimes and transitions are observed (see Appendix A).

In the case of N coupled systems, we also observe three possible regimes. Small coupling leads to a global dynamics which has not particularities and is represented by a Gaussian distribution. The dynamics in the case of intermediate coupling is described by a bi-modal Gaussian distribution. This corresponds to a global dynamics which shows a quasi-limit cycle behavior. For strong coupling the system is not anymore chaotic and falls into a bi-annual limit cycle. We performed simulations where the sizes n_i where uniform and power-law distributed and find that the transitions between these different regimes occur in both cases.

The global quasi-limit cycle we observed in the case of intermediate coupling corresponds very well to the bi-annual recurrence of outbreaks in the measles data from England/Wales. During these outbreaks, nearly all cities are synchronized. We could reconstruct the susceptibles from data and the result leads to us to attractors which were very similar to the 'tooth attractor' of the SIR-model.

Appendix A: Extension to coupled Rössler oscillators

We study here the interaction of two coupled Rössler oscillators coupled in the z-variable

$$\begin{cases} \dot{x_1} = -y_1 - z_1 \\ \dot{y_1} = x_1 + a y_1 \\ \dot{z_1} = b + z_1(x_1 - c) + w(z_2 - z_1) \end{cases} \tag{4.34}$$

$$\begin{cases} \dot{x_2} = -y_2 - z_2 \\ \dot{y_2} = x_2 + a y_2 \\ \dot{z_2} = b + z_2(x_2 - c) - w(z_2 - z_1) \end{cases} \tag{4.35}$$

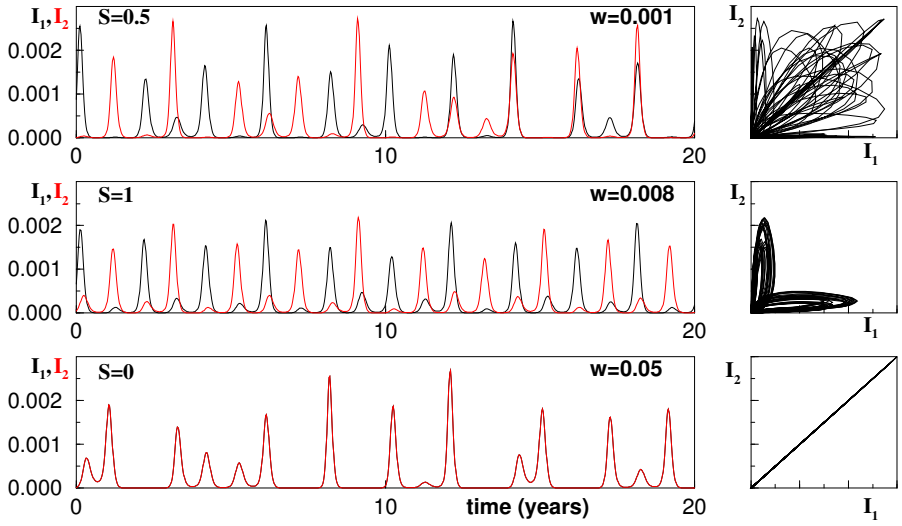

Figure 4.21: Interaction of two coupled Rössler oscillators. Left colum: Variable z_1 *vs.* variable z_2. Right colum: time series of z_1 and z_2. The coupling strength is a) $w = 0.001$, b) $w = 0.008$ and c) $w = 0.05$ and the parameters are $a = b = 0.2$ and $c = 5$.

where w is the coupling strength. The numerical values of the parameters are $a = 0.2$, $b = 0.2$ and $c = 5$.

We observe in Figure 4.21 that three dynamical regimes are possible: either the systems synchronize, anti-synchronize or do not synchronize at all. These regimes are observed for strong, intermediate and small coupling strength w, respectively. This system shows exactly the same dynamical behavior than two coupled SIR-models (see Figure 4.12).

Chapter 5

Complex Dynamics in Networks with distributed Sizes

5.1 Motivation

Since natural interacting systems often show large differences in their sizes, we generalize in this chapter the problem of infectious diseases in networks of cities to the study of networks of weighted chaotic maps. These weights can be distributed over several order of magnitudes. In the framework of epidemiological SIR-model, the coupling is introduced through the ratio of city sizes.

A network is an abstract set of k nodes connected by l links. The nodes represents in our case dynamical systems but they could also be individuals, computers or Internet pages in the WWW. A link between two nodes can be either directed, weighted or both. This means that the a node can influence another node without being itself influenced or that the intensity of the influence can vary. The network is mathematically represented by the so-called adjacency matrix $A(n, m)$, where each element is the intensity of the connection *from* node n *to* node m. Networks are described using graph theory and statistical properties like degree distribution, connectivity, clustering coefficient or mean path-length can be computed [105].

The topic of coupled logistic maps has been well studied for special types of networks. For example the case of global coupling has been considered by [114, 116, 119, 123, 121] and the case of scale-free networks by [104]. Their findings help to understand the different regimes or states which can occur in these networks [119, 114] and the statistical properties of the global dynamics [123].

The novelty of our approach lies in the new type of coupling which is directly derived from the coupling $\epsilon_{ij} = n_j/n_i$ used in the system of differential equations (4.26). The topology of the network is entirely generated by a single parameter and by the size

distribution of the system. This additional parameter can be interpreted as an effective temperature T_{eff} and a large variety of network configurations can be created. The topologies which are generated differ from the classical ones [105] (power-law, Poisson, small-world, random...).

We classify in a first part the different topologies which can be generated by the size distribution and the effective temperature. The second part is then devoted to the study of the global dynamics corresponding to these different networks. In the last part we finally design an effective theory which permits to understand the dynamics in this complex system.

5.2 Coupling N maps in a weighted network

We consider in this section a set of N coupled maps in a weighted network. The dynamics is described by

$$x^i_{n+1} = (1 - \frac{\epsilon}{N}\sum_{j=1}^{N} g_{ij}) f(x^i_n) + \frac{\epsilon}{N}\sum_{j=1}^{N} g_{ij} f(x^j_n) \tag{5.1}$$

where $f(x)$ represents the map, ϵ the coupling strength and g_{ij} the coupling matrix which is a function of the sizes n_i and n_j of two systems i and j. The sizes are distributed as $\rho(n)$.

The coupling function was $\epsilon_{ij} = n_j/n_i$ in the case of coupled SIR-models. This form cannot be directly transposed to coupled maps because the coupling intensity has to stay in the interval $[0, 1]$ to insure the stability of the system. Therefore one has to find a transformation of the type

$$\epsilon_{ij} \in [0, +\infty] \overset{\mathcal{T}?}{\longmapsto} g_{ij} \in [0, 1] \tag{5.2}$$

The property (4.28)

$$\epsilon_{ji} = 1/\epsilon_{ij} \tag{5.3}$$

obliges the transformation $\mathcal{T}$ to fulfill the condition

$$g_{ji} = 1 - g_{ij}. \tag{5.4}$$

A possible solution for the coupling is the saturating function

$$g_{ij} = \frac{1}{2}\left(1 + \tanh\left(\mu \ln\left(\frac{n_j}{\kappa n_i}\right)\right)\right) = \frac{1}{1 + (n_j/\kappa n_i)^{-2\mu}} \tag{5.5}$$

which is plotted in fig. (5.1) where $g_{ij} = g(r)$, with $r = n_j/n_i$.

The parameter μ can be interpreted as an effective temperature with $T_{eff} \sim 1/\mu$. The limiting case $\mu \to 0$ corresponds to the situation where all coupling strengths are equal

and the structure of the network is destroyed by the high temperature (global coupling). The other limiting case $\mu \to \infty$ represents a network which is frozen ($T_{eff} \to 0$) in a hierarchical way. The links are uni-directional and only systems having a size n_j larger than κn_i contribute to the dynamics of system i. The parameter κ represents some threshold defining the critical ratio r_c above which a system j influences a system i in the case $\mu \to \infty$. Thus, the parameter μ allows to smoothly deform the network from a global coupling to a directed network.

The form (5.5) of the coupling offers the possibility to generate various configurations of networks. The structure of the network depends solely on the size distribution $\rho(n)$ and the parameters μ and κ. In the following the network topology is analyzed in function of these parameters.

5.3 Analysis of the network topology

This section is devoted to the relation between the coupling matrix (5.5) and the network topology. A systematical analysis of the network characteristics in function of the parameters μ and κ and the size distribution $\rho(n)$ is performed. Since a large number of different topologies can arise from the coupling function (5.5), we split for clarity of the study by considering the two cases where $\mu \to \infty$ μ takes intermediate values ($\sim \kappa$). This is the first step in order to later understand the relation between the topology of the network and its dynamics.

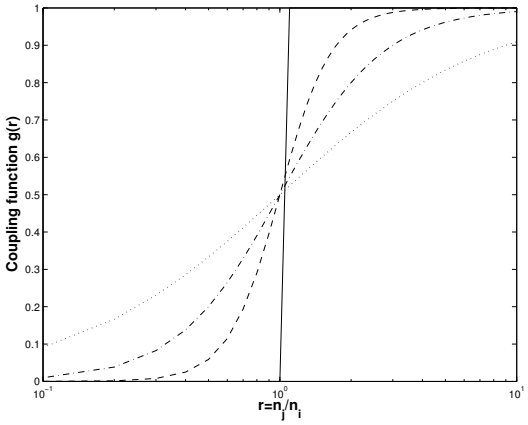

Figure 5.1: Plot of the coupling function (5.5) for $\mu = 0.5$ (dotted line), $\mu = 1$ (dash-dot line), $\mu = 2$ (dashed line) and $\mu \to \infty$ (solid line). $\kappa = 1$ in all cases and the variable $r = n_j/n_i$ is plotted on a logarithmic scale.

5.3.1 The case $\mu \to \infty$: hierarchical topology

When $\mu \to \infty$, the effective temperature $T_{eff} \to 0$ and the coupling tends to the Heaviside function

$$g_{ij} \to \theta\left(\frac{n_j}{n_i} - \kappa\right) \tag{5.6}$$

This corresponds to a situation where the network is frozen in a hierarchical topology (see for example [127]). A system j only contributes to a system i if the ratio n_j/n_i is larger than κ, that means if $n_j \geq \kappa n_i$. The links are then directed and not weighted.

Given the distribution $\rho(n)$ and the parameter κ, it is possible to compute some typical statistical properties of the network: degree distribution, distribution of the ratio $r = n_j/n_i$, connectivity and clustering coefficient.

We consider for the distribution function $\rho(n_i)$ the following very common cases: a) power-law, b) uniform and c) exponential distributions.

a) The power-law distribution

$$\rho(n_i) = \left(\frac{\alpha - 1}{n_0}\right)\left(\frac{n_i}{n_0}\right)^{-\alpha} \quad \text{with } n_i \geq n_0 \tag{5.7}$$

Depending of the parameter κ, three types of topologies are generated (see fig. (5.5)):

$\kappa < 1$: The network is over-linked, which means that there can be two links (bi-directionality) between two nodes. There are $m = (1 - \kappa^{\alpha-1})N$ nodes which are globally connected. Each node has a minimal number of links $k_{min} = 0$ and the maximal number is $k_{max} = N - 1$.

$\kappa = 1$: A node with index i in the ranking of sizes has ingoing links only from nodes j which are larger. That means with $j > i$ and there is exactly one link between two nodes. The minimal and maximal connectivity is $k_{min} = 0$ and $k_{max} = N - 1$, respectively.

$\kappa > 1$: Each node has a maximal number of links $k_{max} = (N-1)\kappa^{-\alpha+1}$. and the minimal connectivity is $k_{min} = 0$. The network is weakly linked.

In order to compute the degree distribution of the network, we first need to compute the number of links (connectivity) going *into* a node i

$$\begin{aligned} k_i(n_i) &= (N-1)P(n_j \geq \kappa n_i) \\ &= (N-1)\int_{\kappa n_i}^{+\infty} \rho(n_j)dn_j \\ &= (N-1)\left(\frac{\kappa n_i}{n_0}\right)^{-\alpha+1} \end{aligned} \tag{5.8}$$

We obtain for the degree distribution

$$\begin{aligned}\bar{\rho}(k) &= \int \delta[k-k_i(n_i)]\rho(n_i)dn_i \\ &= \begin{cases} \frac{\kappa^{\alpha-1}}{N-1}+(1-\kappa^{\alpha-1})\delta(k-k_{max}) & \text{if } \kappa<1 \quad , \quad 0\le k\le N-1 \\ \frac{\kappa^{\alpha-1}}{N-1} & \text{if } \kappa\ge 1 \quad , \quad 0\le k\le (N-1)\kappa^{-\alpha+1} \end{cases}\end{aligned} \tag{5.9}$$

and the mean connectivity becomes

$$< k >= \int k\bar{\rho}(k)dk = \begin{cases} (N-1)(1-\frac{\kappa^{\alpha-1}}{2}) & , \quad \kappa<1 \\ \frac{N-1}{2}\kappa^{-\alpha+1} & , \quad \kappa\ge 1 \end{cases} \tag{5.10}$$

The clustering coefficient for node i is defined as

$$C_i = \frac{E_i}{k_i(k_i-1)} \tag{5.11}$$

where k_i is the number of links going *into* this node, $k_i(k_i-1)$ the maximum number of links between the k_i nodes and E_i the real number of links between the k_i nodes (in the case of an *undirected* network, the clustering coefficient C_i must be multiplied by 2). The clustering coefficient can be computed out of the distribution $\tilde{\rho}(r)$ of the ratio $r=\frac{n_p}{n_q}$. Therefore we first use the joint probability density for systems having their size larger than a with size $n_{p,q}\ge\kappa n_i$

$$\rho(n_p,n_q) = \left(\frac{\alpha-1}{\kappa n_i}\right)^2\left(\frac{n_p}{\kappa n_i}\right)^{-\alpha}\left(\frac{n_q}{\kappa n_i}\right)^{-\alpha} \tag{5.12}$$

The ratio distribution is computed from the formula

$$\begin{aligned}\rho_{n_i}(r) &= \int_{\kappa n_i}^{\infty} n_p\rho(n_p,rn_p)dn_p \\ &= \begin{cases} \frac{1}{2}(\alpha-1)r^{-\alpha} & \text{if } r\ge 1 \\ \frac{1}{2}(\alpha-1)r^{\alpha-2} & \text{if } r<1 \end{cases}\end{aligned} \tag{5.13}$$

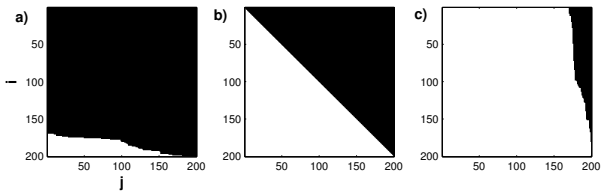

Figure 5.2: Representation of the coupling matrix (5.6) in the case where $\mu\to\infty$ and $\rho(n_i)$ is a power-law distribution ($\alpha=4$). The parameters are a) $\kappa=0.5$, b) $\kappa=1$ and c) $\kappa=2$ ($N=200$ in all cases).

and the number of uni-directional links between all the pairs of nodes p and q having their size larger than κn_i is

$$\begin{aligned} E_i &= k_i(k_i-1)P(r \geq \kappa) \\ &= k_i(k_i-1)\int_{\kappa}^{\infty} \rho_{n_i}(r)dr \\ &= k_i(k_i-1)\begin{cases} \frac{1}{2}\kappa^{-\alpha+1} & , \quad \kappa \geq 1 \\ 1-\frac{1}{2}\kappa^{\alpha-1} & , \quad \kappa < 1 \end{cases} \end{aligned} \tag{5.14}$$

This leads to the clustering coefficient for node i

$$C_i = \begin{cases} \frac{1}{2}\kappa^{-\alpha+1} & , \quad \kappa \geq 1 \\ 1-\frac{1}{2}\kappa^{\alpha-1} & , \quad \kappa < 1 \end{cases} \tag{5.15}$$

which can be averaged over all possible sizes n_i

$$\begin{aligned} C &= < C_i > \\ &= \int_{n_i}^{\infty} C_i \rho(n_i) dn_i \\ &= \begin{cases} \frac{1}{2}\kappa^{-\alpha+1} & , \quad \kappa \geq 1 \\ 1-\frac{1}{2}\kappa^{\alpha-1} & , \quad \kappa < 1 \end{cases} \end{aligned} \tag{5.16}$$

We observe on fig. (5.3.a) that the clustering coefficient (5.16) is large for small values of κ and drops rapidly to zero after the $\kappa = 1$. There are less links when κ grows and the nodes are more independent from each another.

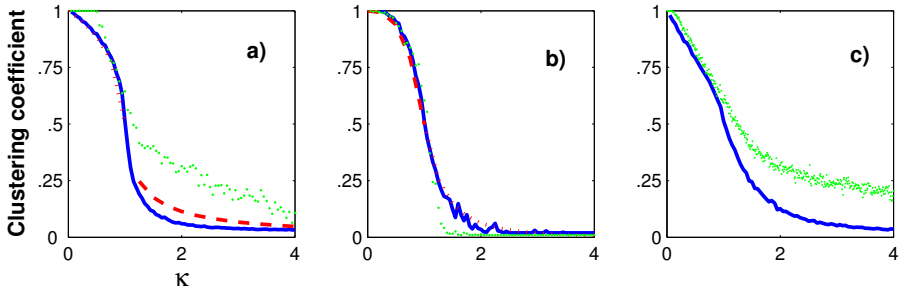

Figure 5.3: Clustering coefficient for the a) uniform, b) power-law ($\alpha = 4$) and c) exponential ($\beta = 1$) distribution with $N = 100$ and $\mu \to \infty$. Plotted are the numerical (solid blue line) *vs.* the analytical results (dashed red line). The dotted green line corresponds to the size of the cluster of synchronized maps which is determined numerically in the section 6.5 following formula 5.34.

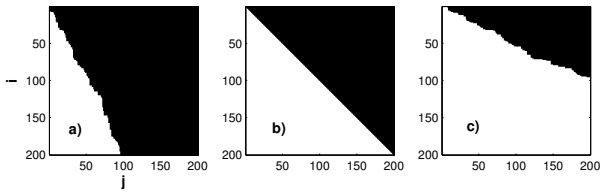

Figure 5.4: Representation of the coupling matrix (5.6) in the case where $\mu \to \infty$ and $\rho(n_i)$ is a uniform distribution. The parameters are a) $\kappa = 0.5$, b) $\kappa = 1$ and c) $\kappa = 2$ ($N = 200$ in all cases).

b) The uniform distribution

$$\rho(n_i) = \left\{ \begin{array}{lcl} 1 & , & \text{if } n_i \in [0,1] \\ 0 & , & \text{otherwise} \end{array} \right. \qquad \left(\text{ or } \left\{ \begin{array}{lcl} \frac{1}{n_2 - n_1} & , & \text{if } n_i \in [n_1, n_2] \\ 0 & , & \text{otherwise} \end{array} \right. \right) \tag{5.17}$$

Depending of the parameter κ, three types of topologies are generated (see fig. (5.5)):

$\kappa < 1$: Each node has a minimal number *ingoing* of links $k_{min} = k_{max}(1 - \kappa)$, where the maximal number is $k_{max} = N - 1$. The network is over-linked, which means that there can be two links (bi-directionality) between two nodes.

$\kappa = 1$: A node with index i in the ranking of sizes has ingoing links only from nodes j which are larger, that means with $j > i$, and there is exactly one link between two nodes. The minimal and maximal connectivity is $k_{min} = 0$ and $k_{max} = N - 1$, respectively.

$\kappa > 1$: Not all nodes are connected in this topology. There are $m = (1 - \frac{1}{\kappa})N$ nodes which are completely unconnected. The minimal and maximal connectivity is $k_{min} = 0$ and $k_{max} = N - 1$, respectively.

We perform identical computations than for the power-law distribution. This leads to the following results for the connectivity

$$k_i(n_i) = (N-1)(1 - \kappa n_i), \tag{5.18}$$

the degree distribution

$$\tilde{\rho}(k) = \left\{ \begin{array}{ll} \frac{1}{(N-1)\kappa} & \text{if } \kappa < 1 \quad , \quad (N-1)(1-\kappa) \le k \le N-1 \\ \frac{1}{(N-1)\kappa} + \left(\frac{\kappa - 1}{\kappa}\right) \delta(k) & \text{if } \kappa \ge 1 \quad , \quad 0 \le k \le N-1, \end{array} \right. \tag{5.19}$$

the mean connectivity

$$< k >= \left\{ \begin{array}{lcl} (N-1)(1 - \frac{\kappa}{2}) & , & \kappa < 1 \\ \frac{N-1}{2\kappa} & , & \kappa \ge 1 \end{array} \right. \tag{5.20}$$

the ratio distribution function

$$\rho_{n_i}(r) = \left\{ \begin{array}{lcl} \frac{n_2^2 - (\kappa n_i / r)^2}{2(n_2 - \kappa n_i)^2} & , & \frac{\kappa n_i}{n_2} \le r < 1 \\ \frac{(n_2/r)^2 - (\kappa n_i)^2}{2(n_2 - \kappa n_i)^2} & , & 1 \le r \le \frac{n_2}{\kappa n_i} \end{array} \right. , \tag{5.21}$$

and the clustering coefficient

$$C = \begin{cases} \frac{3\kappa-2}{2\kappa} + \frac{\kappa-1}{\kappa^2}\log|1-\kappa| & , \quad \kappa < 1 \\ \frac{2\kappa-1}{2} + \kappa(\kappa-1)\log\left|\frac{1-\kappa}{\kappa}\right| & , \quad \kappa \geq 1 \end{cases} \tag{5.22}$$

for $n_1 = 0$ and $n_2 = 1$.

We see from fig. (5.3.b) that the clustering coefficient for the uniform distribution has qualitatively the same features than for the power-law distribution. The larger κ is, the smaller the number of connected nodes is.

c) The exponential distribution

$$\rho(n_i) = \beta e^{-\beta n_i} \quad \text{with } n_i \geq 0 \tag{5.23}$$

Respectively, the minimal and maximal connectivity is $k_{min} = 0$ and $k_{max} = N - 1$ for all κ's. But depending on the parameter κ, three types of topologies are generated (see fig. (5.5)):

$\kappa < 1$: Some pairs of nodes have bidirectional links and the network is over-linked.

$\kappa = 1$: A node with index i in the ranking of sizes has ingoing links only from nodes j which are larger, that means with $j > i$, and there is exactly one link between two nodes.

$\kappa > 1$: Some pairs of nodes are not connected in this configuration and the network is under-linked.

We perform identical computations than for the power-law distribution. This leads to the following results for the connectivity

$$k_i(n_i) = (N-1)e^{-\beta n_i}, \tag{5.24}$$

the degree distribution

$$\tilde{\rho}(k) = \left(\frac{1}{\kappa k}\right)\left(\frac{k}{N-1}\right)^{1/\kappa} \tag{5.25}$$

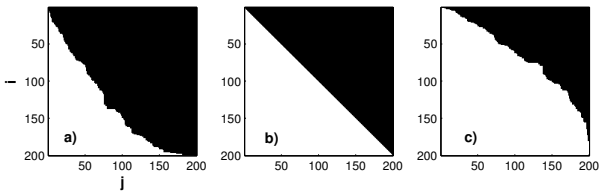

Figure 5.5: Representation of the coupling matrix (5.6) in the case where $\mu \to \infty$ and $\rho(n_i)$ is an exponential distribution ($\beta = 1$). The parameters are a) $\kappa = 0.5$, b) $\kappa = 1$ and c) $\kappa = 2$ ($N = 200$ in all cases).

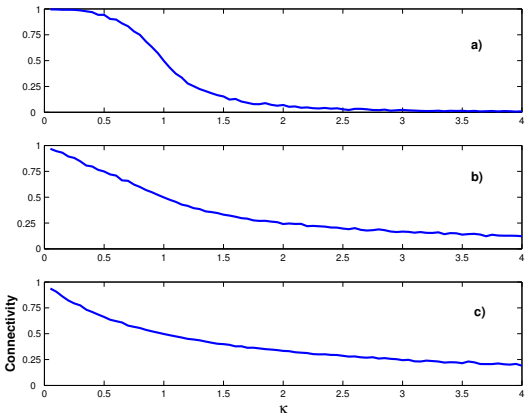

Figure 5.6: Plot of the mean connectivity in function of κ when $\mu \to \infty$. In the case of a) the power-law ($\alpha = 4$), b) the uniform and c) the exponential ($\beta = 1$) distribution ($N = 200$).

and the mean connectivity

$$< k >= \frac{N-1}{1+\kappa} \tag{5.26}$$

The ratio distribution $\rho_{n_i}(r)$, and so the clustering coefficient, cannot be computed analytically because integrals of the type

$$\int \frac{e^{-\beta n_i}}{1+n_i} dn_i \tag{5.27}$$

are appearing. But the clustering coefficient can be computed numerically (see fig. (5.3.c)).

It clearly appears from this analysis that the role played by the exact form of size distribution $\rho(n)$ is minimal in the case $\mu \to \infty$. We see that the clustering coefficient C (cf. fig (5.3)) and the mean connectivity $< k >$ (cf. fig (5.6)) have very similar shape. In contrast, the parameter κ controls directly all the essentials statistical properties of the network. This information will be very useful when developing in the next sections an effective theory for the global system.

5.3.2 Intermediate values of μ: weighted links

In this section we characterize the properties of the network when links are weighted, that means in the case were μ does not $\to 0$ or ∞. This topic has been partly studied by [106, 119] when the weights are evolving in time.

Intuitively, during the transition $\mu : \infty \to 0$, the pairs of systems having their ratio near κ are influenced first. We mainly characterize the network by considering the distribution

$\chi(g)$ of the coupling strength

$$g_{ij} = g(r) = \frac{1}{1 + (r/\kappa)^{-2\mu}} \tag{5.28}$$

if $r = n_j/n_i$ is a stochastic variable with distribution $\tilde{\rho}(r)$. $\chi(g)$ gives the number of systems having in- or out-going links with coupling strength g.

To compute $\chi(g)$ we use the Frobenius-Perron equation

$$\chi(g) = \int_0^\infty \delta[g - g(r)]\tilde{\rho}(r)dr \tag{5.29}$$

Using the distributions (5.16) and (5.22) for the power-law and uniform distributions, respectively, we find that

$$\chi^{power}(g) = \begin{cases} \left(\frac{\alpha-1}{4\mu g^2}\right)\kappa^{\alpha-1}\left(\frac{1}{g}-1\right)^{-1-\frac{\alpha-1}{2\mu}} & , \quad g < \frac{1}{2} \\ \left(\frac{\alpha-1}{4\mu g^2}\right)\kappa^{-\alpha+1}\left(\frac{1}{g}-1\right)^{-1+\frac{\alpha-1}{2\mu}} & , \quad g \geq \frac{1}{2} \end{cases} \tag{5.30}$$

$$\chi^{unif}(g) = \begin{cases} \left(\frac{\kappa}{4\mu g^2}\right)\left(\frac{1}{g}-1\right)^{-1-\frac{1}{2\mu}} & , \quad g < \frac{1}{2} \\ \left(\frac{1}{4\mu g^2\kappa}\right)\left(\frac{1}{g}-1\right)^{-1+\frac{1}{2\mu}} & , \quad g \geq \frac{1}{2} \end{cases} \tag{5.31}$$

In the case of the exponential distribution, $\chi(g)$ cannot be computed because there is no analytical form for $\tilde{\rho}(r)$.

Fig. (5.7) and (5.8) shows a 3-dimensional plot of $\chi^{unif}(g)$ and $\chi^{power}(g)$. We see that both distributions are centered in peak around $g = 0.5$ for small μ ($T_{eff} \to \infty$, high

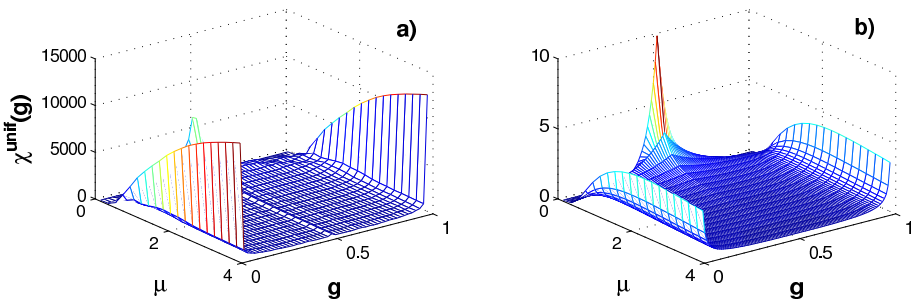

Figure 5.7: Graphical representation of the density $\chi^{unif}(g)$ in function of μ and g. a) Numerical ($N = 200$) and b) analytical (see formula (5.31)) computation for $\rho(n)$ a uniform distribution and $\kappa = 1$.

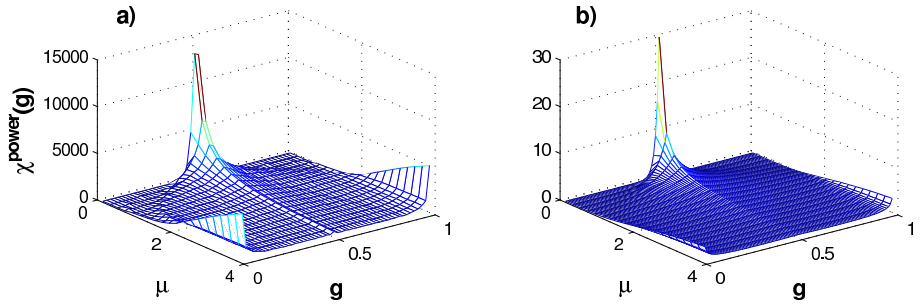

Figure 5.8: Graphical representation of the density $\chi^{power}(g)$ in function of μ and g. a) Numerical ($N = 200$) and b) analytical (see formula (5.30)) computation for $\rho(n)$ a power-law distribution ($\alpha = 4$) and $\kappa = 1$.

temperature). That means that most of links have the strength $g_{ij} = 0.5$. For large μ ($T_{eff} \to 0$, low temperature), the distributions are maximum when $g = 0$ and $g = 1$ and the coupling strength can take only two values: 0 or 1.

Intermediate values of μ correspond to a situation where the couplings strength is peaked at the three positions $g = 0$, $g = 0.5$ and $g = 1$. This is shown in fig. (5.9). That means that almost only links having these three coupling strengths are present in the network. N^H nodes of the network are coupled in a hierarchical way and N^G nodes are globally coupled. The fraction N^H/N^G grows with μ. To conclude this section we notice that the exact form of the size distribution $\rho(n)$ does not play a major role in the topology of the network.

Intermediate values of μ correspond to a situation where the couplings strength is peaked at the three positions $g = 0$, $g = 0.5$ and $g = 1$. This is shown in fig. (5.9). That means that almost only links having these three coupling strengths are present in the network. N^H nodes of the network are coupled in a hierarchical way and N^G nodes are globally coupled. The fraction N^H/N^G grows with μ. To conclude this section we notice that the exact form of the size distribution $\rho(n)$ does not play a major role in the topology of the network.

5.4 Networks of asymmetrical tent maps

In a first time we stay close to the epidemiological concepts of the previous chapter and consider a system of coupled asymmetric tent maps. After that we expand the study to networks of logistic maps.

We couple N asymmetric tent maps using the coupling function (5.5). The map $f(x)$

then reads

$$f(x) = \begin{cases} qx & \text{for } x < 0 \quad (q = 0.8) \\ -rx & \text{for } x \geq 0 \quad (r = 2) \end{cases} \tag{5.32}$$

which is the form of the map 4.16 derived from the SIR-model. We present in Figure 5.10 and 5.11 some typical numerical results for the simulation of system (5.1). The transition of the global dynamics when the parameters μ varies from 0 to 100 can be clearly observed. All the maps are independent when μ is small and no structure is recognizable. When μ is large, a dynamics where most of the maps are in a quasi-period-2 regime occurs.

The symbolic dynamics S_n^i is simply generated by considering the sign of x_n^i, $S_n^i = \Theta(x_n^i)$. If x_n^i is positive, $S_n^i = 1$ and if x_n^i is negative, $S_n^i = 0$. In order to understand the effect of this reduction we compare the histograms of the mean-fields $< x_n^i >_i$ and $< S_n^i >_i$ in Figure 5.11. It appears that both dynamics are quasi identical and that the symbolic dynamics can be used without risk of information loss. It seems that the configuration of the network in the case $\mu \to \infty$ tends to stabilize the period-2 limit cycle regime, even if the individual maps remains chaotic.

Figure 5.12 gives information about the transition from incoherent dynamics to global limit cycle. The maps with a small weight have a higher transition probability for a period-2 limit cycle ($p(0|1)$ grows and $p(1|1)$ diminishes) than the systems with a larger weights. We also observe that the synchrony between maps grows with the hierarchical level of the network. This synchronization prenomen has been described by authors working on mast seeding [23, 111, 112], on spatial predator/prey systems [32] or on abstract systems of coupled maps [104, 108, 110].

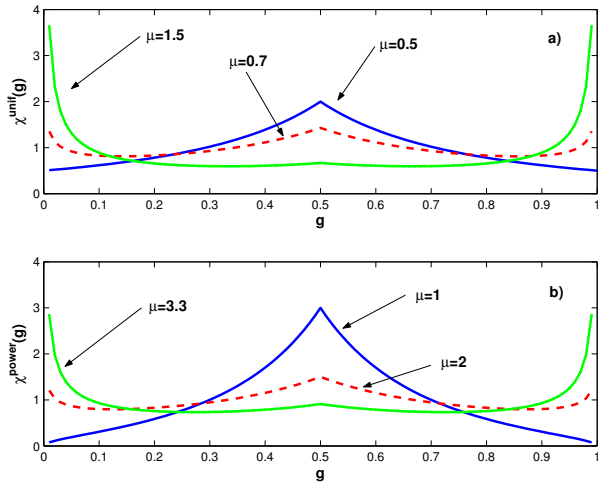

Figure 5.9: Graphical representation of the densities a) $\chi^{unif}(g)$ and b) $\chi^{power}(g)$ for $\kappa = 1$.

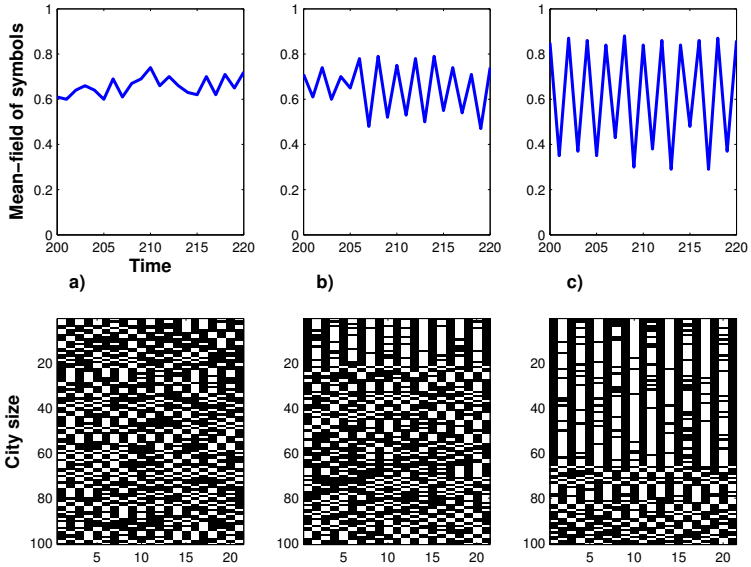

Figure 5.10: Numerical results for an ensemble of 100 coupled tent maps (5.32). In the upper part is plotted the mean-field of the symbols and in the lower part is plotted the symbolic sequence for each system (black corresponds to a '1' and white to a '0'). The parameters are $\kappa = 1$, $\epsilon = 0.2$ and a) $\mu = 0$ (global coupling), b) $\mu = 0.5$, c) $\mu = 10$ (hierarchical network). The n_i's are uniformly distributed.

5.5 Generalization to the logistic maps

We consider here the general model (5.1) of coupled maps where $f(x) = rx(1-x)$ is the logistic map in the chaotic regime ($r = 4$) and the coupling matrix g_{ij} has the form (5.5) derived at the begin of the chapter. Each individual map is characterized by a size n_i.

The system (5.1) has been studied in the case of the following classical topologies: global coupling [119, 123, 121], scale-free networks [104, 105] or small-world networks [110, 108]. We introduce with the coupling matrix g_{ij} a new network topology.

We first consider the simple case $\mu \to 0$, which corresponds to a situation where the effective temperature $T_{eff} \to \infty$. In this case the high temperature destructs the structure of the network and the coupling strength is identical for all pairs of systems

$$g_{ij} \to \frac{1}{2} \tag{5.33}$$

The topology corresponds to an all-to-all coupling with only free parameter the coupling strength ϵ. This situation has been extensively been studied in [114, 115, 116, 121, 122, 123]. It was found that the dynamics dynamics appearing in this system was very rich:

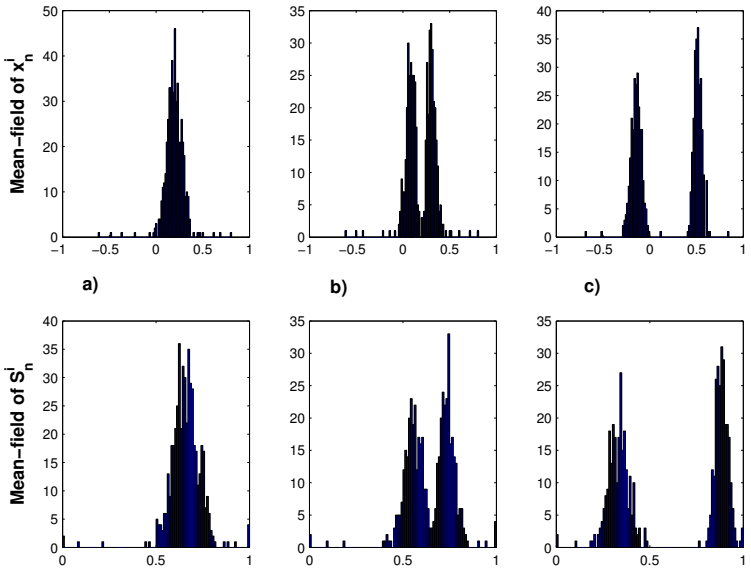

Figure 5.11: Distributions of the mean-field of the real variables $< x_n^i >_i$ and the symbolic variables $< S_n^i >_i$. The parameters are $\kappa = 1$, $\epsilon = 0.2$ and a) $\mu = 0$, b) $\mu = 0.5$, c) $\mu = 10$. The n_i's are uniformly distributed.

coherent, turbulent, intermittent, ordered or glassy phases can occur [114, 120]. The authors realized phase diagrams in function of the bifurcation parameter r and the coupling strength ϵ. The clustering structure or distribution was studied in [114, 121, 123] and bifurcations diagrams representing the transition between different clustering states were found.

The next sections are devoted to the systematical analysis of the dynamics in the system when $\mu \neq 0$. We examine the relation between the network topology and the global dynamics. The results then lead us to an effective theory which permits us to understand this relation.

5.6 Dynamics in the network and bifurcation analysis

In the section we investigate the relation between the network topology and the global dynamics. Characterizing the dynamics of a complex system with a large number of freedom degrees is a huge topic. Depending on the specific properties one is interested in, different approaches are possible.

[121, 122, 123] already investigated the clustering properties of the system (5.1) in the case of global coupled maps (GCM). They therefore developed the idea of the evaporation

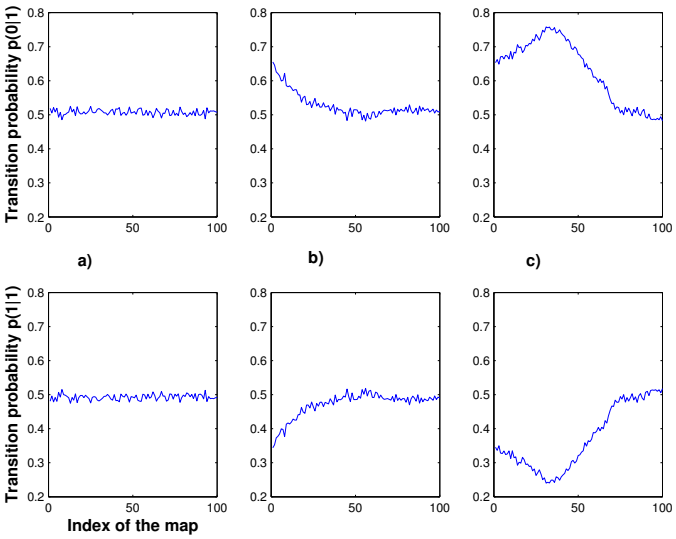

Figure 5.12: Transition probabilities $p(0|1)$ and $p(1|1)$ for each individual map. The parameters are $\kappa = 1$, $\epsilon = 0.2$ and a) $\mu = 0$, b) $\mu = 0.5$, c) $\mu = 10$. The n_i's are uniformly distributed.

exponent of clusters. This quantity is related to the Lyapunov exponent of a specific clustering state and gives its stability. Following [123, 114] it is also possible to analyze the clustering properties in the case of GCM (for example the probability of apparition of a cluster of a certain size). Some other global properties like the mean-field were considered in [108] to realize bifurcation diagrams of their systems. Our study is partially inspired from their methods.

Our motivation originally comes from the problem of understanding the dynamics in networks of coupled SIR-models or asymmetric tent map. For that reason we have particular interest in the synchronization and limit cycle properties of the system (5.1) of coupled chaotic logistic maps. Therefore we classify the behavior of the maps into two types: maps which are synchronized and fully correlated and maps which are not. This leads automatically to the concept that a map should either belong to the cluster $\mathcal{C}^S$ of synchronized systems, either to the cluster $\mathcal{C}^{NS}$ of non-synchronized systems. The size of the cluster $\mathcal{C}^S$ is numerically defined by the condition

$$\Delta_i = \sqrt{\sum_{n=1}^{\infty} (x_n^{i+1} - x_n^i)^2} > 1, \tag{5.34}$$

where $i = 1 \dots N-1$.

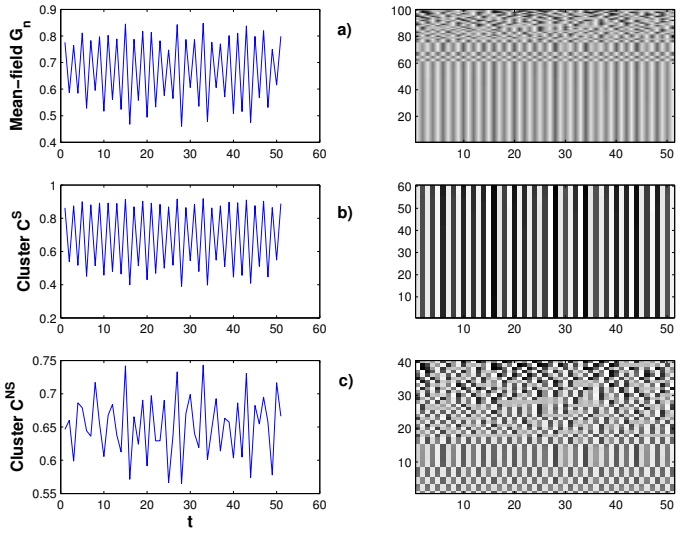

Figure 5.13: Plotted are the time series of the mean-field of a) all the system G_n, b) cluster $\mathcal{C}^S$ and c) cluster $\mathcal{C}^{NS}$. The parameters are $\mu = 10$, $\kappa = 1$, $\epsilon = 0.8$, $N = 100$ and $\rho(n)$ is a power-law distribution with $\alpha = 4$.

We consider the mean-field of all maps

$$G_n =< x_n^i >_i = \frac{1}{N}\sum_{i=1}^{N} x_n^i \tag{5.35}$$

as a measure of the global dynamics. The mean-field of the clusters $\mathcal{C}^S$ and $\mathcal{C}^{NS}$ can also be used to characterize more precisely the dynamics of the system. The time series of this three different mean-fields are plotted in Figure 5.13. The histograms and the return maps of the mean-field of this three clusters are plotted in Figure 5.14.

One observes that the mean-field G_n shows a dynamics which is very near to period-2 limit cycle and the dynamics of the cluster $\mathcal{C}^S$ is very similar to it. In opposite, the dynamics of $\mathcal{C}^{NS}$ has no noticeable structure and the maps belonging to this cluster seems to be independent of the mean-field G_n. The variable representing $\mathcal{C}^{NS}$ can be assimilated to a Gaussian distribution. This helps us to already understand the system at this stage of the study. Since the global dynamics is a superposition of the dynamics of the two clusters, one may think of reducing the whole system to a single map with additional noise. This idea will be exploited in the last section.

In order to show that the splitting the system into two classes of maps is sensible, we computed the index Δ_i defined by (5.34) and the correlation of the individual maps with

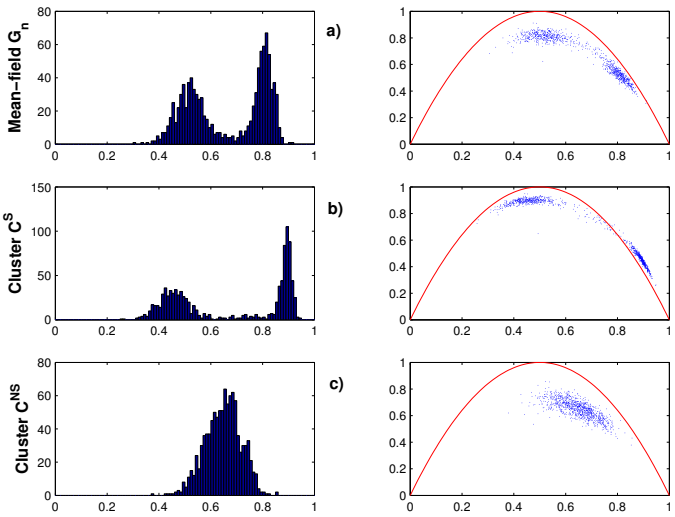

Figure 5.14: Plotted are the histograms (left) and the return map (right) of the mean-field of a) all the system G_n, b) cluster $\mathcal{C}^S$ and c) cluster $\mathcal{C}^{NS}$. The curve in red is the parabola $f(x) = 4x(1-x)$. The parameters are $\mu = 10$, $\kappa = 1$, $\epsilon = 0.8$, $N = 100$ and $\rho(n)$ is a power-law distribution with $\alpha = 4$.

the mean-field. The result is plotted in Figure 5.15. Also the pair-wise correlation between two maps i and j has been represented in matrix-form in Figure 5.16. It is obvious from these figures that the system is a superposition of the two dynamics belonging to $\mathcal{C}^S$ and $\mathcal{C}^{NS}$.

As a general result which does not dependent on the parameter set, we observe that it is possible to classify the global dynamics into three categories:

- Quasi-limit cycle: noisy logistic map where the bifurcation parameter r satisfy

$$3 < r < 1 + \sqrt{6} \tag{5.36}$$

  in the period-2 regime

- Incoherent overlapping of chaotic maps: mean-field with Gaussian distribution

$$\rho(G_n) \sim \exp\left(-\frac{1}{2}\frac{(G_n - < G_n >)^2}{\sigma^2}\right), \tag{5.37}$$

  with $G_n \approx 0.5$

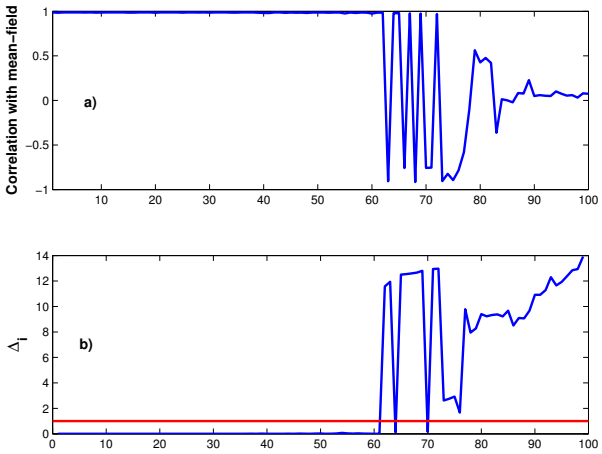

Figure 5.15: a) Correlation of the individual maps x_n^i with the mean-field G_n and b) Plot of the measure Δ_i. The parameters are $\mu = 10$, $\kappa = 1$, $\epsilon = 0.8$, $N = 100$ and $\rho(n)$ is a power-law distribution with $\alpha = 4$.

- Coherent overlapping of chaotic maps: mean-field having the same distribution

$$\rho(G_n) \sim \frac{\pi}{\sqrt{G_n(1-G_n)}} \tag{5.38}$$

  than the logistic map for $r = 4$.

We use this classification to investigate more precisely the effect of the parameters μ, κ and ρ on the dynamics. In the next section we compute for these parameters the bifurcation diagrams of the mean-field.

We start our study by assuming that each parameter can play the role of a bifurcation parameter for the mean-field. Bifurcation diagram in every direction of the parameter space (μ, κ, ϵ and size index i) will be computed. We will encounter for each parameter the classical route to chaos. Because of the strongly noisy character of the system, only transitions from fixed point to limit cycle regime and from limit cycle to chaotic regimes are resolved.

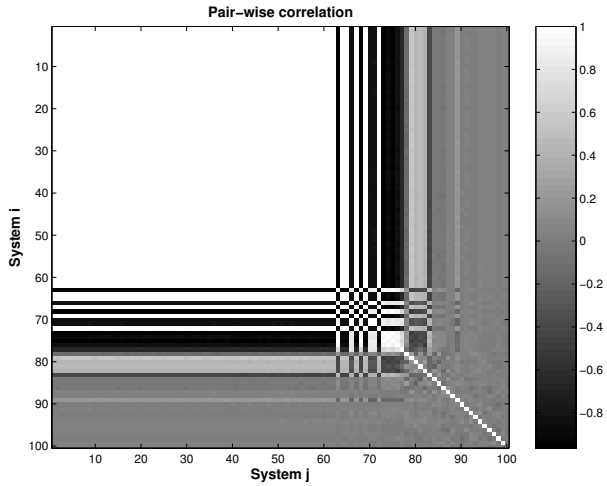

Figure 5.16: Representation of the pair-wise correlation between two maps i and j. The parameters are $\mu = 10$, $\kappa = 1$, $\epsilon = 0.8$, $N = 100$ and $\rho(n)$ is a power-law distribution with $\alpha = 4$.

5.6.1 Influence of the effective temperature $T_{eff} \sim 1/\mu$

Figures 5.17 and 5.18 show the bifurcation of the mean-field when varying the parameter μ from 0 to 2.

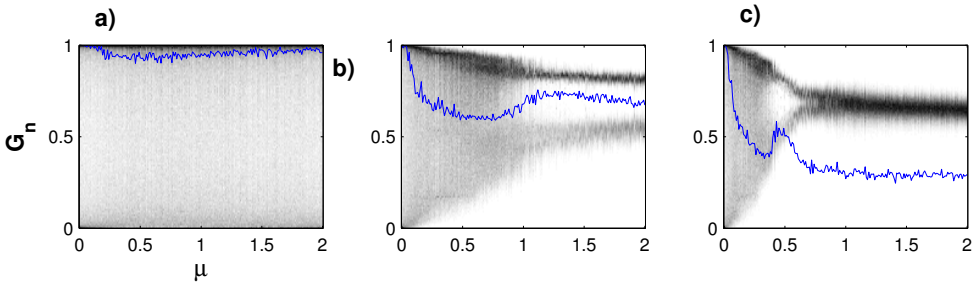

Figure 5.17: Bifurcation diagrams of the mean-field with effective parameter μ. The parameters are $\epsilon = 1$, $N = 100$, a) $\kappa = 0.5$, b) $\kappa = 1$, c) $\kappa = 2$ and $\rho(n)$ is a uniform distribution. The solid line corresponds to the size of the cluster of synchronized maps defined by $\Delta_i > 1$.

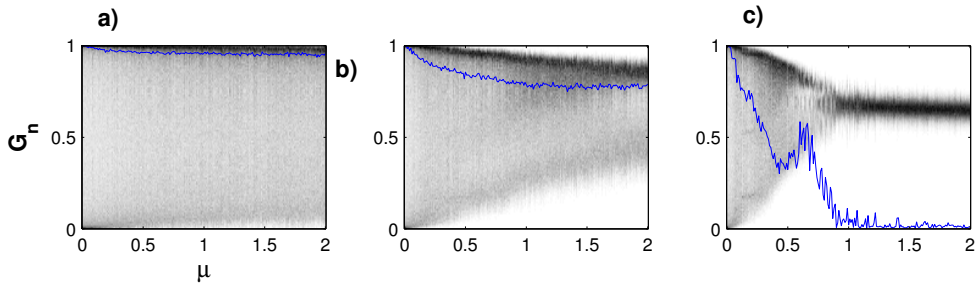

Figure 5.18: Bifurcation diagrams of the mean-field with effective parameter μ. The parameters are $\epsilon = 1$, $N = 100$, a) $\kappa = 0.5$, b) $\kappa = 1$, c) $\kappa = 2$ and $\rho(n)$ is a power-law distribution ($\alpha = 4$). The solid line corresponds to the size of the cluster of synchronized maps defined by $\Delta_i > 1$.

5.6.2 Influence of the coupling strength ϵ

Figures 5.19 and 5.20 show the bifurcation of the mean-field when varying the coupling strength ϵ from 0 to 1.

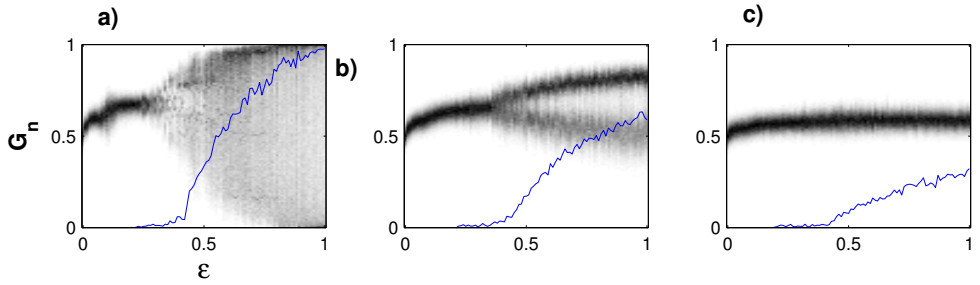

Figure 5.19: Bifurcation diagrams of the mean-field with effective parameter ϵ. The parameters are $\mu \to \infty$, $N = 100$, a) $\kappa = 0.5$, b) $\kappa = 1$, c) $\kappa = 2$ and $\rho(n)$ is a uniform distribution. The solid line corresponds to the size of the cluster of synchronized maps defined by $\Delta_i > 1$.

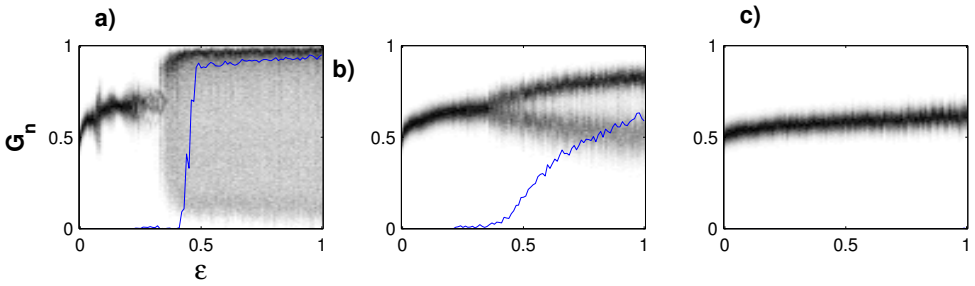

Figure 5.20: Bifurcation diagrams of the mean-field with effective parameter ϵ. The parameters are $\mu \to \infty$, $N = 100$, a) $\kappa = 0.5$, b) $\kappa = 1$, c) $\kappa = 2$ and $\rho(n)$ is a power-law distribution ($\alpha = 4$). The solid line corresponds to the size of the cluster of synchronized maps defined by $\Delta_i > 1$.

5.6.3 Influence of the threshold κ

Fig. (5.21) shows the bifurcation of the mean-field when varying the threshold κ from 0 to 4.

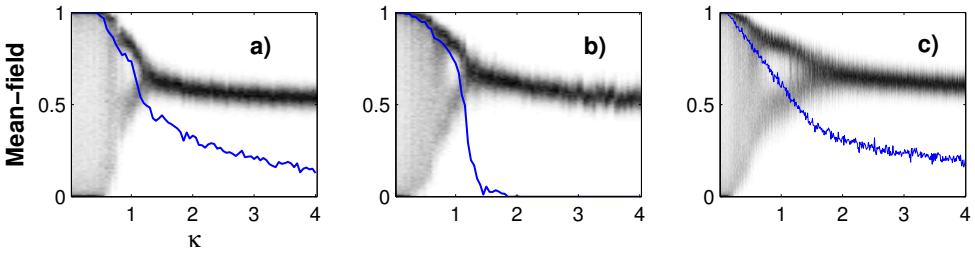

Figure 5.21: Bifurcation diagrams of the mean-field with effective parameter κ. The parameters are $\epsilon = 1$, $\mu \to \infty$, $N = 100$ and $\rho(n)$ is a a) uniform, b) power-law ($\alpha = 4$) and c) exponential ($\beta = 1$) distribution. The solid line corresponds to the size of the cluster of synchronized maps defined by $\Delta_i > 1$.

5.6.4 The role of the sizes in the system

We consider here the rank i of a map as an effective bifurcation parameter. The quantity which is examined is the time-averaged variable $< x_n^i >_n$ for each map i.

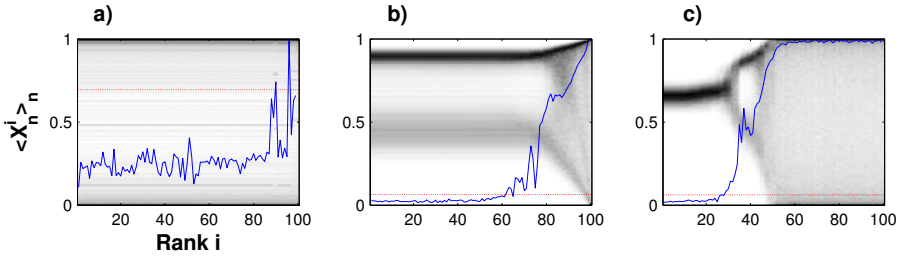

Figure 5.22: Bifurcation diagrams of the time-averaged quantity $< x_n^i >_n$. The parameters are $\kappa = 1$, $\epsilon = 1$, $\mu \to \infty$, $N = 100$, $\rho(n)$ is a uniform distribution and a) $\kappa = 0.5$, b) $\kappa = 1$, c) $\kappa = 2$. The solid line corresponds to the size of the quantity Δ_i and the dashed line to the limit $\Delta_i = 1$.

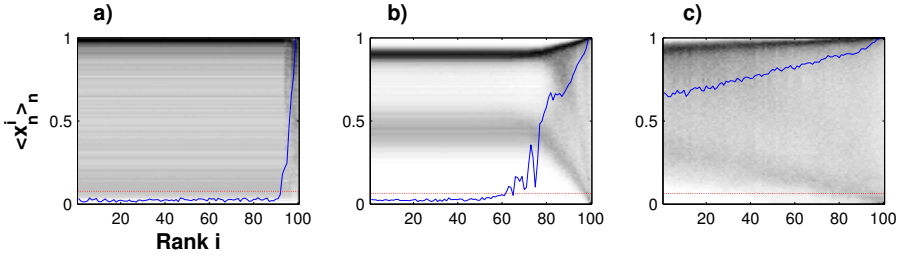

Figure 5.23: Bifurcation diagrams of the time-averaged quantity $< x_n^i >_n$. The parameters are $\kappa = 1$, $\epsilon = 1$, $\mu \to \infty$, $N = 100$, $\rho(n)$ is a power-law distribution ($\alpha = 4$) and a) $\kappa = 0.5$, b) $\kappa = 1$, c) $\kappa = 2$. The solid line corresponds to the size of the quantity Δ_i and the dashed line to the limit $\Delta_i = 1$.

5.7 An effective theory

This section is devoted to the developpement of an effective theory describing the dynamics in the network of logistic maps.

We showed in the previous section that all the parameters of the system are equivalent and may play the role of a bifurcation parameter. This means that we can arbitrarily choose one effective parameter for the theory and fixe the other ones. We therefore consider the analytical convenient case $\mu \to \infty$ where the topology of the network is hierarchical. In this case the parameter κ controls entirely the dynamics. Surprisingly, the index i also seems to be a bifurcation parameter. This gives evidence for some internal threshold in the size N of the system.

We observed in the bifurcation analysis that the correlation between the global state and the size of the cluster defined by the condition (5.34) is very high. To the fixed point

regime corresponds a small cluster size ($C \sim 0$), to the limit cycle regime corresponds an intermediate cluster size ($C \sim 0.5$) and to the chaotic regime corresponds a large cluster size ($C \sim 1$).

Also we found that the cluster size (dynamical quantity) and the clustering coefficient (statical quantity) are very strongly correlated (see fig. (5.3)) and the size distribution does not change the qualitative behavior of these quantities.

This leads us to strongly assume that the system behaves like a single noisy logistic map with an effective bifurcation parameter being a function of the clustering coefficient. This theory is developped in the following sections.

5.7.1 Analytical formulation of the evolution of the system

We developpe here an analytical formulation for the effective theory describing the dynamics observed in the network. Since there is a high correlation between the clustering coefficient and the cluster size, we consider that the size m of a cluster can be approximatly related to the clustering coefficient through $C(\kappa) = \frac{m}{N}$.

The dynamics of this cluster is then described by the equation

$$\begin{aligned} \bar{x}_{n+1} &= \left[1 - \frac{(N-m)\epsilon}{N}\right] f(\bar{x}_n) + \frac{(N-m)\epsilon}{N}\zeta_n \\ &= [1 - (1 - C(\kappa))\epsilon]\, f(\bar{x}_n) + (1 - C(\kappa))\epsilon\zeta_n \end{aligned} \tag{5.39}$$

where $\bar{x}_{n+1}$ is the mean-field of the cluster and ζ_n a term representing gaussian noise with standard deviation σ and mean ν. Another way to write eq. (5.39) is

$$\bar{x}_{n+1} = [1 - (1 - C(\kappa))\epsilon]\, f(\bar{x}_n) + (1 - C(\kappa))\epsilon(\nu + \sigma\eta_n)), \tag{5.40}$$

where $\eta_n = \mathcal{N}(0, 1)$.

Since the clustering coefficient and the cluster size are very similar in the case where $\rho(n)$ is a power-law distribution (see fig.(5.3.a)), we choose to consider the explicit form

$$C(\kappa) = \begin{cases} \frac{1}{2}\kappa^{-\alpha+1} & , \quad \kappa \geq 1 \\ 1 - \frac{1}{2}\kappa^{\alpha-1} & , \quad \kappa < 1 \end{cases} \tag{5.41}$$

In the three limiting cases where $\kappa = 0$, $\kappa = 1$ and $\kappa \to \infty$, the clustering coefficient becomes $C = 1$, $C = \frac{1}{2}$ and $C = 0$, respectively. This leads to the evolution equations

$$\bar{x}_{n+1} = f(\bar{x}_n) \tag{5.42}$$

$$\bar{x}_{n+1} = (1 - \frac{\epsilon}{2}) f(\bar{x}_n) + \frac{\epsilon}{2}(\nu + \sigma\eta_n) \tag{5.43}$$

$$\bar{x}_{n+1} = (1 - \epsilon) f(\bar{x}_n) + \epsilon(\nu + \sigma\eta_n) \tag{5.44}$$

in these three different cases.

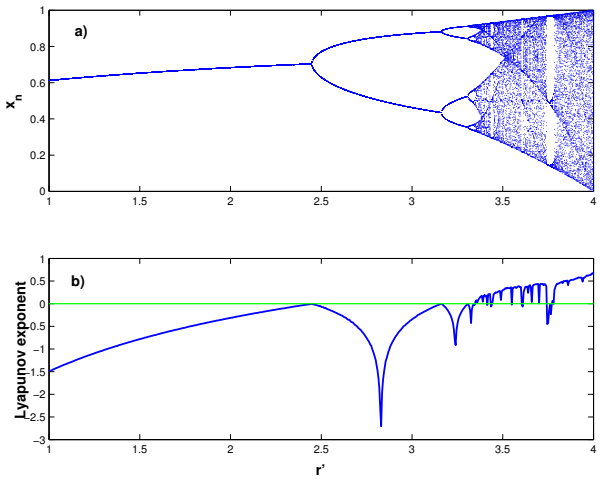

Figure 5.24: a) Bifurcation diagram and b) Lyapunov exponent of the system (5.45) with effective parameter r' and without noise ($\sigma = 0$). The parameters are $r = 4$ and $\nu = 0.5$

If $f(x) = rx(1-x)$, the equation (5.40) can be re-written as

$$\bar{x}_{n+1} = r'(\kappa)\bar{x}_n(1-\bar{x}_n) + \left(1 - \frac{r'(\kappa)}{r}\right)\nu + \left(1 - \frac{r'(\kappa)}{r}\right)\sigma\eta_n = F(\bar{x}_n) \tag{5.45}$$

where

$$r'(\kappa) = [1 - (1 - C(\kappa))\epsilon]\, r \tag{5.46}$$

We study the dynamical behavior of the system (5.45) without noise ($\sigma = 0$). Fig. (5.24) gives a graphical representation of the bifurcation diagram and the Lyapunov exponent of this system in function of the effective parameter r'. We see that this system shows the usual route to chaos with successive period-doubling of limit cycles.

5.7.2 Testing the theory

We compare in this section the dynamics of our effective theory with the global dynamics of the whole network. Therefore we plotted in fig. (5.25.a) the bifurcation diagram of the system (5.45) with noise ($\sigma \neq 0$) and in fig. (5.25.b) the bifurcation diagram of the mean-field in the network. Both systems show very similar transitions between the different dynamical regimes. In the effective theory, the period-2 limit cycle regime occurs for a parameter $\kappa \simeq 1$.

In order to confirm the exactness of our effective theory (5.45), we also compared on the same plot in fig. (5.26) the bifurcation diagram of the network and the bifurcation

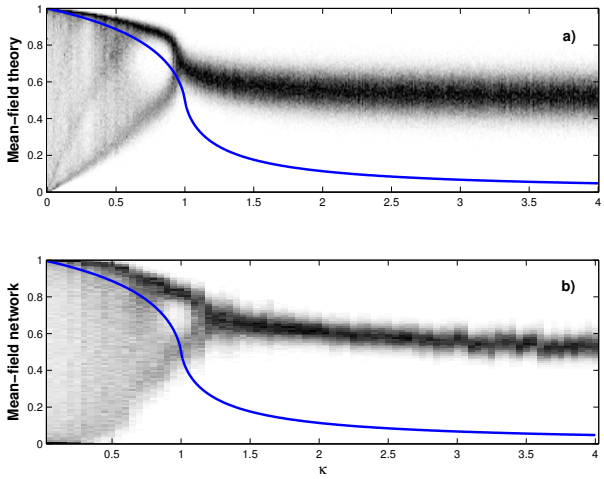

Figure 5.25: Bifurcation diagrams with parameter κ for the a) effective model and b) network. The solid line represent the clustering coefficient. The parameters are $r = 4$, $\epsilon = 1$, $\nu = 0.5$, $\sigma = 0.07$ and $\rho(n)$ is a power-law distribution ($\alpha = 4$).

diagram of the theory without noise. Both diagrams are in very good qualitative and quantitative agreement.

From our studies we conclude that the mean-field of the maps in the network is very well reproduced by the simple system (5.45). So we can affirm that our effective theory explains the structures and the phenomenon which are observed in the network of logistic maps.

5.8 Results

We investigated in this chapter the dynamics in networks of weighted maps. We introduced a new form of coupling function (5.5) which is deduced from the distribution of weights. The topology of the network is controled by adjusting a single parameter which is interpretatd as an effective temperature T_{eff}.

We performed the analysis of the new generated topologies and computed the principal properties of the network using the statistical approach. The coupling function can create a large variety of networks from global coupling to a perfectly hierachical structure, where all intermediates topologies are possible. It was found that the distribution of weights does not have any essential consequences on the topology. In fact, the effective temperature $1/\mu$ and the threshold κ are entirely controlling the network. It could then be shown that either μ or κ is sufficient to control the whole generated topology. Since the statistical

properties of the network can be computed analyticaly in the case $\mu \to \infty$, we choose κ as the only effective parameter which permits to adjust the topology. We can then compute the degree distribution, the connectivity and the clustering coefficient in function of κ. The network is not anymore weighted in this case and the links are directed. The network is globally coupled when κ is small (< 1) and not coupled at all when κ is large (> 1). The clustering coefficients then correspond to $C \approx 1$ and $C \approx 0$, respectively.

Concerning the dynamics in the networks we examined the mean-field of the system as a measure for its behavior. It was found that only three dynamical regimes can take place. The first regime is an uncoherent superposition of the dynamics of the individual maps and leads to a mean-field which is Gaussian distributed. Inthe second regime the mean-field is distributed as a bi-modal Gaussian distribution and corresponds to a global quasi-limit cycle. The third regime corresponds to a coherent superposition of the individual dynamics and the mean-field is distributed as for the logistic map in the chaotic regime ($r = 4$). In terms of a single dynamical system, these regimes can be called fixed point, period-2 limit cycle and chaos. The coupling strength ϵ, the threshold κ or the effective temperature $1/\mu$ have exactly the same effect on the global dynamics. Using bifurcation diagrams of the mean-field we observed that these parameters control in an identical way the transitions between the different regimes.

We also examined the synchronization phenomenon between the maps [110, 108]. We therefore split the system into two clusters: maps which are sychronized and maps which

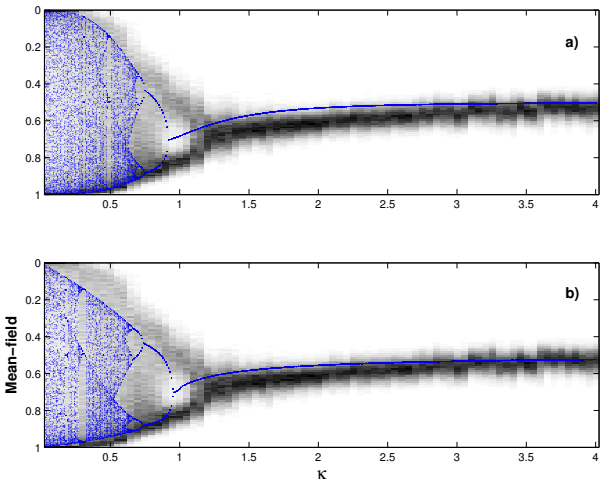

Figure 5.26: Bifurcation diagrams with parameter κ for the the effetive model (black dots) and the network (gray scale). The parameters are $r = 4$, $\epsilon = 1$, $\nu = 0.5$, $\sigma = 0.08$ and the distribution $\rho(n)$ is a) uniform and b) power-law ($\alpha = 4$).

are not synchronized. It was found that the size of the cluster of synchronized map is quasi-identical to the clustering coefficient of the network. This coefficient is a property of the network and is independent of the particular form of map $f(x)$. Furthermore we found that each regime is associated with a typical cluster size or clustering coefficient. The gaussian distribution of the mean-field corresponds to a small cluster size (≈ 0), the bi-modal distribution to an intermediate size (≈ 0.5) and the U-shaped distribution for the chaotic regime to a large size (≈ 1).

We demonstrate our findings by writing an effective theory for the whole system in the limit case $\mu \to \infty$. As we mentioned previously, since the parameters μ and κ play an equivalent role for the network topology and in the bifurcation diagrams, we can fixe one parameter (here $\mu \to \infty$) and consider only the other one (κ) as relevant for the system. Our theory is based on the fact that we can describe the cluster of synchronized maps by a single logistic map with an effective bifurcation parameter depending on the size of the cluster and the coupling strength. The cluster of non-synchronized maps can be repalaced by Gaussian noise. The result is that we can replace the system of coupled maps by a single effective logistic map with an additional noisy term. For this reason it is possible to observe global limit cycles even if the original individual maps were chaotic.

Our investigations can take into account a large variety of natural systems from the spreading of infectious diseases to the tree masting (see Appendix A).

Appendix A: Tree masting

We present in this Appendix a model for tree masting which is strikingly similar to the asymmetrical tent map derived from the SIR-model. This model was introduced in [111, 112, 23] to study synchronization between trees in forests. The model which describes the evolution of a single tree reads

$$S_{n+1}^i = \begin{cases} S_n + P_s & \text{if } S_n + P_s \leq L_T \\ S_n + P_s - a(R_c + 1)(S_n + P_s + L_T) & \text{if } S_n + P_s > L_T \end{cases} \tag{5.47}$$

where S_n is the amount of energy at the beginning of year n, P_s the net production gained per year by a tree from photosynthesis, a is a proportionality constant and R_c the ratio of fruiting costs to flowering cost. L_T represents the critical level under which the tree does not reproduce and save energy for the following year and above which the energy is used for flowering.

We can write this model in a dimensionless form

$$Y_{n+1}^i = \begin{cases} 1 + Y_n^i & , \quad \text{if } Y_n^i < 0 \\ 1 - kP_n^i Y_n^i & , \quad \text{if } Y_n^i \geq 0 \end{cases} \tag{5.48}$$

where $Y_n = (S_n + P_s - L_T)/P_s$ and $k = a(R_c + 1) - 1$. This map has exactly the same

shape than our asymmetrical tent map (4.16) but the coupling between the maps is realized through the variable k, which becomes a function of Y_n^i.

Notice that this map was derived independently from our model. Since tree masting seems to show the same mechanism than epidemics outbreaks, it may be possible to rewrite the model (5.48) as a system of differential equations.

Chapter 6

Outlook

We studied in this thesis recurrent outbreaks in natural chaotic systems. We considered the cases of phytoplankton blooms and epidemics outbreaks. In both cases we succeed to reproduce with our models the periodical behavior in time and the irregular amplitudes of the outbreaks. A class of models which permits bottom-up control of the dynamics in a system was used. This type of models show fixed points with the stability type of a stable spiral.

It was shown that some simple phytoplankton model may exhibit chaotic behavior under external periodic forcing of nutrients. We also developed in this context a method to characterize single algae bloom. This method can of course be extended to other systems showing outbreak dynamics.

The spread of epidemics in networks of cities and the synchronization of outbreaks was a topic closely related to the previous one. The individual cities were described by a model similar to the phytoplankton model. The coupling matrix has been introduced for this epidemiological model, but appears to be valid for a large variety of systems. The coupling strength in the differential equations is proportional to the ratio of the city sizes.

It was possible to reduce the SIR-model to a 1-dimensional asymmetrical tent map. This led us to a new coupling function which permits to couple weighted maps in a network. The topology of the network can be adjusted through the change of a parameter representing an effective temperature. We studied exhaustively the dynamics in the network in the case of the logistic map.

A bi-annual cycle has been observed in the data. We succeed to reproduce this 2-year cycle in the context of coupled SIR-models and coupled maps. It is striking that all these models show the same behavior only because of the topology of the network.

The new type of coupling we introduced might be very useful when needing to couple maps representing dynamical systems having some weights or sizes. But one could also think about other coupling which could be for example proportional to the product $n_i n_j$

of the sizes. This may represent cooperation between the systems.

It is also interesting to notice that very different systems can be described by similar models or mechanisms. Consider the following examples belonging to this class of systems: spreading of epidemics, masting in forests or lasers.

The striking similarity of outbreak characteristics, which is exhibited in totally different and unrelated (ecological) systems naturally leads to the question whether there are universal mechanisms underlying outbreak dynamics in different systems in ecology [2, 34]. In this sense a comparative study of complex outbreak phenomena in Nature gives information about possible underlying mechanisms and properties of the system.

Acknowledgments

This thesis was prepared under supervision of Jr. Prof. Bernd Blasius. The work was financially supported by the German *Volkswagen Stiftung*.

I wish to thank all the people with whom I had many motivating discussions and who supported me through this three years (in alphabetical order): Bernd Blasius, Jost Fischer, Gregor Fussmann, my Guitar, Annika Herzog, Nina Kuckländer, Jürgen Kurths, Ernest Montbrió, Birgit Nader, Udo Schwarz, Ralf Steuer, Jörg-Uwe Tessmer, Ralf Tönjes and Guntram Weithoff.

Bibliography

[1] M. Begon, J.L. Harper and C.R. Townsend (1996) *Ecology* Blackwell Science Ltd., Oxford.

[2] A.A. Berryman (2003) 'On principles, laws and theory in population ecology' *Oikos* **103**, 695-701.

[3] Ottar N. Bjørnstad, Mikko Peltonen, Andrew Liebhold and Werner Baltensweiler (2002) 'Waves of larch budmoth outbreaks in the European Alps' *Science* **298**, 1020-1023.

[4] Blasius B., Huppert A. & Stone L. (1999) 'Complex dynamics and phase synchronization in spatially extended ecological systems' *Nature* **399**, 354-359.

[5] Blasius B. & Stone L. (2000) 'Chaos and phase synchronization in ecological systems' *Int. J. Bifurcation and Chaos* **10**, 2361-2380.

[6] C. Vacher, D. Bourguet, F. Rousset, C. Chevillon & M.E. Hochberg (2003) 'Modeling the spatial configuration of refuges for a sustainable control of pests: a case study of *Bt* cotton *J. Evol. Biol.* **16**, 378-387.

[7] Costantino R.F., Desharnais, R.A., Cushing, J.M. & Dennis, B. (1997) 'Chaotic dynamics in an insect population' *Science* **275**, 389-391.

[8] Cushing J.M., Costantino R.F., Dennis B., Costantino R.F. & Desharnais R.A. (2002) *Chaos in Ecology* Academic Press.

[9] J. Davidson and H.G. Andrewartha (1948) 'Annual trends in a natural population of *Thrips imaginis* (Thysanoptera)' *Journal of Animal Ecology* **17**, 193-199.

[10] DeAngelis D.L. (1992) *Dynamics of nutrient cycling and food webs* Chapman and Hall, London.

[11] F. Cellina, G.A. De Leo, M. Bartoli, P. Viaroli (2002) 'The control of algal bloom damages to clam yield in a North Adriatic coastal lagoon (Sacca di Goro, Italy)' *Proceedings of the International Environmental Modeling and Software Society* **3**, 479-484.

[12] Brian Dennis, Robert A. Desharnais, J.M. Cushing, Shandelle M. Henson and R.F. Costantino (2003) 'Can noise induce chaos?' *Oikos* **102**, 329-339.

[13] Mikhail F. Dimentberg (2002) 'Lotka-Volterra system in a random environment' *Phys. Rev. E* **65**, 036204.

[14] Stephen P. Ellner (2003) 'When does parameter drift decrease the uncertainty in extinction risk estimates?' *Ecology Letters* **6**, 1039-1045.

[15] Jianfeng Feng and Guibin Li (2001) 'Integrate-and-fire and Hodgkin-Huxley models with current inputs' *J. Phys. A: Math. Gen.* **34**, 1649-1664.

[16] Gregor F. Fussmann and Gerd Heber (2002) 'Food web complexity and chaotic population dynamics' *Ecology Letters* **5**, 394-401.

[17] Hastings A. & Powell T. (1991) 'Chaos in a three-species food chain' *Ecology* **72**, 896-903.

[18] Hastings A., Hom C.L., Ellner S., Turchin P. & Godfray H.C.J. (1993) 'Chaos in ecology: is Mother Nature a strange attractor?' *Annual Review of Ecology and Systematics* **24**, 1-33.

[19] J.J. Hopfield (1999) 'Brain, neural networks and computation' *Review of Modern Physics* **71**, No. 2, 431-437.

[20] Niclas Jonzén, Per Lundberg, Esa Ranta and Veijo Kaitala (2002) 'The irreducible uncertainty of the demography-environment interaction in ecology' *Proc. R. Soc. Lond. B* **269**, 221-225.

[21] S. Kim, H. Li, E.R. Dougherty, N. Cao, Y. Chen, M. Bittner and E.B. Suh (2002) 'Can Markov chain models mimic biological regulation?' *Journal of Biological Systems* **10**, Vol. 4, 337-357.

[22] Kot M., Sayler G.S. & Schultz T.W. (1992) 'Complex dynamics in a model microbial system' *Bulletin of Mathematical Biology* **54**, 619-648.

[23] Andrew Liebhold, Victoria Sork, Mikko Peltonen, Walter Koenig, Ottar N. Bjørnstad, Robert Westfall, Joseph Elkinton and Johannes M.H. Knops (2004) 'Within-population spatial synchrony in mast seeding of North American oaks' *Oikos* **104**, 156-164.

[24] D. Ludwig, D.D. Jones and C.S. Holling (1978) 'Qualitative analysis of insect outbreak systems: the spruce budworm and forest' *Journal of Animal Ecology* **47**, 315-332.

[25] Matteo Marsili and Yi-Cheng Zhang (1998) 'Interacting individuals leading to Zipf's Law' *Phys. Rev. Let.* **80**, 2741-2744.

[26] Odum 'Ökologie' 3. Auflage, Thieme Verlag Stuttgart 1999

[27] Arkady Pikovsky and Jürgen Kurths (1997) 'Coherence resonnance in a noisy-driven excitable system' *Phys. Rev. Let.* **78**, 775-778.

[28] Esa Ranta, Per Lundberg, Veijo Kaitala and Nils Chr. Stenseth (2002) 'On the crest of a population wave' *Science* **298**, 973-974.

[29] Rinaldi S. & Muratori S. (1993) 'Conditioned chaos in seasonally perturbed predator-prey models' *Ecological Modeling* **69**, 79-97.

[30] Ian D. Rozdilsky and Lewi Stone (2001) 'Complexity can enhance stability in competitive systems' *Ecol. Let.* **4**, 397-400.

[31] Ricard V. Solé, Javier G.P. Gamarra, Marta Ginovart and Daniel López (1999) 'Controlling chaos in ecology: from deterministic to individual-based models' *Bulletin of Mathematical Biology* **61**, 1187-1207.

[32] L. Stone, R. Olinky, B. Blasius, A. Huppert and B. Cazelles 'Complex Synchronization Phenomena in Ecological Systems' *AIP Conference Proceedings* **622**(1), 476-488.

[33] Justin M.J. Travis and David R. French (2000) 'Dispersal functions and spatial models: expanding our dispersal toolbox' *Ecol. Let.* **3**, 163-165.

[34] A. Tsoularis and J. Wallace (2002) 'Analysis of logistic growth models' *Math. biosc.* **179**, 21-55.

[35] Vandermeer J., Stone L. & Blasius B. (2001) 'Categories of chaos and fractal basin boundaries in forced predator-prey models' *Chaos, Solitons and Fractals* **12**, 265-276.

[36] O'Brien W.J. (1974) 'The dynamics of nutrient limitation of phytoplankton algae: a model reconsidered' *Ecology* **55**, 135-141.

[37] Sébastien Clodong and Bernd Blasius 'Chaos in a periodically forced chemostat with algal mortality' *Proc. R. Soc. Lond. B* **271**, 1617-1624.

[38] M. R. Droop (1968) 'Vitamin B_{12} and marine ecology. IV. The kinetics of uptake, growth and inhibition in *Monochrysis Lutheri*' *J. mar. biol. Assoc. U.K.* **48**, 689-733.

[39] M. R. Droop (1973) 'Some thoughts on nutrient limitation in algae' *J. Phycolog.* **9**, 264-272.

[40] Fussmann G.F., Ellner S.P., Shertzer K.W. & Hairston Jr., N.G. (2000) 'Crossing the Hopf bifurcation in a live predator-prey system' *Science* **290**, 1358-1360.

[41] H. L. Golterman (2002) 'Archimedes and a too simple model of competition between a macrophyte and plankton' *Hydrobiologia* **472**, 107-117.

[42] Xue-Zhong He and Shigui Ruan (1998) 'Global stability in chemostat-type plankton models with delayed nutrient recycling' *J. Math. Biol.* **37**, 253-271.

[43] Jef Huisman, Anna M. Johansson, Eelke O. Folmer and Franz J. Weissing (2001) 'Towards a solution of the plankton paradox: the importance of physiology and life history' *Ecol. Let.* **4**, 408-411.

[44] A. Huppert, B. Blasius and L. Stone (2002) 'A model of phytoplankton blooms' *Am. Nat.* **159**, 156-171.

[45] Hutchinson G.E. (1961) 'The paradox of the plankton' *Am. Nat.* **95**, 137-145.

[46] W. Lampert and U. Sommer 'Limnökologie' 2. Auflage, Thieme Verlag Stuttgart 1999.

[47] Kenneth Lange and Francisco J. Oyarzun (1992) 'The attractiveness of the Droop equations' *Math. Biosci.* **111**, 261-278.

[48] S.V. Petrovskii, M.E. Vinogradov and H. Malchow (1999) 'A possible mechanism of patchiness in the spatial distribution of plankton' *Doklady Biological Sciences* **367**, 391-394.

[49] H. Malchow (2000) 'Nonequilibrium spatio-temporal patterns in models of nonlinear plankton dynamics' *Freshwater Biology* **45**, 239-251.

[50] May R.M. (1974) 'Biological populations with nonoeverlapping generations: stable points, stable cycles and chaos' *Science* **186**, 645-647.

[51] Monod, J. (1942) '*Recherches sur la croissance des cultures bactériennes*' *Hermann* Paris.

[52] W. W. Murdoch, R. M. Nisbet, E. McCauley, A. M. DeRoos and W. S. C. Gurney (1998) 'Plankton abundance and dynamics across nutrient levels: tests of hypotheses' *Ecology* **79**, 1339-1356.

[53] M. Pascual (1994) 'Periodic response to periodic forcing of the Droop equations for phytoplankton growth' *J. Math. Biol.* **32**, 743-759.

[54] Smith H.L. & Waltman P. (1995). *The theory of the chemostat: dynamics of microbial competition* Cambridge University Press, New York.

[55] Scheffer, M. (1998) *Ecology of Shallow Lakes* Chapman and Hall, London.

[56] H. L. Smith (1997) 'The periodically forced Droop model for phytoplankton growth in a chemostat' *J. Math. Biol.* **35**, 545-556.

[57] Sommer, U. (1985) 'Comparison between steady state and non-steady state competition: Experiments with natural populations' *Limnol. Oceanogr.* **30**, 335-346.

[58] Truscott, J.E. (1995) 'Environmental forcing of simple plankton models' *J. Plankton Res.* **17**, 2207-2232.

[59] T. Yoshida, L.E. Jones, S.P. Ellner, G.F. Fussmann and N.G. Hairston (2003) 'Rapid evolution drives ecological dynamics in a predator-rey system' *Nature* **424**, 303-306.

[60] M. Abel, A. Celani, D. Vergni and A. Vulpiani (2001) 'Front propagation in laminar flows' *Phys. Rev. E* **64**, 046307.

[61] Edward R. Abraham (1998) 'The generation of plankton patchiness by turbulent stirring' *Nature* **391**, 577-580.

[62] Edward R. Abraham et al. (2000) 'Importance of stirring in the development of an iron-fertilized phytoplankton bloom' *Nature* **407**, 727-730.

[63] Philip W. Boyd et al. (2000) 'A mesoscale Phytoplankton bloom in the polar Southern Ocean stimulated by iron fertilization' *Nature* **407**, 695-702.

[64] Sallie W. Chisholm (2000) 'Stirring times in the Southern Ocean' *Nature* **407**, 685-687.

[65] Sallie W. Chisholm, Paul G. Falkowoski, John J. Cullen (2001) 'Dis-Crediting Ocean Fertilization' *Science* **294**, 309-310.

[66] Paul G. Falkowski (2002) 'The Ocean's Invisible Forest' *Scientific American* **287**, 38-45.

[67] Watson W. Gregg and Margarita E. Conkright (2002) 'Decadal changes in global ocean chlorophyll' *Geophysical Research Letters* **29**, 1-4.

[68] Zoltán Neufeld, Peter H. Haynes, Véronique Garçon and Joël Sudre (2002) 'Ocean fertilization experiments may initiate a large scale phytoplankton bloom' *Geophysical Research Letters* **29**, 1-4.

[69] J.M.G. Vilar, R.V. Solé and J.M. Rubí (2003) 'On the origin of plankton patchiness' *Physica A*, Vol. 317, 239-246.

[70] Bingtuan Li, Gail S. K. Kolkowicz and Yang Kuang (2000) 'Global asymptotic behavior of a chemostat model with two perfectly complementary resources and distributed delay' *J. appl. Math.* **60**, No. 6, 2058-2086.

[71] W. Ebenhöh (1988) 'Coexistence of an unlimited number of algal species in a model system' *Theor. Pop. Biol.* **34**, No. 2, 130-144.

[72] W. Ebenhöh (1993) 'Coexistence of similar species in models with periodic environments' *Ecol. Model.* **68**, 227–247.

[73] Grover J.P. (1991) 'Non-steady state dynamics of algal population growth: experiments with two chlorophytes' *J. Phycol.* **27**, 70-79.

[74] Grover J.P. (1991) 'Dynamics of competition among microalgae in variable environments: experimental tests of alternative models' *Oikos* **62**, 231-243.

[75] Grover J.P. (1992) 'Constant- and variable-yield models of population growth: responses to environmental variability and implications for competition' *J. Theor. Biol.* **158**, 409-428.

[76] Jef Huisman and Franz J. Weissing 'Biodiversity of plankton by species oscillations and chaos' *Nature* **402**, 407-410.

[77] B. Sonnleitner (1998) 'Dynamic adaptation of microbes' *J. Biotech.* **65**, 47-60.

[78] Kai W. Wirtz (2002) 'A generic model for changes in microbial kinetic coefficients' *Journal of Biotechnology* **97**, 14-162.

[79] Bingtuan Li, Gail S. Wolkowicz abd Yang Kuang (2000) 'Global asymptotic behavior of a chemostat model with two pefectly complementary resources and distributed delay' *J. appl. math.* **60**, No. 6, 2058-2086.

[80] J.L. Aron and I.B. Schwartz (1984) 'Seasonality and period-doubling bifurcations in an epidemic model' *Journal Of Theoretical Biology* **110**, 665-679.

[81] O.E. Aié llo and M.A.A. da Silva (2002) 'Dynamical Monte-Carlo method for stochastic epidemic models' *arXiv:physics/0208089*.

[82] S. Eubank, H. Gudu, V.S.A. Kumar, M.V. Marathe, A. Srinivasan, Z. Toroczkai and N. Wang (2004) 'Modeling disease outbreaks in realistic urban social networks' *Nature* **429**, 180-184.

[83] B.T. Grenfell, B.M. Bolker and A. Kleczkowski (1995) 'Seasonality and extinction in chaotic metapopulations' *Proc. R. Soc. Lond. B* **259**, 97-103.

[84] Earn D.J.D, Rohani P., Bolker B.M. & Grenfell B.T. (2000) 'A simple model for complex dynamical transitions in epidemics' *Science* **287**, 667-670.

[85] B.T. Grenfell, O.N. Bjørnstad and J. Kappey (2001) 'Traveling waves and spatial hierarchies in measles epidemics' *Nature* **414**, 716-723.

[86] P. Rohani, C.J. Green, N.B. Mantilla-Beniers and B.T. Grenfell (2003) 'Ecological interference between fatal diseases' *Nature* **422**, 885-888.

[87] M.J. Keeling (1999) 'The effects of local spatial structure on epidemiological invasions' *Proc. R. Soc. Lond. B* **266**, 859-867.

[88] Matt J. Keeling (2000) 'Simple stochastic models and their power-law type behavior' *Theoretical Population Biology* **58**, 21-31.

[89] Matt Keeling (2000) 'Evolutionary trade-offs at two time-scales: competition versus persistence' *Proc. R. Soc. Lond. B* **267**, 385-391.

[90] Matt J. Keeling, Pejman Rohani and Bryan T. Grenfell (2001) 'Seasonally forced disease dynamics explored as switching between attractors' *Physica D* **148**, 317-335.

[91] Ken T.D. Eames and Matt J. Keeling (2002) 'Modelling dynamic and network heterogeneities in the spread of sexually transmitted diseases' *Proc. Natl. Acad. Sci.* **99**, Vol. 20, 13330-13335.

[92] Matt J. Keeling (2002) 'Using individual-based simulations to test the Levins metapopulation paradigm' *Journal of Animal Ecology* **71**, 270-279.

[93] Matt J. Keeling and Pejman Rohani (2002) 'Estimating spatial coupling in epidemiological systems: a mechanistic approach' *Ecol. Let.* **5**, 20-29.

[94] Matt J. Keeling and Bryan T. Grenfell (2002) 'Understanding the persistence of measles: reconciling theory, simulation and observation' *Proc. R. Soc. Lond. B* **269**, 335-343.

[95] Pejman Rohani, Matthew J. Keeling and Bryan T. Grenfell (2002) 'The interplay between determinism and stochasticity in childhood diseases' *The American Naturalist* **159**, No. 5, 469-481.

[96] Robert M. May and Alun L. Lloyd (2001) 'Infection dynamics on scale-free networks' *Phys. Rev. E* **64**, 06612.

[97] Ingemar Nåsell (2002) 'Stochastic models of some endemic infections' *Mathematical Biosciences* **179**, 1-19.

[98] Patrick W. Nelson and Alan S. Perelson (2002) 'Mathematical analysis of delay differential equation models of HIV-1 infection' *Mathematical Biosciences* **179**, 73-94.

[99] M.E.J. Newman (2002) 'Exact solutions of epidemic models on networks' *arXiv:cond-mat/0201433*.

[100] Alberto d'Onofrio 'Stability properties of pulse vaccination strategy in SEIR epidemic model' *Mathematical Biosciences* **179**, 57-72.

[101] Romualdo Pastor-Satorras and Alessandro Vespignani (2001) 'Epidemic spreading in scale-free networks' *Phys. Rev. Let.* **86**, 3200-3203.

[102] Romualdo Pastor-Satorras and Alessandro Vespignani (2001) 'Epidemic dynamics and endemic states in complex networks' *Phys. Rev. E* **63**, 066117.

[103] Peter M. Strebel and Stephen L. Cochi (2001) 'Waving goodbye to measles' *Nature* **414**, 695-696.

[104] Sarika Jalan and R.E. Amritkar (2003) 'Self-organized and driven phase synchronization in coupled maps' Phys. Rev. Let., Vol. **90**, 014101.

[105] Réka Albert and Albert-Lázló Barabási (2001) 'Statistical mechanics of complex networks' *cond-mat/0106096*.

[106] Alain Barrat, Marc Barthelemy and Alessandro Vespignani (2004) 'Weighted evolving networks: coupling topology and weight dynamics' *Phys. Rev. Let.* **92**, 228701.

[107] Ginestra Bianconi and Albert-László Barabási (2001) 'Bose-Einstein condensation in complex networks' *Phys. Rev. Let.* **24**, 5632-5635.

[108] Prashant Gade and Chin-Kun Hu (2000) 'Synchronous chaos in coupled map lattices with small-world interactions' Phys. Rev. E, Vol. **62**, 6409-6413.

[109] Jon Greenman, Masashi Kamo and Mike Boots (2003) 'External forcing of ecological and epidemiological systems: a resonance approach' *Physica D* **190**, 136-151.

[110] H. Hong, M.Y. Choi and Beom Jun Kim (2002) 'Synchronization on small-world networks' Phys. Rev. E, Vol. **65**, 026139.

[111] Y. Isagi, K. Sugimura, A. Sumida and H. Ito (1997) 'How does masting happen and synchronize?' J. Theor. Biol., Vol. **187**, 231-239.

[112] Yoh Iwasa and Akiko Satake (2004) 'Mechanisms inducing spatially extended synchrony in mast seeding: the role of pollen coupling and environmental fluctuation' *Ecological Research* **19**, 13-20.

[113] J. Jost and M.P. Joy (2002) 'Spectral properties and synchronization in coupled map lattices' *Phys. Rev. E* **65**, 016201.

[114] Kunihiko Kaneko (1990) 'Clustering, coding, switching, hierarchical ordering and control in a network of chaotic elements' *Physica D* **41**, 137-172.

[115] Kunihiko Kaneko (1991) 'Partition complexity in a network of chaotic elements' *J. Phys. A: Math. Gen.* **24**, 2107-2119.

[116] Kunihiko Kaneko (1992) 'Mean-field fluctuation of a network of chaotic elements' *Physica D* **55**, 368-384.

[117] Kunihiko Kaneko (1994) 'Relevance of dynamic clustering to biological networks' *Physica D* **75**, 55-73.

[118] Kunihiko Kaneko (1997) 'Coupled maps with growth and death: an approach to cell differentiation' *Physica S* **103**, 505-527.

[119] Junji Ito and Kunihiko Kaneko (2002) 'Spontaneous structure formation in a network of chaotic units with variable connection strengths' *Phys. Rev. Let.* **88**, 028701.

[120] Tatsuo Shibata and Kunihiko Kaneko (2003) 'Coupled map gas: structure formation and dynamics of interacting motile elements with internal dynamics' *Physica D* **181**, 197-214.

[121] A. Pikovsky, O. Popovych and Yu. Maistrenko (2001) 'Resolving clusters in chaotic ensembles of globally coupled identical oscillators' *Phys. Rev. Let.* **87**, 044102.

[122] O. Popovych, Yu. Maistrenko, E. Mosekilde, A. Pikovsky and J. Kurths (2001) 'Transcritical riddling in a system of coupled maps' *Phys. Rev. E* **63**, 036201.

[123] O. Popovych, A. Pikovsky, and Yu. Maistrenko (2002) 'Cluster-splitting bifurcation in a system of coupled maps' *Physica D* **168**, 106-125.

[124] R. Steuer, J. Kurths, O. Fiehn and W. Weckwerth (2003) 'Observing and interpreting correlations in metabolomic networks' *Bioinformatics* **19**, No. 8, 1019-1026.

[125] Akiko Satake and Yoh Iwasa (2000) 'Pollen coupling of forest trees: forming synchronized and periodic reproduction out of chaos' *J. theor. biol* **203**, 63-84.

[126] Akiko Satake and Yoh Iwasa (2002) 'The synchronized and intermittent reproduction of forest trees is mediated by the Moran effect, only in association with pollen coupling' *Journal of Ecology* **90**, 830-838.

[127] A. Trusina, S. Maslov, P. Minnhagen and K. Sneppen (2004) 'Hierarchy measures in complex networks' *Phys. Rev. Let.* **92**, 178702.

[128] Tomoji Yamada and Hirokazu Fujisaka (1983) 'Stability theory of synchronized motion in coupled-oscillator systems. II' *Prog. Theor. Phys.*, vol. **70**, No. 5, 1240-1248.

[129] Finkenstädt B.F. & Grenfell B.T. (2000) 'Time series modelling of childhood diseases: a dynamical systems approach' *Apll. Statist.* **49**, 187-205.

[130] Bjørnstad O.N., Finkenstädt B.F. & Grenfell B.T. (2002) 'Endemic and epidemic dynamics of measles. I. estimating transmission rates and their scaling using a time series SIR model' *Ecological Monographs* **72**, 169-184.

[131] C.P. Dettmann (1999) 'Traces and determinants of strongly stochastic operators' *Phys. Rev. E* **59**, 5231-5234.

[132] Werner Ebeling, Jan Freund and Katja Rateitschak (1996) 'Entropy and extended memory in discrete chaotic dynamics' *International Journal of Bifurcation and Chaos* **6**, No. 4, 611-625.

[133] R. Quian Quiroga, T. Kreuz and P. Grassberger (2002) 'Event synchronization: a simple and fast method to measure synchronicity and time delay patterns' *Phys Rev E* **66**, 041904.

[134] Hanspeter Herzel and Ivo Große (1995) 'Measuring correlations in symbol sequences' *Physica A* **216**, 518-542.

[135] Svetoslav Nikolov and Sébastien Clodong (2004) 'Hyperchaos in a modified family of Röss ler systems' *Chaos, Solitons and Fractals* **21**, 803-808.

[136] R. Steuer, W. Ebeling, D.F. Russell, S. Bahar, A. Neiman, F. Moss (2001) 'Entropy and local uncertainty of data from sensory neurons' *Phys. Rev. E* **64**, 061911.

[137] F. Takens (1981) Detecting strange attractors in turbulence, in Rand D. & Young L.S. (Eds.) *Dynamical Systems and Turbulence*, Warwick, Springer Lecture Notes in Mathematics **898**, 366-381.

[138] Wolf, A., Swift, J.B., Swinney, H.L. & Vastano, J.A. (1985) 'Determining Lyapunov exponents from a time series' *Physica D* **16**, 285-317.